Spring 2011

Effect of hydrophobicity and surface roughness on two-phase flow in rectangular microchannels

Gautham C. Unni

Department: Chemical and Biochemical Engineering

EFFECT OF HYDROPHOBICITY AND SURFACE ROUGHNESS ON TWO-PHASE FLOW IN RECTANGULAR MICROCHANNELS

by

GAUTHAM C. UNNI

A DISSERTATION

Presented to the Faculty of the Graduate School of the

MISSOURI UNIVERSITY OF SCIENCE AND TECHNOLOGY

In Partial Fulfillment of the Requirements for the Degree

DOCTOR OF PHILOSOPHY

in

CHEMICAL ENGINEERING

2011

Approved by

Dr. Kimberly Henthorn
Dr. Xing Yangchuan
Dr. Douglas Ludlow
Dr. Neil Book
Dr. Chang-Soo Kim

ABSTRACT

Two-phase flows in microchannels have received significant attention recently, and have become the cornerstone of numerous microfluidic devices. Microscale devices used for bioengineering applications, oil recovery, and chemical and catalytic microreactor applications involve the transport of bubbles in confined fluidic networks in channels of micrometer length scale. These types of two-phase flows result in pressure variations, leading to an overall increase in pressure drop. Among various flow parameters, pressure drop is extensively used in design of microfluidic devices. There are several parameters that affect the pressure drop across two-phase flow in microchannels. In the present study, the goal is to be able to predict the pressure drop of two-phase flow in rectangular microchannels as a function of hydrophobicity, surface roughness, and bubble size. The SU-8 channels are fabricated using photolithography to ensure a perfectly smooth surface, which eliminates the effect of surface roughness. The fabricated channels are treated to alter the contact angle of water on SU-8, isolating the effects of hydrophobicity. Pressure drop data of air-water two-phase flow across the channels was collected, and compared to a previously published model, which predicts the pressure drop across a smooth hydrophilic rectangular microchannel with an air bubble flowing through it. Deviations of the experimental pressure drop from the predicted values were observed as a function of hydrophobicity and bubble size; this information was used to introduce a term, accounting for the effects of hydrophobicity and bubble size, into the existing model. A method of fabricating rough SU-8 channels was proposed to isolate the effects of surface roughness. The model was validated using channels of varying aspect ratios. It was found that the proposed model was independent of the aspect ratio.

ACKNOWLEDGMENTS

I would like to thank my advisor, Dr. Kimberly Henthorn, without her invaluable guidance this dissertation would surely have not been the same. I'm extremely grateful for the guidance, encouragement, and for teaching me to be independent in my research. You have been a source of inspiration to me and I would like to thank you from the bottom of my heart for being the person I could look up to when I needed anything over the last few years.

I am thankful to Dr. Chang Soo Kim for all his valuable insights on the project. All the resources provided and the permission to use his lithography equipments at will has gone a long way in the completion of this project. I thank Dr. David Henthorn and his research group for allowing us to implement their technique in our project, and for the timely advice provided. I am grateful to my committee member for investing their time to review my work.

I would like to thank Ashish, who has been like a brother to me, for the constant support, and for all the fun we have had over the last decade. I thank Varun for always being around when needed, Nishitha for constantly entertaining me on skype, and Anil for being a good friend. I thank all my friends for their support.

I thank Adya, Anoop, Anurag, Arvind, Karthik, Kiran, Mohit, Shreekanta and Shilpa for the great times we have spent together.

I would like to thank my parents for their support and love during my best and worst times. They are a constant inspiration to me and their undying support has brought me this far. I owe all of this to them.

TABLE OF CONTENTS

Page

LIST OF ILLUSTRATIONS

LIST OF TABLES

1. INTRODUCTION

Two-phase flows in microchannels have received significant attention recently, and have become the cornerstone of numerous microfluidic devices. Microscale devices used for bioengineering applications, oil recovery, and chemical and catalytic microreactor applications involve the transport of bubbles in confined fluidic networks in channels of micrometer length scale (1-3). These types of two-phase flows result in pressure variations, leading to an overall increase in pressure drop (4).

Microscale devices are commonly fabricated using photolithography, which has led to the increased use of rectangular channels in microfluidic networks (13). Theoretical (5,6) and experimental (7,8) studies of pressure variation in channels containing bubbles show that the pressure drop in circular and rectangular microchannels are different due to the leakage of fluid at the corners of rectangular channels (7,9-11). Although most of the mentioned applications involve the flow of a single bubble in a confined channel, the main focus of most published studies has been related to a train of bubbles in channels and rather than the movement of a single bubble. There is very little research on understanding flow characteristics and their related factors for systems involving the flow of a single bubble in a rectangular microchannel. However, these fundamentals are of utmost importance to the design of microfluidic devices.

Interactions between the bubble, liquid, and microchannel surface play a critical role in the behavior of bubbles during manipulation. In particular, channel roughness is directly related to the frictional resistance imparted on the bubbles by the channel surface. As the channel size decreases, surface roughness becomes an important parameter.

Experiments conducted with rough channels have shown significant deviation in friction factor from the conventional laminar theory. The common observation made is that as hydraulic diameter decreases, friction factor increases and the transition Reynolds number decreases (12-15).

In addition, the hydrophobic nature of the channel surface impacts the meniscus shape, lubrication, and movement of the bubble through the channel. At the microscale, the surface force has influence on the bubble movement because of the higher surface-to-volume ratio, especially for two-phase flow (16). Also, high wall adhesion forces have to be overcome in order to drive a bubble through a hydrophobic channel, when compared to only balancing of viscous forces in hydrophilic channels (78). Investigation of flow patterns in hydrophilic and hydrophobic microchannels has shown that a slug bubble is lubricated with liquid film on a hydrophilic surface but that bubble has no liquid film on a hydrophobic surface (18), confirming the influence of surface forces in two-phase flow in hydrophobic channels. Experimental studies using circular and rectangular microchannels showed that the pressure drop against a hydrophobic surface is higher than that against a hydrophilic one (19). All physical behavior in two-phase flow is governed by a flow pattern. Investigation of the effect of wettability on the two-phase flow regime shows change in flow regime when the surface becomes hydrophobic (17). There has been extensive study on flow patterns due to hydrophobic surfaces, but correlation of effects of hydrophobicity on flow characteristics such as pressure drop is still lacking.

In this study, the goal is to be able to predict the pressure drop of two-phase flow in rectangular microchannels as a function of hydrophobicity, surface roughness, and bubble size. The SU-8 channels are fabricated using photolithography to ensure a

perfectly smooth surface, which eliminates the effect of surface roughness. The fabricated channels are treated using a technique developed by the David Henthorn research group (21). The method allows the contact angle of water on SU-8 to be varied between 80° and 8°. Pressure drop data of air-water two-phase flow across the channels was collected, and compared to a previously published model, which predicts the pressure drop across a smooth hydrophilic rectangular microchannel with an air bubble flowing through it (7). Deviations of the experimental pressure drop from the predicted values were observed as a function of hydrophobicity; this information was used to introduce a hydrophobicity term into the existing model.

The proposed model was then used to isolate the effect of surface roughness. Polydimethylsiloxane (PDMS) channels with varying degrees of roughness were used to study the effect of surface roughness on pressure drop in these systems. The data will be used to introduce a roughness term into the proposed model.

2. BACKGROUND

2.1 TWO-PHASE FLOW

Much of the documented work with two-phase flows has been focused on understanding flow regime transitions. Suo and Griffith [23], Barnea *et al.* [24], Damianides and Westwater [25], Fukano *et al.* [26] made the earliest attempts to understand flow regime transitions as a function of decreasing diameters. These papers primarily focus on explanations and transition criteria deviations from the theoretical predictions of Taitel and Dukler [79].

Investigations on the influence of channel diameter and shape on flow patterns and regime transitions for two-phase flow in tubes with small hydraulic diameters were carried out by Coleman and Garimella [31] and Triplett *et al.* [32]. They used high-speed video analysis to develop flow regime maps and transitions between various (bubble, dispersed, elongated bubble, slug, stratified, churn, slug-annular, wavy, annular wavy, and annular) regimes. Several other similar regimes and transitions involving air-water flows in small channels were documented by researchers [24,27,33-35].

Yang and Shieh [36] investigated the effect of change in working fluid on prediction of flow regime transitions. They used tubes with diameters ranging from 1-3 mm, and R-134a refrigerant as the working fluid instead of an air-water mixture. They observed that the flow regime transitions were not similar to those predicted for air-water mixture. The deviation was attributed to the lower surface tension of R-134a.

A flow regime map for microchannels as a function of surface tension, shear, and buoyancy forces was developed by Tabatabai and Faghri [37]. They determined the occurrence of slug, plug and bubbly regime using the size and distance between the collars and bridges, which were formed with an increase in gas-phase velocity.

Wambsganss *et al.* [38] employed flow visualization and dynamic pressure measurements to observe flow patterns and transitions in rectangular channels. He used channels of hydraulic diameter 5.45 mm and aspects ratios of 6 and 0.167 for the flow analysis. He then extended this work [39], where he used the root mean square pressure changes to develop a criterion for transition of bubble or plug flow to slug flow.

Feng and Serizawa [40] investigated flow regime patterns and transitions in microchannels with diameters ranging from 25-100 μm. They recorded all the standard flow regimes except bubbly flow, which was attributed to low Reynolds number. They also observed that the flow patterns were not affected by gravitational forces.

Kawaji *et al.* [41-43] found that in 50 - 530 μm channels, the flow patterns in the larger tubes in this range were similar to those reported by Triplett *et al.* [32], but in the smaller channels only slug flow was observed. The attributed the absence of other flow regimes in smaller diameter channels to effects of viscous and surface tension forces. They concluded that the Bond number, Reynolds number, Weber number, and capillary number decrease with decreasing channels size. This meant that the viscous and surface tension forces were more influential than gravitational and inertial forces.

The lack of comprehensive understanding of the effects of surface tension, surface wettability and liquid viscosity has be summarized by Ghiaasiaan and Abdel-Khalik [22] in their review paper on research being conducted on two-phase flow in microchannels. They concluded that there is still a lack of correlations for predicting pressure drop and heat transfer. Also, link between two-phase flow regimes and pressure drop in microchannels in order to design better microfluidic devices has been a challenging area of research which has still been found wanting.

2.2 PRESSURE DROP

Determination of the pressure drop in conventional channels widely uses the correlations developed by Lockhart and Martinelli [46], Chisholm [47], and Friedel [48]. Specific geometry or flow conditions under consideration are accounted for by modifying these correlations. Many of the more recent correlations use the above-mentioned correlations as a basis even though they have shown considerable deviations from the data for small channels with two-phase flows. Most of the work with small channels with regard to flow regime mapping has been for adiabatic flows of air-water mixtures. Investigators [49-51] have shown that in channels with hydraulic diameters ranging from 1-6 mm, the pressure drop across two-phase flow can be reasonably predicted by the homogeneous flow model. Studies conducted by Yang and Webb [52], and Yan and Lin [53] using the homogeneous flow model showed that the influence of entrance lengths and tube roughness increased the friction factor.

Mishima and Hibiki [27] modified the classical correlations in their work with air-water flows through 1-4 mm tubes. They developed the expression (Equation 1) for Chisholm's [54] parameter in the Lockhart-Martinelli [46] correlation. Based on experiments conducted, they found the parameter to be a function of hydraulic diameter in microscale systems rather than the value "5" used in conventional scale systems.

$$C = 21(1 - e^{-0.319 D_h}) \tag{1}$$

The *C* parameter in Chisholm's [54] equation for the Lockhart-Martinelli [46] multiplier was further modified by Wang *et al.* [55] to develop flow-regime-specific values. They used pressure drop measurements across adiabatic air-water flow in tubes of diameter 6.5 mm for the modification. Chen *et al.* [56] accounted for the effects surface tension and mass flux by modifying the homogeneous flow pressure drop model. They later concluded that the effect of gravity was overemphasized through Froude number when compared to the effect of surface tension through Weber number in Friedel [48] correlation.

Lee and Lee [58] noted that the effect of slug Reynolds number, the ratio of viscous and surface tension effects were significant in surface-tension dominated air-water flows. They carried out the flow experiments in rectangular microchannels with gaps ranging from 0.4-4 mm between the bubbles. They modified the Chisholm's parameter to account for the gap size as well as the phase flow rates. They observed that as the gap size decreased the flow tended more to plug and slug flow. Also, the curvature of the caps of the bubble increased the effect of surface tension.

Tran *et al.* [59] and Zhang and Webb [60] also modified previously existing correlations. Tran *et al.* modified the Chisholm correlation to account for the effects of surface tension. They noted that the pressure drop is higher in small tubes (D = 2.4-3 mm) where bubbles are confined and elongated when compared to large tubes where the bubble flow is unrestricted. Zhang and Webb modified the Friedel [48] correlation as a function of reduced pressure rather than density and viscosity ratios.

Dukler and Hubbard [61] observed that a slow moving liquid film is accelerated to the slug velocity by a fast moving slug. They also noted that the pressure drop contribution of the film portion was negligible. Using these observations they developed a pressure drop model and an expression for relative slug lengths for an air-water flow in tubes of diameter 3-8 mm. Fukano *et al.* [62] conducted experiments with air-water in circular tubes and proposed a pressure drop correlations for bubbly, slug, plug, and annular flow.

The models developed to predict pressure drop has been predominantly for circular microchannels. Fuerstman et al. [10] developed a model to predict the pressure drop across rectangular microchannels for two-phase flow. According to this model, they categorized the pressure drop into the pressure drop contribution from the part of the channel with no bubble, the body of the bubble and the caps of the bubble. They used channels with heights ranging from 20-75 microns, and widths ranging from 68-132 microns. The model was validated experimentally and found to be independent of liquid viscosity and channel aspect ratio. The model can successfully predict the pressure drop in completely smooth and hydrophilic microchannels. The research here concentrates on how to improve this model to account for the effects of surface roughness and surface wettability.

2.3 PHOTOLITHOGRAPHY

Lithography techniques include processes such as electron beam lithography, ion beam lithography, imprint technique, photolithography, and many more. All of these techniques have advantages in particular steps of the process, with the most common trade off being time against resolution [80].

Photolithography is the method of transferring a desired pattern onto a substrate. Pattern transfer is achieved by exposing a photosensitive material (coated on the substrate) to light to change its chemical properties. Altering the chemical properties of the photosensitive material makes it either more resistant or less resistant to a particular solvent known as the developer solution. The developer solution removes the less resistant area of the material resulting in the desired pattern being transferred onto the substrate [63].

The photolithography steps are shown in detail in Figure 2.1. The process begins with the preparation of the substrate. Glass that is predominantly used as the substrate in this thesis is cleaned using acetone or methanol to remove impurities, ensuring better resist adhesion to the surface. In case of silicon wafer, silicon dioxide is deposited onto the wafer surface. It is important that the deposition is even and the surface is flat. Certain wafers can be bought off the market with silicon dioxide already coated on the surface. Silicon dioxide can be stripped using hydrofluoric acid for applications which do not require it. The wafers are then cleaned with acetone or methanol [63, 80].

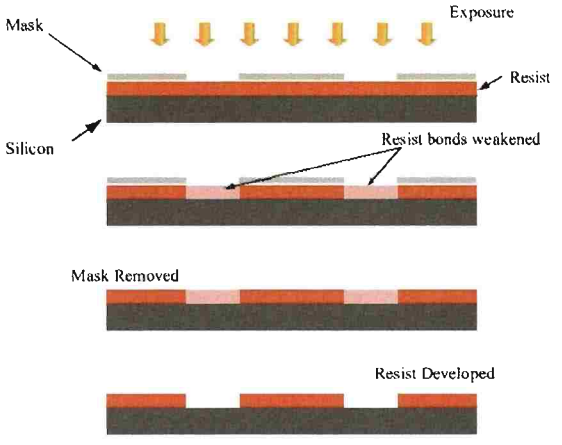

Figure 2.1 Schematic representation of the steps involved in photolithography process [63]

The resist is then spun onto the substrate surface. This process is often carried out using a spincoater. To evenly distribute the polymer onto the substrate surface, it is spun at a controlled speed for a set amount of time. The thickness of the polymer layer can be controlled by the spin speed and time (Equation 2).

$$T = \frac{KC^{\beta}\eta^{\gamma}}{\omega^{\alpha}} \tag{2}$$

where C is the resist concentration, η is the polymer viscosity, ω is the spin speed, and α, β, γ, and K are calibration constants [80]. The film thickness vs spin speed data for SU-8 2150, used in this research, are shown in Figure 2.2.

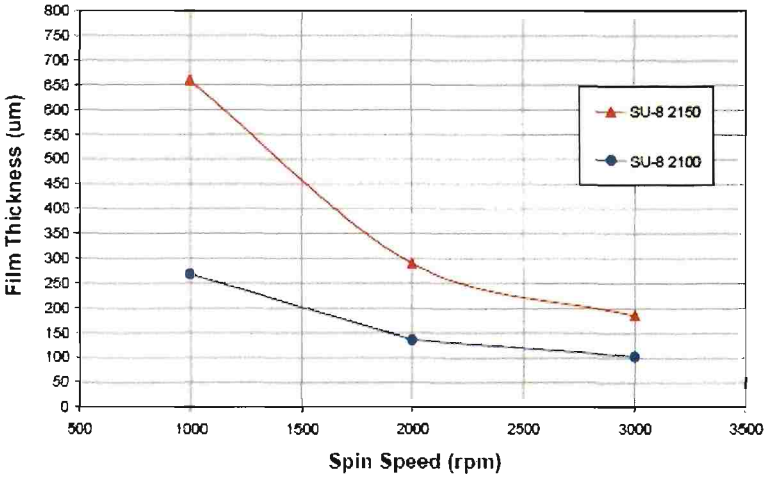

Figure 2.2 SU-8 2150 film thickness vs spin speed graph [67]

The type of photoresist used plays an important role as well. A developed structure using positive photoresist will result in a positive image of the photomask, while a negative photoresist will result in a negative image of the photomask. Exposure of the photoresist to a light source of appropriate energy and wavelength optically activates it rendering it either soluble or insoluble. Positive resist, upon being optically activated, breaks the polymer chains resulting in the resist becoming more soluble to an alkaline solution, while the negative resist initiates cross-linking resulting in the resist becoming insoluble to a solvent developer [80]. The difference in the structure when developed using positive and negative photoresist is shown in Figure 2.3.

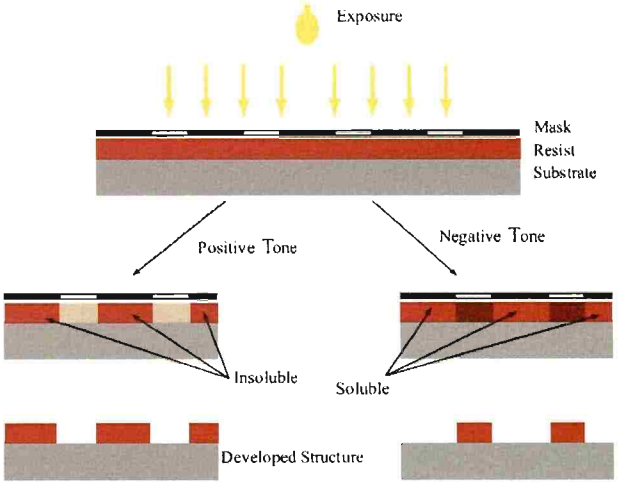

Figure 2.3 Schematic representation of structures developed using positive and negative photoresist [63]

The next step is the soft bake step, which is performed before exposure to harden the resist and evaporate any solvents remaining. The type of photoresist used determines the temperature and time of the soft baking process. Following the baking, the resist is exposed to a UV light source under a mask of the desired pattern.

The next step involved is the development step. Here, the pattern on the mask is translated on to the exposed resist [80]. SU-8 uses a SU-8 developer (1-Methoxy-2-propyl acetate) to dissolve the unexposed resist areas yielding a negative image of the mask.

2.4 CONTACT ANGLE

Contact angle is a good measure of surface energy, which in turn is a characteristic of chemical bonding. The surface energy of the solid is most easily estimated from the contact angle of a liquid droplet on the solid surface. The contact angle is defined as "the angle between a tangent drawn on the drop's surface at the contact point and a tangent to the supporting surface" [68] (Figure 2.4).

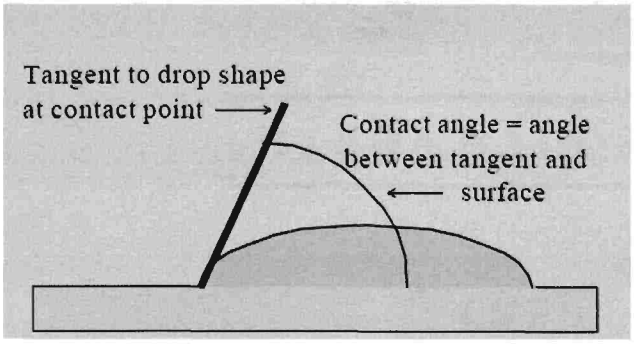

Figure 2.4 Representation of contact angle measurement [81]

Information on the chemical bonding nature of the surface can be found by the contact angle, which determines its wettability and adhesion. Chemical bonds are the attractive forces between atoms in a molecule and between adjacent molecules in a substance. In an idealized solid as shown in Figure 2.5 [68], bonds are satisfied in all directions of an atom in the interior, but the atoms on the top row have one bond not satisfied. These unsatisfied bonds are the source of wetting and adhesion. The adhesion strength with depend on the surface energy and its potential to satisfy the bond when another substance is brought near. Contact angles are used to estimate the nature and strength of these bonds.

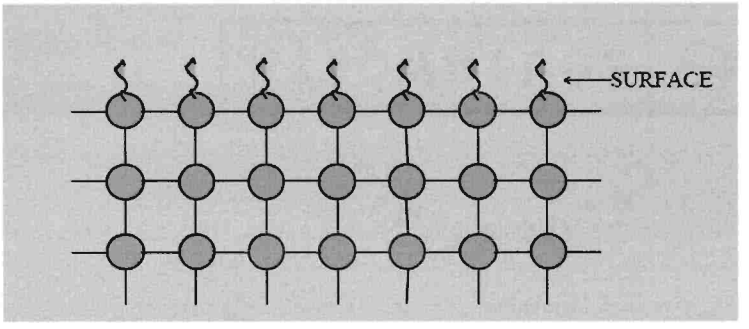

Figure 2.5 Schematic of an ideal solid surface [81]

A contact angle between the range from 0^0 to 180^0 is formed when a drop of water is placed on the solid surface, which defines the wetting or non-wetting behavior of the surface. Contact angle is the measure of the equilibrium between adhesive and cohesive forces between the molecules at the liquid-solid interface [69]. The surface can be classified as hydrophobic or hydrophilic depending on the contact angle.

Contact angle measurements can determine the surface energy of a solid. Using the Lewis acid/base theory and a set of fluids along with the contact angle, θ, for each fluid, the surface energy can be measured accurately. However, a simple contact angle measurement with water will give an approximate answer [70]. Altering the surface energy through external bonding will change the contact angle of the surface [21]. In the present research, the samples are cleaned to ensure no contaminants affect the process. The surface is coated with polyethylene glycol methacrylate (PEGMA). The surface is then UV radiated, where PEGMA polymerizes. The extent of polymerization can be controlled with the time of exposure, rendering a surface with varying surface energy, and in turn varying contact angle.

2.5 SURFACE ROUGHNESS

The liquid flow characteristics in microchannels are important in the design of MEMS and micro-fluidic devices. There has been a lot of research work done in the area of fluid flow through microchannels, which show that the flow behavior often deviates from the predictions of conventional fluid mechanics theories [82].

Harley and Bau [73] found the product of the friction factor and Reynolds number for the rectangular channels to be 49 and for trapezoidal channels to be 512, when compared to the classical value of 48. The experiments were carried out in rectangular channels of 100 μm in depth, and 50 μm in width, and in trapezoidal microchannels of 33 μm deep, 111 μm top width, and 63 μm bottom width.

Wu and Little [72] measured the friction factor for the flow of gases channels etched in glass and silicon with hydraulic diameters ranging from 55 to 83 μm. They found that the normalized friction constant for all data was greater than unity, indicating higher friction factor than predicted by macroscale theory. The transition to turbulent flow occurred at a Reynolds number as low as 350. They attributed these deviations to high surface roughness caused by the fabrication technique.

Hrnjak and Tu [83] investigated liquid and vapor flow through rectangular microchannels with hydraulic diameters ranging from 69 to 304 μm. They reported that when the channel surface roughness was low, the friction factor and the critical Reynolds number approached the conventional values. As the surface roughness was increased, significant deviation from conventional values and early transition to turbulent flow was observed.

Yu et al. [73] investigated the flow characteristics of dry nitrogen gas and water in microtubes and found the average relative roughness of the tubes to be 53 μm. The

channels were of diameters of 19, 52, and 102 μm. They reported the friction factor to be approximately 0.0003 and for laminar flow, the product of friction factor and Reynolds number to be between 49.35 and 51.56, instead of 64, the reason being the high relative roughness of the channels.

Peng and Peterson [74] reported the flow friction behaviors of both the laminar and turbulent flows to depart from classical correlations for water flows in rectangular microchannels. The experiments were conducted in channels with hydraulic diameters ranging from 133 to 367 μm and aspect ratio from 0.333 to 1. They concluded that the flow transition occurred at Reynolds number 200, and the reason for the deviation to be the surface roughness and not the geometrical parameters, such as hydraulic diameter and aspect ratio.

Mala and Li [76] and Qu et al. [78] investigated flow in trapezoidal silicon microchannels. Experimental results indicated significant deviation from theoretical predictions. In addition, the pressure gradient and flow friction were higher than those given by conventional laminar theory, which was attributed to the surface roughness.

Mala and Li [76] reported the pressure gradients of water flow in large microtubes (150 μm < D < 254 μm) to be in reasonable agreement with conventional theory. In case of smaller microtubes (50 μm < D < 150 μm) the pressure gradients were found to be about 35% higher than those predicted by the conventional theory. The difference between experimental and conventional results increased as the Reynolds number increased, as shown in Figure 2.6. They attributed these effects to surface roughness.

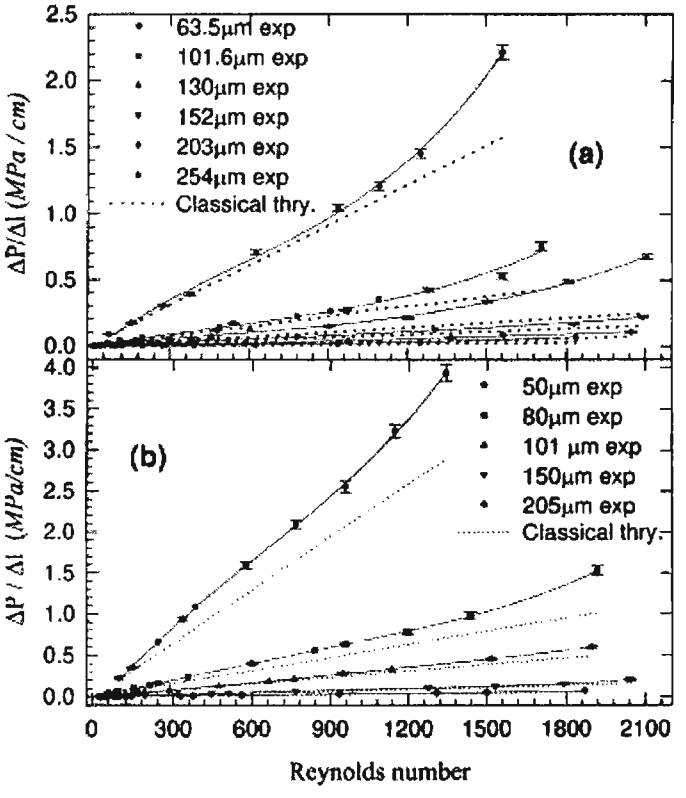

Figure 2.6 Comparison of experimental and classical theory pressure gradient in (a) stainless steel and (b) fused silica microtubes. [76]

Mala and Li proposed a roughness-viscosity to model predict the pressure gradient in microchannels of known surface roughness. According to this concept the value of roughness viscosity, μ_R, should have a higher value near the wall and gradually diminish as the distance from the wall increases.

Most of the published research concentrates on comparison of friction factor between classical theory and experimental data for single-phase flow in microchannels. However, not a lot of work has been done on the effects of surface roughness on two-phase flow in microchannels. Researchers have reported change in flow regimes due to surface roughness and higher pressure drops in rough channels [84-86], but complete

understanding the effect of roughness on two-phase flow is still lacking. Prediction of pressure drop during two-phase flow in a rough microchannel is another area, which requires comprehensive understanding. In the following work includes an attempt made to propose a model that can predict the pressure drop of two-phase flow in microchannels with surface roughness.

3. EXPERIMENTAL METHOD

3.1 MATERIALS

Polydimethylsiloxane and Hamilton Needles were purchased from World Precision Instruments (Sarasota, FL). The photoinitiator 1-hydroxycyclohexyl phenyl ketone (HCPK) and Poly (ethylene glycol) monomethyl ether methacrylate (PEGMA) were purchased from Sigma Aldrich (St Louis, MO). The negative tone photoresist SU-8 (formulation 2150) and SU-8 developer were purchased from MicroChem (Newton, MA).

3.2 CHANNEL FABRICATION

PDMS channels were fabricated to analyze the deviation in pressure drop due to surface roughness. The templates used to fabricate the channels varied in their degree of roughness. The smooth template was fabricated using the photolithography technique. An SU-8 layer was added to a glass wafer by spin coating at 500 rpm for 10 seconds, followed by 2000 rpm for 30 seconds. A prebaking step was carried out at 65°C for 7 minutes followed by 95°C for 45 minutes on a hotplate. The SU-8 initiator was activated by exposure to UV light in a mask aligner for 35 seconds for a total exposure of 525 mJ/cm^2. Post irradiation, the samples were baked at 65°C for 5 minutes and then ramped to 95°C for 15 minutes. The sample was developed using an SU-8 developer for 17 minutes and then rinsed with isopropanol followed by deionized water. The mask used to fabricate the smooth template is shown in Figure 3.1.

The rougher channels were made using Scotch tape and painters tape templates. The tapes were adhered onto a glass slide and layers were added to obtain the required height. The tape was then hand-cut to the required dimensions. The templates as shown in Figure 3.2 were then placed in a Petri dish and filled with PDMS. The dishes were placed in a vacuum desiccator for 14 hours to cure the PDMS, and the cured PDMS was then cut and peeled off. The roughness on the templates was translated onto the channel walls. The channels were finally sealed using a flat PDMS layer with similar roughness, resulting in a sealed rectangular channel with roughness on all the wall surfaces. The three channels were 1000 μm x 250 μm x 6.5 cm (Width x Height x Length) and of different degrees of roughness.

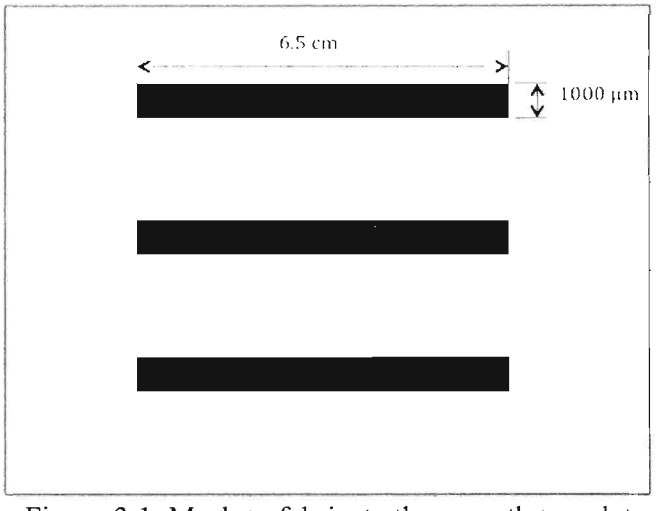

Figure 3.1 Mask to fabricate the smooth template

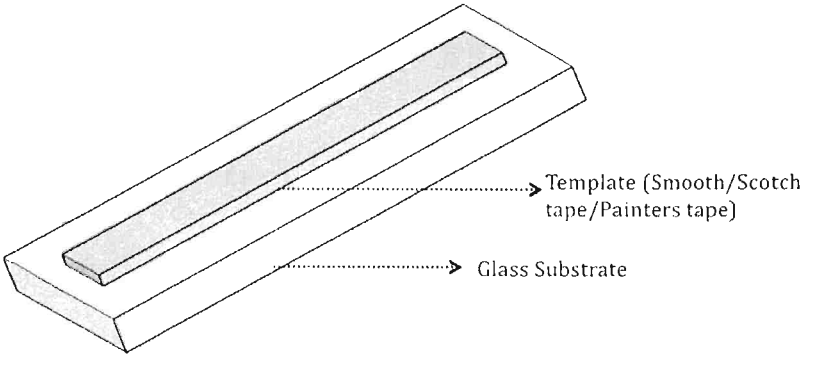

Figure 3.2 Schematic representation of the templates used to fabricate the channels

The smooth channels to study the variation in pressure drop due to hydrophobicity were fabricated in a similar fashion as the smooth template, with the difference being the mask used. The glass substrate was coated with a layer of SU-8 and developed without any pattern. Another coat of SU-8 was applied and developed using the mask shown in Figure 3.3, to ensure the all the surfaces of the channel was SU-8. The top layer was SU-8 coated on a glass substrate and adhered to the patterned sample, resulting in the microchannel shown in Figure 3.4.

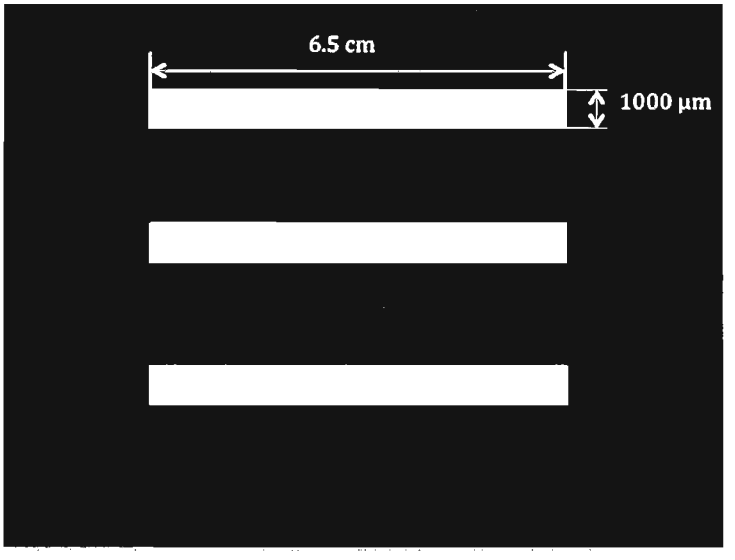

Figure 3.3 Mask to fabricate smooth microchannels

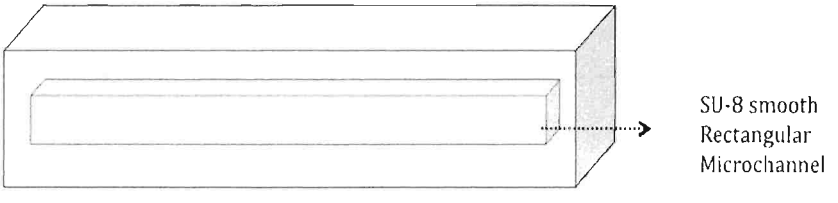

Figure 3.4 Schematic representation of the fabricated smooth microchannels

Prior to adhering the two samples to obtain a sealed microchannel, they were treated to alter the hydrophobicity. The samples were soaked in a 5% solution of HCPK in ethanol (w/w). The samples were placed in nitrogen filled box for 3 hours. The samples were then exposed to UV radiation for 50 minutes for a total exposure of 48600 mJ/cm^2, resulting in formation of surface bound photoinitiator. The excess HCPK was

removed by washing with ethanol. Subsequently, PEGMA was spin coated onto the samples at 1000 rpm for 25 seconds. Exposure to UV radiation for 18, 30, 54, and 72 minutes result in alteration of the water contact angle on SU-8 to 63°, 51°, 35°, and 24°, respectively (21). The water contact angle on untreated SU-8 is 78°, giving five channels of different hydrophobicities. The channels dimensions were 1000 μm x 250 μm x 6.5 cm (Width x Height x Length).

3.3 PRESSURE DROP MEASUREMENT

The PDMS and SU-8 channels were fitted with Hamilton needles. The inlet needle of the channel was connected to a microinfusion pump (Aladdin 1000, World Precision Instruments), while the outlet needle was open to atmosphere. The inlet and outlet tubes were fit with pressure gauges (DTG-6000, 3D instruments) as shown in Figure 3.5. The distance between the needles was maintained at 6 cm for all the channels. This entire setup was placed under a microscope fitted with a CCD camera. The microscope not only aided in measuring the length of the body and caps of the bubble, but also in observing the bubble meniscus and bubble break-up regimes.

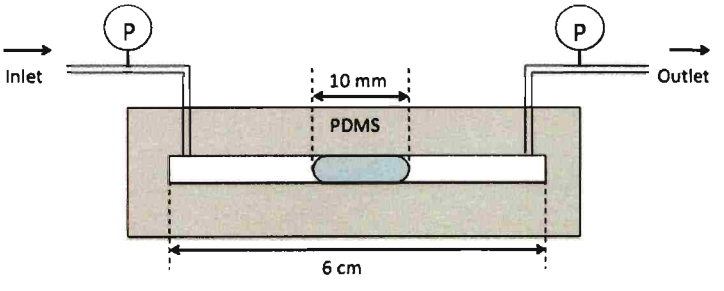

Figure 3.5 Schematic representation of the channel setup

Water was pumped through the channels to maintain a continuous flow. A known volume of air was injected into the tubes to produce a bubble. The bubble flowed through the channel and the pressure drop across the channel was recorded for Reynolds numbers ranging from 0 to 70. The procedure was repeated for the three PDMS channels and the five SU-8 channels. Different bubble sizes (5 mm, 8 mm, 10 mm, 12 mm, and 15 mm) were injected and the pressure drop across each of the channels was recorded. The

data recorded gave the change in pressure drop with change in Reynolds number in each of the eight channels for five different bubble sizes. This pool of data enabled the determination of the effect of channel roughness, hydrophobicity, and bubble size on pressure drop across a rectangular microchannel.

4. ANALYSIS

4.1 THEORETICAL MODEL

Fuerstman developed a model to predict the theoretical pressure drop for two-phase flow in a rectangular microchannel (10). According to the model, the pressure drop across a microchannel with two-phase flow is comprised of three parts, and is shown by Equation (3).

$$\Delta P_{TOTAL} = \Delta P_{SINGLE\,PHASE} + \Delta P_{BUBBLE\,BODY} + \Delta P_{BUBBLE\,CAPS} \tag{3}$$

The single-phase pressure drop is calculated across the length of the channel given by Equation (4).

$$\Delta P_{SINGLE\,PHASE} = \frac{a v \mu L_{SP}}{H^2} \tag{4}$$

where a = W/H, W is the width of the channel, H is the height of the channel, v is the average velocity of the flow, μ is the fluid viscosity, and L_{SP} is difference between the lengths of the channel and the bubble.

The contribution of the body of the bubble to the pressure drop across the channel is given by Equation (5).

$$\Delta P_{BUBBLE\,BOBY} = \frac{v \mu L_{BODY}^3}{H^4} \tag{5}$$

where L_{BODY} is the length of the bubble body.

The pressure drop contribution from the bubble caps is given by Equation (6).

$$\Delta P_{\text{BUBBLE CAP}} = \frac{cv\mu(C_a)^{\frac{1}{3}}}{H} \tag{6}$$

where c = L_{CAPS}/H, L_{CAPS} is the length of the caps, C_a is the Capillary number given by $C_a = \mu v / \sigma$, and 'σ' is the surface tension.

Equation (3) assumes that the bubble fills the entire cross section of the channel, the channel surface is perfectly smooth, and the channel material is perfectly hydrophilic.

4.2 PRESSURE LOSSES

The model developed by Fuerstman et al. [10] gives the theoretical pressure drop across the length of the channel. The experimental setup measures the pressure drop across the channel through the tubing connecting the pressure transducers on either side of the channel, the orifices connecting the tubes to the needles on either side, and the inlet and outlet needles. In addition, the right angle bends at the inlet and the outlet contribute to the pressure loss. The pressure losses due to tubing, the orifices, the needles, and the right angle bends are given by Equations (7), (8), (9), and (10), respectively.

$$\Delta P_{\text{TUBING}} = \frac{4v\mu L}{r^2} \tag{7}$$

where 'L' is the collective length of tubing (15 cm) and 'r' the radius of the tube (2 mm).

$$\Delta P_{\text{ORIFICE}} = \rho Q^2 \left[\frac{1}{A_{\text{NEEDLE}}} - \frac{1}{A_{\text{TUBE}}} \right] \tag{8}$$

where 'Q' is the volumetric flow rate, and A_{NEEDLE} and A_{TUBE} are the cross sectional areas of the needle and tube, respectively.

$$\Delta P_{\text{NEEDLE}} = \frac{4v\mu L_{\text{NEEDLE}}}{r^2_{\text{NEEDLE}}} \tag{9}$$

where 'L_{NEEDLE}' is the collective length of the needles, which (5 cm) and 'r_{NEEDLE}' the radius of the needle (260 μm)

$$\Delta P_{\text{BEND}} = 4\left(\frac{16}{N_{re}}\right)\rho v^2\left(\frac{L}{D}\right)_e \tag{10}$$

where $(L/D)_e$ is 70 for right angle bends [78].

To make a comparison between the model and the experimental data, a summation of all pressure losses should be deducted from the experimental pressure drop.

4.3 PRESSURE DROP VARIATION DUE TO SURFACE ROUGHNESS

Patterning rectangular microchannel molds with photolithography, Scotch tape, and Painters tape produced variations in channel roughness. A profilometer (Alpha-Step 200) was used to quantify the relative heights of asperities on the bottom surface of the channels, and Scanning Electron Microscopy (SEM) was used to view the side walls and the sharpness of the corners, as they contribute to the overall roughness.

Table 4.1 shows that smooth channels were fabricated successfully, and the channels of two different roughnesses were made using the scotch tape and painters tape templates.

Table 4.1 Profilometer Roughness Data of Different Channels

Channel Type	**Roughness (Ra)**
Smooth	332 ± 36 Å
Scotch Tape	4.35 ± 1.20 μm
Painters Tape	11.75 ± 2.68 μm

The channels were fabricated using a peel-off technique, where the bottom layer of the channel was peeled off the template. The technique implemented put a great deal of stress on the surfaces of the channel. The consistency of the surface roughness on the bottom layer and side walls was an important factor to take into consideration. Images from the SEM (Figure 4.1) showed consistent roughness on all channels and well made

side walls. The corners of the scotch tape and painters tape channels were slightly rounded, mainly due to human error involved in making the two templates.

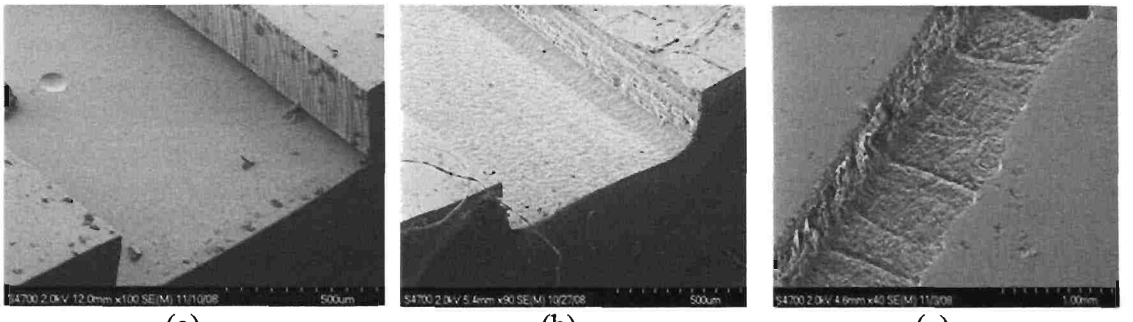

(a) (b) (c)

Figure 4.1 SEM images of rectangular PDMS microchannel surfaces patterns with a) smooth photolithographed template, b) Scotch tape, c) Painters tape

Single-phase pressure drop data were collected in each channel using ambient water and compared to Equation (4.2) for pressure drop through a perfectly smooth hydrophilic channel. It was found that the model underpredicts the pressure drop for all three PDMS channels (Figure 4.2), and that the experimental pressure drop is directly related to the relative surface roughness, as expected. The roughness and hydrophobicity of the channel surface are not included in Equation (4.2), so the hydrophobic PDMS surface used in the experiments is the likely cause of the offset of the photolithographic data from the theoretical model, with the additional offsets for the other two channels being largely a function of surface roughness. The data shown in Figure 4.2 include the deduction of all the pressure losses from the experimental data.

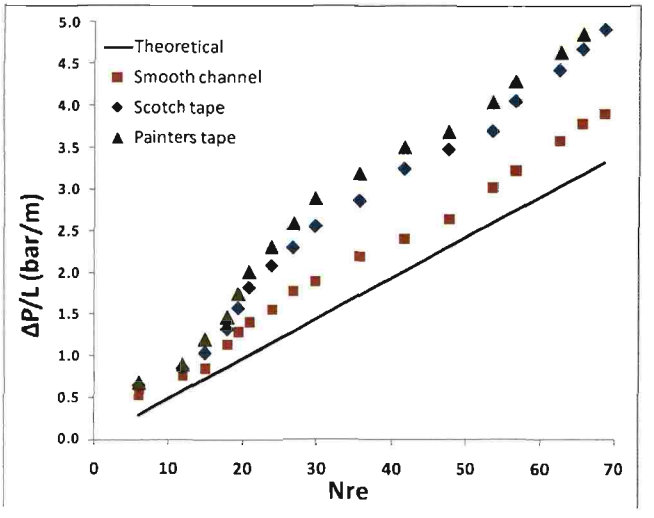

Figure 4.2 Single-phase pressure drop and theoretical prediction

Two-phase pressure drop data were collected after verifying significant changes in pressure drop due to surface roughness in single-phase flow. Data were collected for the various bubble sizes previously discussed. The contact area of the bubble with the channel plays an important role in its behavior. This was evident as the bubble began to break up as the flow rate increased, and it was found that the breakup point in terms of flow rate varied with surface roughness and bubble size. Figure 4.3 shows the two-phase pressure drop across the channel with a 10 mm bubble in it. The pressure drop data acquired by varying the bubble size followed a similar trend to Figure 4.3. The different dotted lines correspond to different breakup regimes observed (Figure 4.4). For a single bubble moving through a rectangular microchannel, four distinct breakup patterns as a function of fluid velocity, with Regime 4 corresponding to the highest fluid velocity, were observed. The breakup of the bubble could also be a function of hydrophobicity, as the contact angle of water on PDMS is 118°. The ability to vary the surface roughness on PDMS channels helps isolate the effect of roughness on pressure drop.

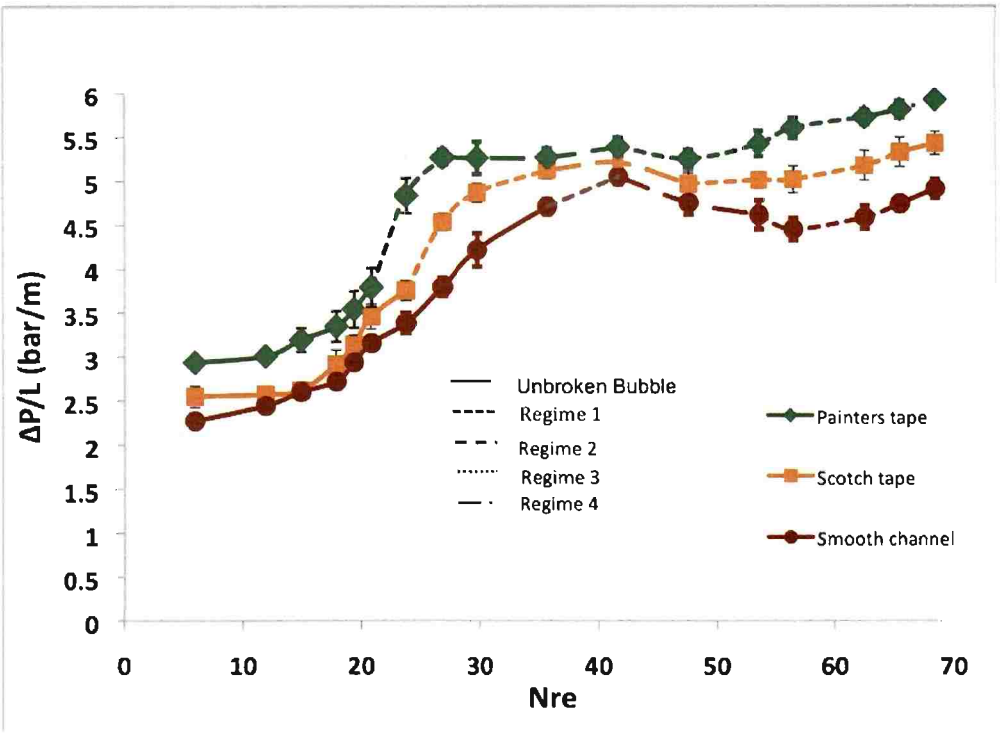

Figure 4.3 Two-phase pressure drop using a 10 mm bubble in different PDMS channels

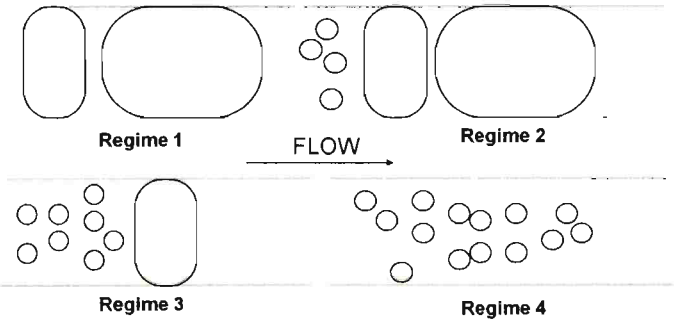

Figure 4.4 Bubble breakup regimes

4.4 PRESSURE DROP VARIATION DUE TO HYDROPHOBICITY

The hydrophobicity of the microchannel surface plays a critical role in the pressure drop across the channel and the bubble breakup. The fluid layer thickness between the channel and the bubble, a strong function of hydrophobicity affects the lubrication and sliding friction of the bubble along the wall. Water has a contact angle of approximately 78° on untreated SU-8. A profilometer was used to check the smoothness of all the SU-8 channels and it was found to be 226 ± 31 Å, which was smoother than the PDMS smooth channels. The ability to modify the surface of SU-8 (21) gives the flexibility to isolate the effect of only hydrophobicity on pressure drop and bubble breakup behavior over a large range of contact angles. Two-phase flow experiments were run in the smooth SU-8 channels and visual observation during data collection showed that the bubble ceased to breakup as the hydrophobicity of the channels was reduced. Hydrophobicity directly affects the bubble mobility and the size of the bubble plays a role in pressure drop, which makes it imperative to include the contact area of the bubble with the channel into the model. The additional term to be incorporated in the existing model is a function of hydrophobicity, roughness, and bubble contact area.

4.5 BUBBLE CONTACT AREA

The bubble contact area is the area of the bubble in contact with the channel walls excluding the bubble caps (Figure 4.5).

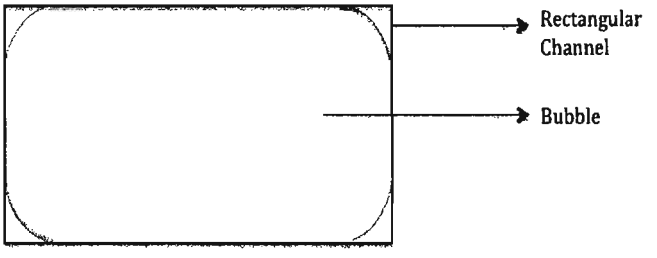

Figure 4.5 Cross sectional view of a bubble in a channel

The determination of the bubble contact area begins by measuring the volume of the bubble. The volume of air dispensed to form the bubble of the desired length is assumed to be the volume of the bubble. The volume of the bubble cap was calculated using Equation (11).

$$V_C = \frac{\pi D_h h_c}{3} \tag{11}$$

where D_h is the hydraulic diameter of the channel and h_C the length of the cap.

The volume of the body of the bubble was determined using Equation (12)

$$V_B = V_D - V_C \tag{12}$$

where V_D is the volume of the bubble and V_C the volume of the caps.

Assuming the bubble shape at the corners to be linear, the cross sectional area of the four corner sectors are estimated using Equation (13)

$$A_R = A_C - A_B \tag{13}$$

where A_c is the cross sectional area of the rectangular channel and A_B is the cross sectional area of the bubble, calculated by dividing the volume of the body of the bubble by the length of the body of the bubble. Subsequently, the area of each sector is calculated by dividing the total area of the corner sectors by four. Assuming that each sector is an isosceles right triangle of equal area, the length of the sides of the triangle can be determined (Figure 4.6). The contact area of the bubble with the channel was then determined using Equation (14).

$$S_B = \left[2(H - 2l_b) + 2(W - 2l_b)\right]L_{BODY} \tag{14}$$

where H is the height of the channel, W is the width of the channel, and l_B is the length of the sides of the triangle.

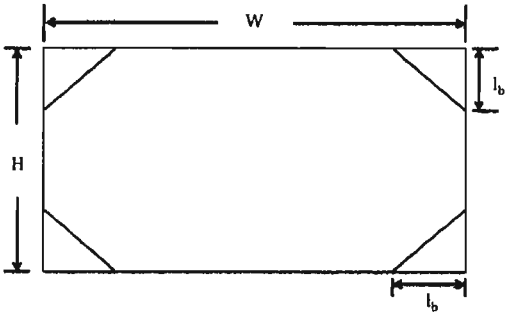

Figure 4.6 Cross sectional view of the assumption that the corners of the bubble are straight and not curved.

5. RESULTS AND DISCUSSION

5.1 EFFECT OF HYDROPHOBICITY ON PRESSURE DROP

Pressure drop data were collected in each channel with varying hydrophobicity (78°, 63°, 51°, 35°, and 24°) using different bubble sizes (5 mm, 8 mm, 10 mm, 12 mm, and 15 mm). The data showed that pressure drop increases with increasing hydrophobicity. These data are compared to the theoretical data values. The 24° contact angle channel, which is the most hydrophilic, closely matches the theoretical data, which assumes that the channel is smooth and completely hydrophilic, for all the bubble sizes. Figures 5.1-5.5 show the pressure drop versus N_{RE} data.

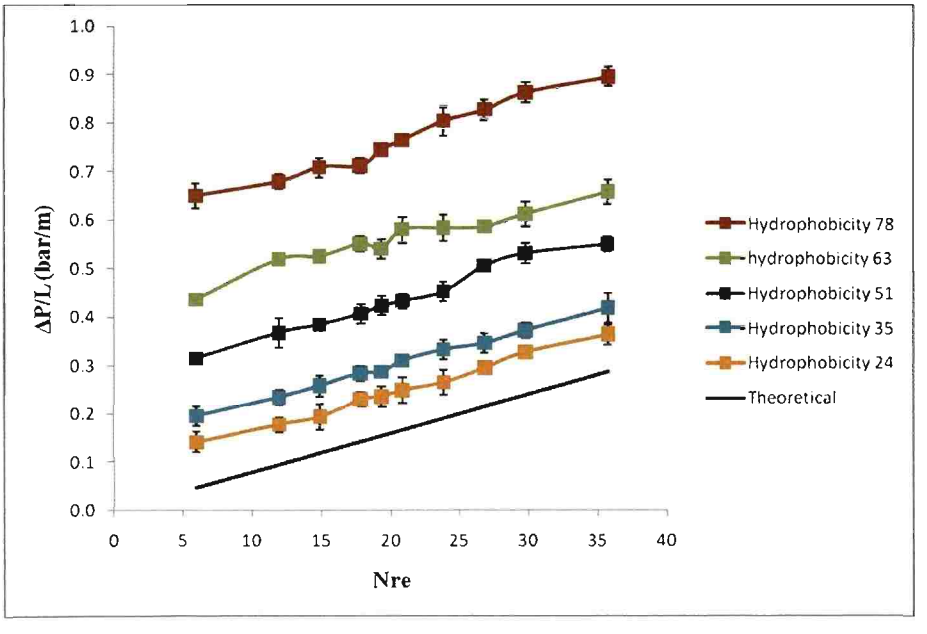

Figure 5.1 Pressure drop across smooth SU-8 channels with varying hydrophobicity using 5 mm bubble

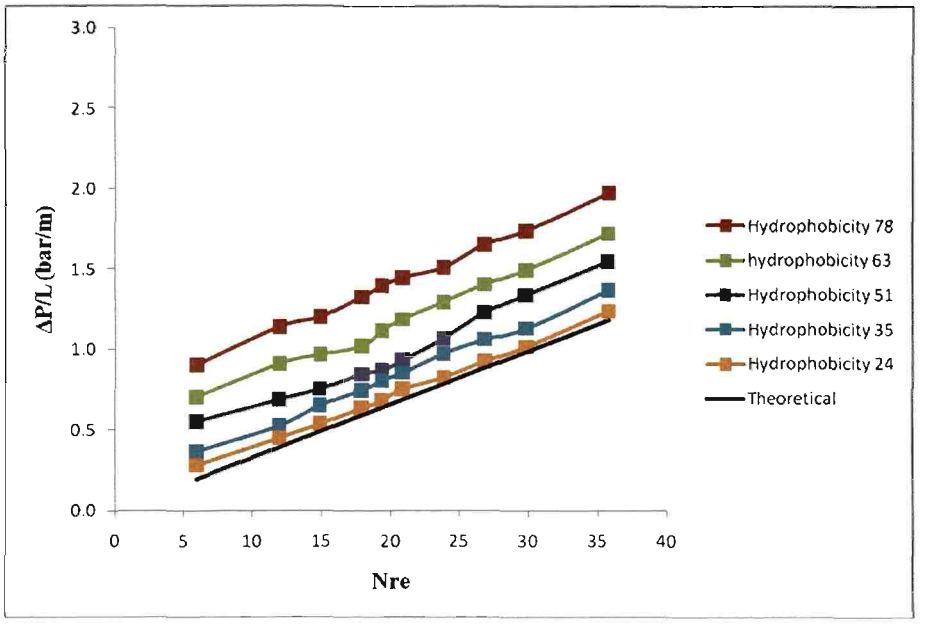

Figure 5.2 Pressure drop across smooth SU-8 channels with varying hydrophobicity using 8 mm bubble

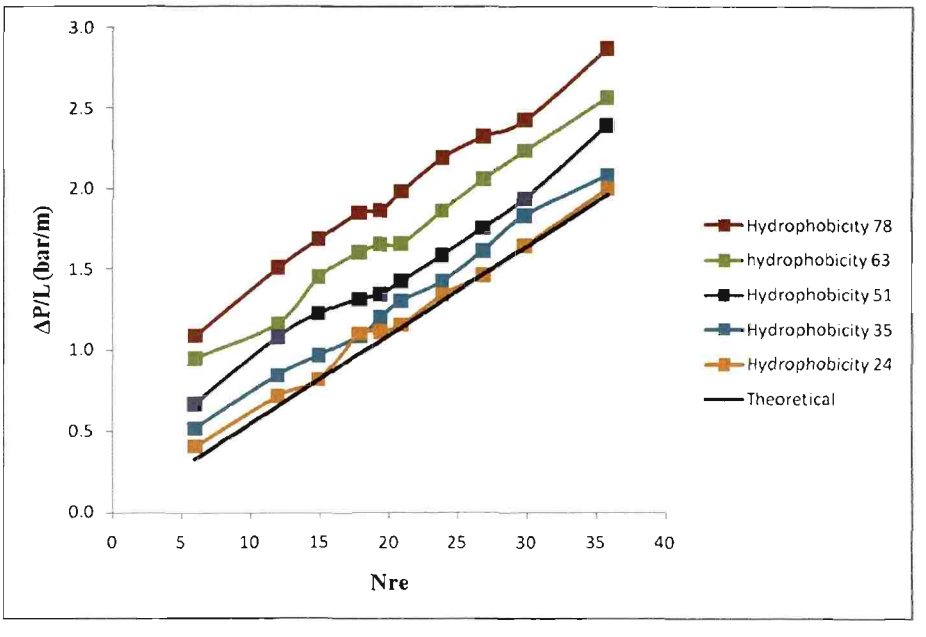

Figure 5.3 Pressure drop across smooth SU-8 channels with varying hydrophobicity using 10 mm bubble

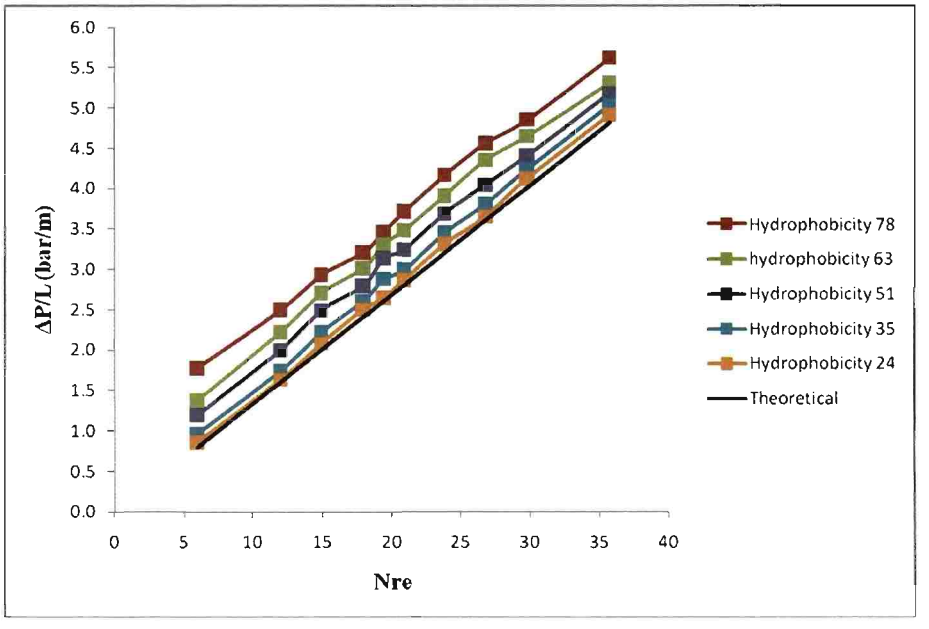

Figure 5.4 Pressure drop across smooth SU-8 channels with varying hydrophobicity using 12 mm bubble

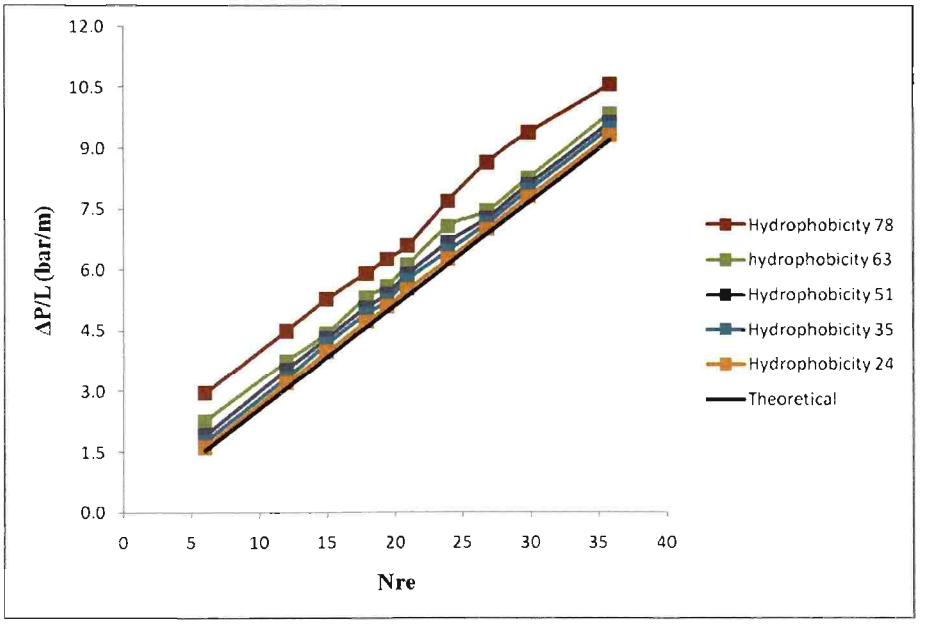

Figure 5.5 Pressure drop across smooth SU-8 channels with varying hydrophobicity using 15 mm bubble

Measurements show a higher pressure drop in hydrophobic channels compared to hydrophilic channels. The reason is that in hydrophobic channels, the channel wall is not completely wettable to the liquid phase, giving rise to a stable contact point where the liquid, vapor and the solid are in contact. Driving a bubble through a hydrophobic channel involves overcoming high wall adhesion forces due to the contact angle hysteresis. In hydrophilic channels, the channels wall is covered by a film of liquid which induces no wall adhesion forces. Driving a bubble through a hydrophilic channel involves only balancing of the viscous forces. The observed data shows as the hydrophobicity decreases the pressure drop is similar to the predicted pressure drop in a completely hydrophilic channel. The hydrophobicity dependence of the pressure drop can be attributed to the difference in flow patterns.

Figures 5.1-5.5 show the effect of hydrophobicity on pressure drop at constant bubble sizes. Figure 5.6 shows that at constant hydrophobicity, an increase in bubble size increases the pressure drop. Figures 5.1-5.6 show that both hydrophobicity and bubble size affects the pressure drop in a microchannel. The theoretical pressure drop considers bubble dimensions in the calculation, but the relation between bubble size and hydrophobicity is a factor that needs to be considered, which is the reason for considering bubble size and hydrophobicity in the additional term of the model to be proposed.

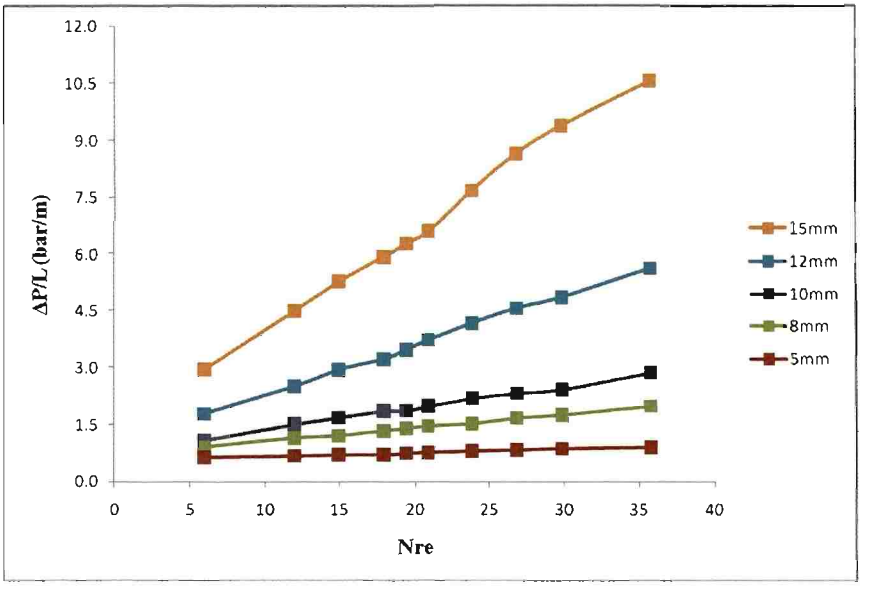

Figure 5.6 Pressure drop across 78° contact angle SU-8 channel for varying bubble sizes

5.2 INCLUSION OF HYDROPHOBICITY AND BUBBLE CONTACT AREA INTO THE MODEL

The data were analyzed to incorporate the effects of hydrophobicity and bubble contact angle into the model. The pressure drop model was curve fitted against the recorded experimental pressure drop data, shown by Equation 15.

$$\Delta P_H = a\Delta P_M + b \tag{15}$$

where ΔP_H is the recorded pressure drop on channels with different hydrophobicities, ΔP_M is the pressure drop calculated using the model, and 'a' and 'b' are coefficients. The coefficients 'a' and 'b' are shown in Table 5.1.

Table 5.1 Coefficients 'a' and 'b' for different hydrophobicities and bubble sizes

		HYDROPHOBICITY									
		78		63		51		35		24	
		a	b	a	b	a	b	a	b	a	b
BUBBLE SIZE (mm)	5	1.123	0.5759	0.8514	0.4354	1.06	0.2577	0.9477	0.1356	1.061	0.05563
	8	1.062	0.7016	1.032	0.4847	1.05	0.3025	1.016	0.1536	0.9611	0.0621
	10	1.042	0.7951	1.001	0.5431	0.9834	0.3362	0.9739	0.1618	0.9632	0.0676
	12	0.9772	0.9548	0.9946	0.6403	0.9938	0.4072	1.019	0.1949	1.015	0.0818
	15	1.027	1.299	0.9939	0.7269	1.002	0.4644	1.006	0.238	1.003	0.0911

Coefficient 'a' can be approximated as 1, and coefficient 'b' is curve fitted with the bubble contact area shown by Equation 16.

$$b = ce^{dS_B} \tag{16}$$

where S_B is the bubble contact area and 'c' and 'd' are coefficients of the curve fit shown in Table 5.2.

Table 5.2 Calculated bubble contact area and coefficients 'c' and 'd' for corresponding bubble sizes

Syringe Pump Volume (cc)	Bubble Size (mm)	Bubble Contact Area (cm^2)	c	d
0.00142	5	0.0739	0.4203	3.991
0.00221	8	0.1274	0.3594	3.565
0.00287	10	0.1552	0.2126	3.861
0.00367	12	0.2184	0.1066	3.842
0.00449	15	0.2781	0.0461	3.496

The coefficient 'c' is curve fitted with the hydrophobicity, shown by Equation 17. The contact angle of the channels is converted into radians to enable a better fit, shown in Table 5.3.

$$c = lh^k \tag{17}$$

where h is the contact angle in radians, and 'l' and 'k' are coefficients.

Table 5.3 Contact angle in degrees and radians

Contact Angle in Degrees	Contact Angle in Radians
78	1.3606
63	1.0990
51	0.8800
35	0.5931
24	0.4361

Equation 18 gives the proposed model including the hydrophobicity and bubble contact area terms.

$$\Delta P_H = \Delta P_M + lh^k e^{dS_B} \tag{18}$$

The coefficients 'l' and 'k' are calculated to be 0.2687 and 1.635, respectively. The coefficient 'd' has five values and the optimum value of 'd' was determined by substituting each value of 'd' into Equation 18, and calculating the error between the proposed model and the experimental data. Figure 5.7 shows the frequency of the error for the value of 'd' that had the best fit. The proposed model was compared against the experimental data for different bubble sizes in all contact angle channels. The majority of the error was within ±10%, which is acceptable considering the experimental setup and the pressure losses involved. Figure 5.8 shows the comparison between the theoretical model, proposed model, and the experimental data. The corrected model fit well with the experimental data for the range of parameters studied here. The curve fittings obtained to

arrive at the proposed model are shown in Appendix A. Equation 19 gives the proposed model incorporating the hydrophobicity and bubble contact area terms.

$$\Delta P_H = \Delta P_M + 0.2687 h^{1.635} e^{3.991 S_B} \tag{19}$$

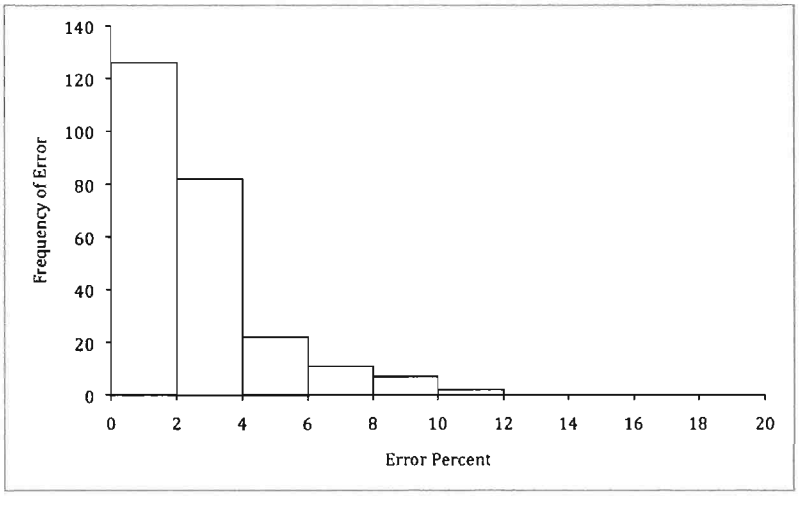

Figure 5.7 Frequency of error calculated between the proposed model and experimental data

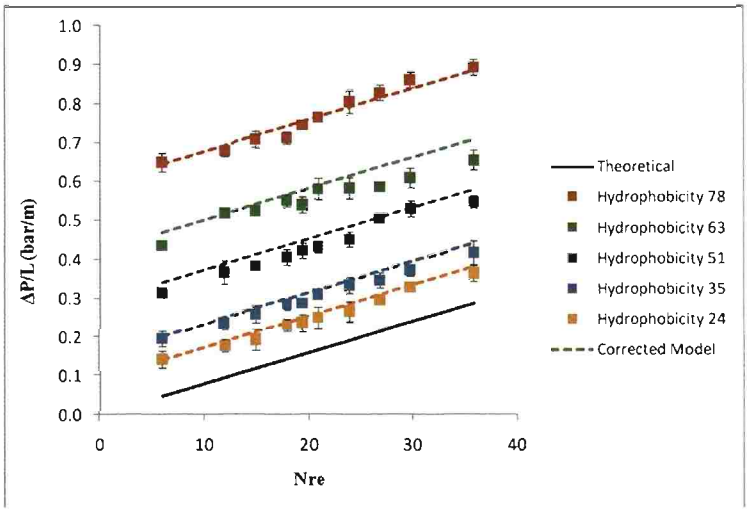

Figure 5.8 Theoretical model, proposed model, and experimental data comparison in smooth SU-8 channels using 5 mm bubble

5.3 VALIDATION OF THE MODEL

The model proposed to theoretically predict the pressure drop across a rectangular microchannel for two-phase flow, for varying hydrophobicity and bubble size, was validated using channels of only one dimension (1000 μm x 250 μm x 6.5 cm), having an aspect ratio of 4. Channels of varying aspect ratios (2, 4, 6, 10, 16, and 20) were fabricated and the hydrophobicity of each channel was altered. Two-phase flow experiments were run in each channel and the pressure drop across the channels for varying bubble size and hydrophobicity were recorded.

The results fit the proposed model within an error of ±10%. The Figures 5.9-5.13 show the frequency of error between the proposed model and the experimental data.

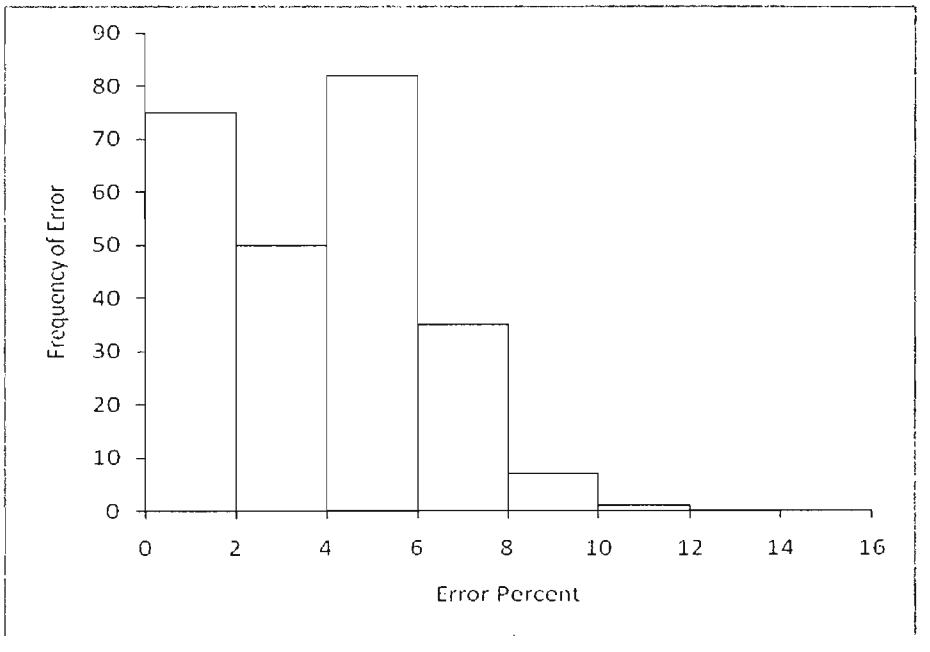

Figure 5.9 Frequency of error calculated between the proposed model and experimental data for a channel of aspect ratio 2 (500 μm x 250 μm x 6.5 cm)

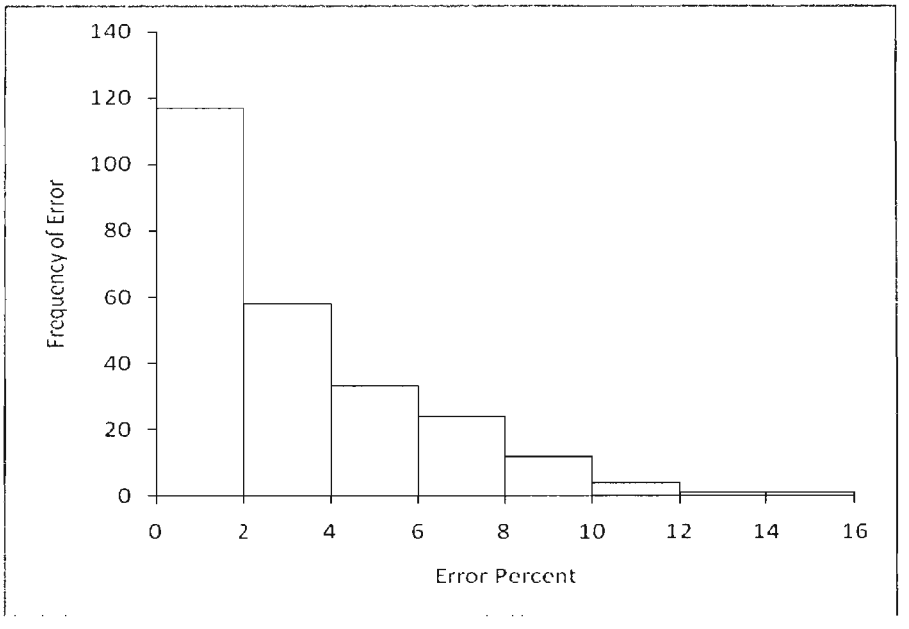

Figure 5.10 Frequency of error calculated between the proposed model and experimental data for a channel of aspect ratio 6 (1200 μm x 200 μm x 6.5 cm)

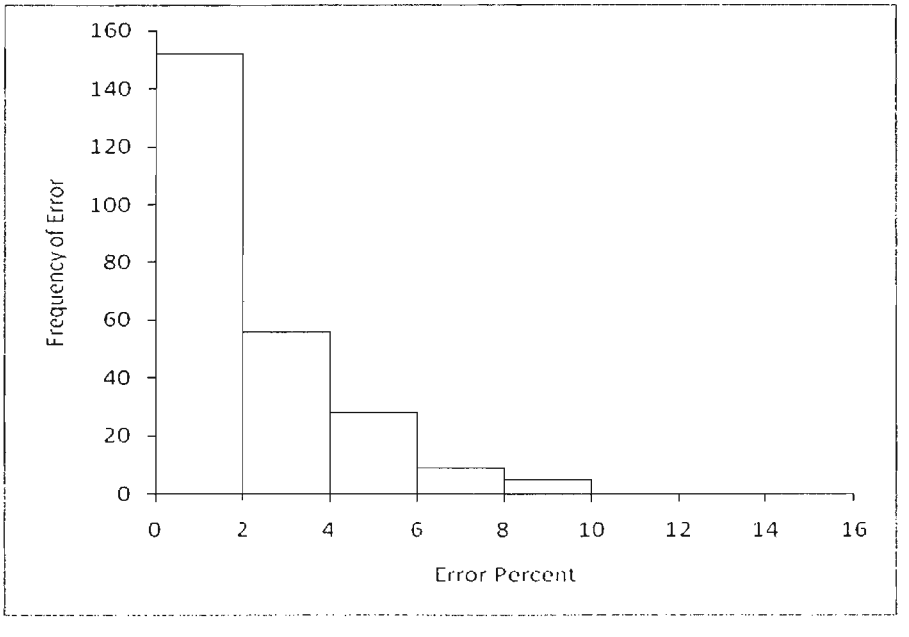

Figure 5.11 Frequency of error calculated between the proposed model and experimental data for a channel of aspect ratio 10 (2500 μm x 250 μm x 6.5 cm)

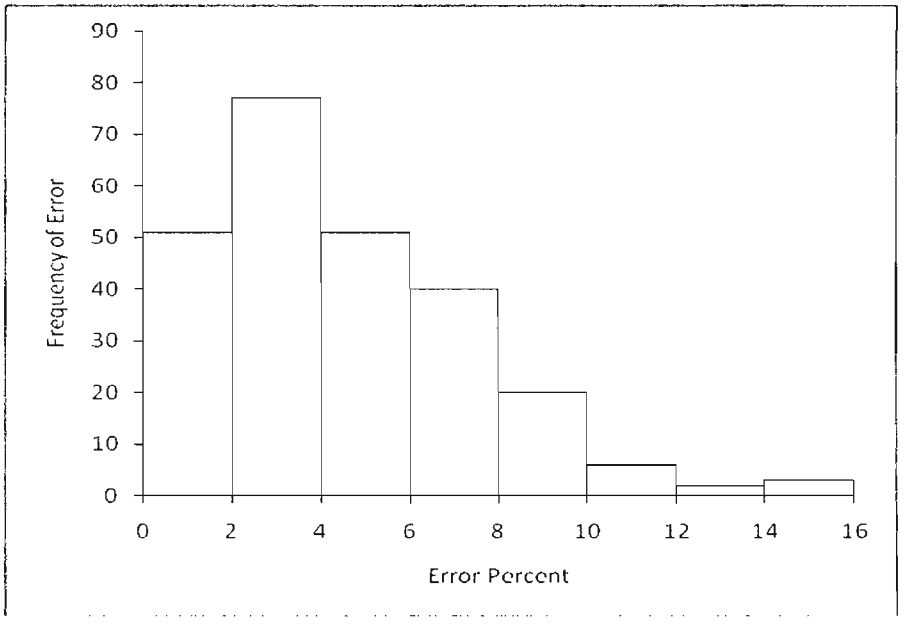

Figure 5.12 Frequency of error calculated between the proposed model and experimental data for a channel of aspect ratio 16 (4000 μm x 250 μm x 6.5 cm)

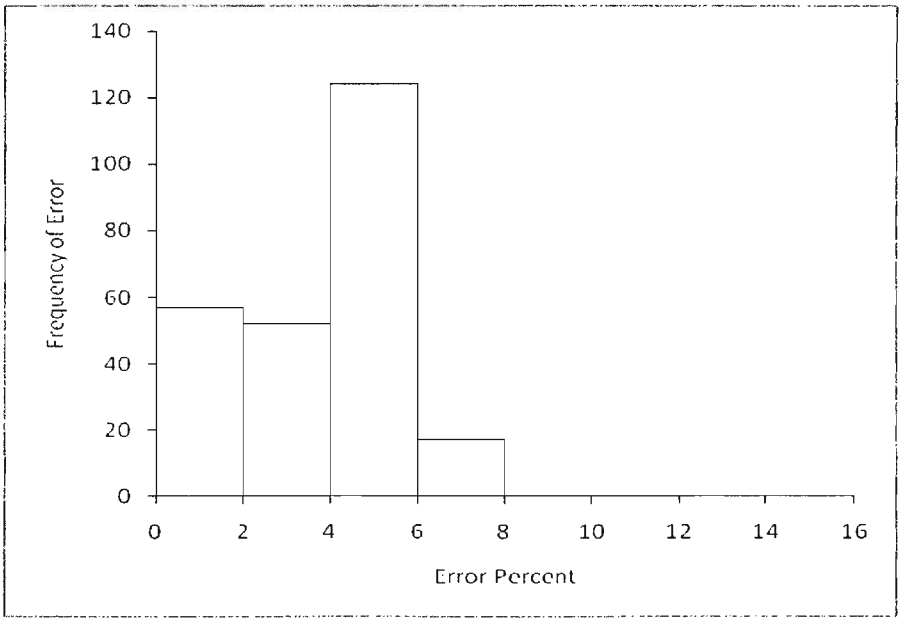

Figure 5.13 Frequency of error calculated between the proposed model and experimental data for a channel of aspect ratio 20 (4000 μm x 200 μm x 6.5 cm)

The graphs comparing the pressure drop in each channel for varying hydrophobicity and bubble size against the theoretical model and the proposed model are shown in Appendix B. The graphs clearly indicate that an error of ±10% is acceptable. The pressure drop in the channels closely traces the proposed pressure drop. There are certain values that deviate more than the acceptable error, which can be attributed to experimental error and accuracy of the pressure sensor. The proposed model predicts the pressure drop in channels of all aspect ratios. The aspect ratio does not have an effect on the pressure drop prediction.

Fabrication of the channels with different aspect ratios had certain physical limitations. The width of the channels ranged from 500 μm to 4000 μm, and the height ranged from 200 μm to 250 μm. The limitation with respect to the width of the channels was the inability to fabricate channels less than 500 μm. Hamilton needles were used to inject the liquid and the bubble into the channels. The needles were of a diameter of 260 μm, and sufficient clearance from the walls of the channels was required for the stability of the microchannels. The height of the channels was not more than 250 μm, because the lithography process had the limitation of being able to develop SU-8 2150 under almost ideal conditions up to a height of 300 μm from a single coat. The height of the channels could be reduced below 200 μm but with the limitation faced with respect to the width of the channels, the channels appeared more like flat slits when the height was reduced. The stability of the bubble in these channels, especially in the hydrophobic ones, was very low. The bubble began to breakup at very low Reynolds numbers because of the amplified effect of the wall adhesion forces.

5.4 EFFECT OF SURFACE ROUGHNESS ON PRESSURE DROP

The pressure drop data were recorded for two-phase flow in smooth PDMS microchannels. The contact angle of water on PDMS is 118°. The proposed model was compared with the experimental data. The model could not predict the pressure drop across two-phase flow in PDMS channels (Figure 5.14). The reason the proposed model was not able to predict the pressure drop could be because of the change in material of channel or that the model has the limitation of not being accurate under extremely hydrophobic conditions, with the latter being more likely. The hydrophobicity of the PDMS channel was outside the range of the contact angle parameter in the proposed model. Extrapolating to predict the pressure drop in the PDMS channels was unsuccessful.

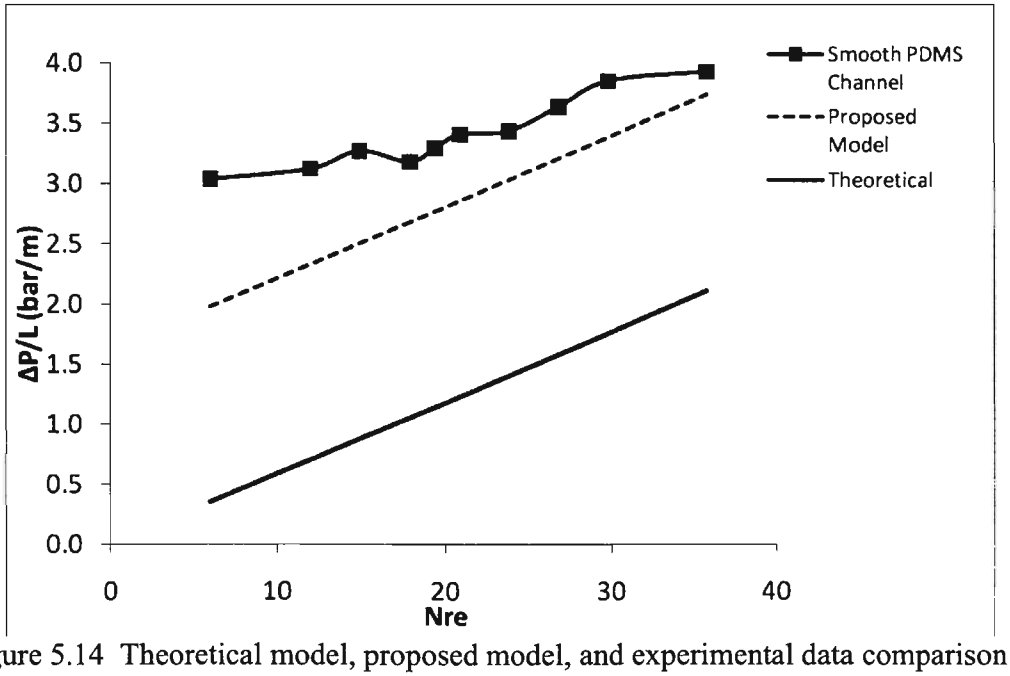

Figure 5.14 Theoretical model, proposed model, and experimental data comparison in smooth PDMS channel using 10 mm bubble

To understand this limitation better, an idea to fabricate rough SU-8 channels was proposed. Figure 5.15 shows the steps followed to fabricate rough SU-8 channels. Fabrication of the bottom section of the channel began with preparing a template using a rough tape similar to the one shown in Figure 3.2. The template was then placed in a Petri dish; PDMS was then poured and cured. The PDMS was peeled off to give a rectangular well with roughness from the tape translated onto the bottom surface. The PDMS structure was then coated with positive resist and then baked at 65°C for 4 minutes. It was then baked again for 35 minutes at 90°C. The PDMS was then peeled off, resulting in a template made of positive resist with the roughness on the PDMS surface translated onto the surface of the positive resist. The positive resist template was then coated with SU-8, which is baked for 7 minutes at 65°C, followed by baking at 95°C for 40 minutes. During the baking process, a glass slide was carefully place on the SU-8 when it had been partially cured, providing stability and strength to the structure. After the curing process the positive resist was dissolved using an etchant, resulting in the bottom section of the microchannel with roughness from the positive resist being translated onto the SU-8 surface.

The top surface of the channel was fabricated in a similar fashion, with the difference being the initial template used. In this case, the entire glass slide was taped, giving a flat surface with roughness on it. The previous mentioned procedure was followed, obtaining the top surface of the channel. The two sections were then attached using epoxy giving a SU-8 microchannel with rough walls. Using different kinds of tapes in the initial template prepared can change the roughness of the walls.

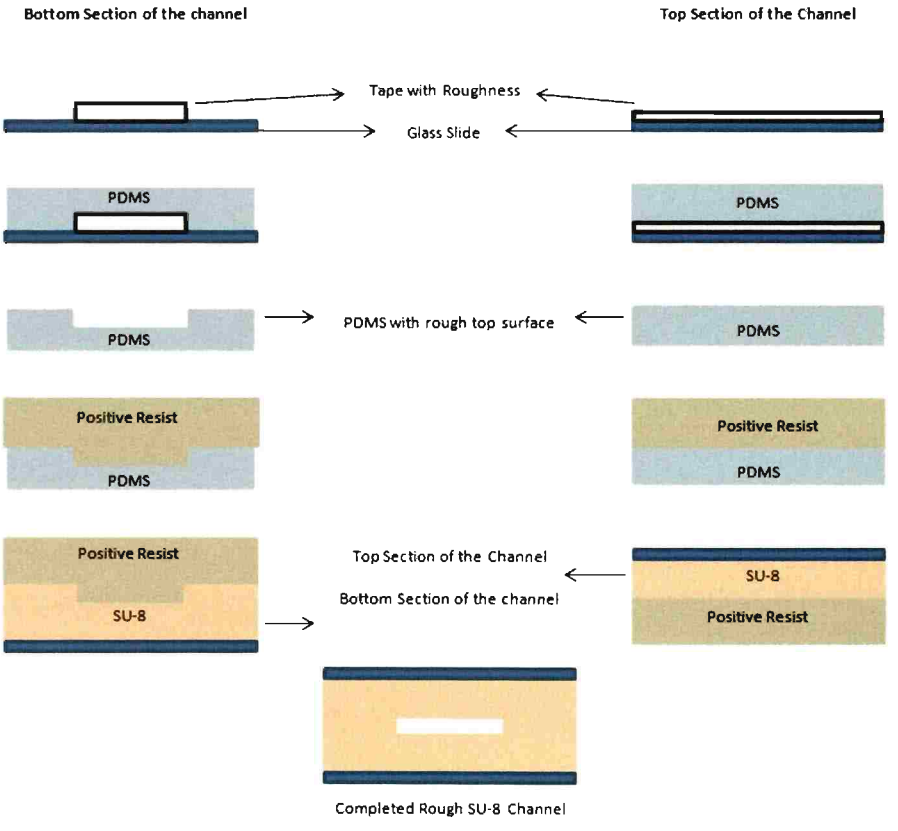

Figure 5.15 Schematic representation of fabrication of rough SU-8 microchannels

6. CONCLUSIONS

1. Hydrophobicity, surface roughness, and bubble size play an important role in bubble transport across a rectangular microchannel.

2. The channels were successfully fabricated to study the pressure drop variation due to these factors.

3. Two different materials (PDMS and SU-8) needed to be used to fabricate the channels. Altering the hydrophobicity of the PDMS channels was difficult. Hence, SU-8 was used to fabricate channels with different hydrophobicities. SU-8 channels had the limitation of not being able to translate roughness onto the channels walls.

4. A model was proposed to theoretically predict the pressure drop across a rectangular microchannel for two-phase flow, for varying hydrophobicity and bubble size. The proposed model successfully predicted the pressure drop for the given set of conditions.

5. The proposed model was validated by successfully predicting the pressure drop for varying hydrophobicity and bubble size across rectangular microchannels with varying aspect ratios.

6. The proposed model failed to successfully predict the pressure drop across PDMS rectangular microchannels. The reason the proposed model was not able to predict the pressure drop could be because of the change in material of channel or the model has the limitation of not being accurate under super hydrophobic conditions, with the latter being the more likely.

7. A method to fabricate rough SU-8 channels was proposed. The fabricated channels can be used to study the deviation of pressure drop due to surface roughness and include a surface roughness term into the presently proposed model.

APPENDIX A

CURVE FITTING PLOTS

The curve fitting plots obtained from Equation 15 are show in Figures A.1-A.21.

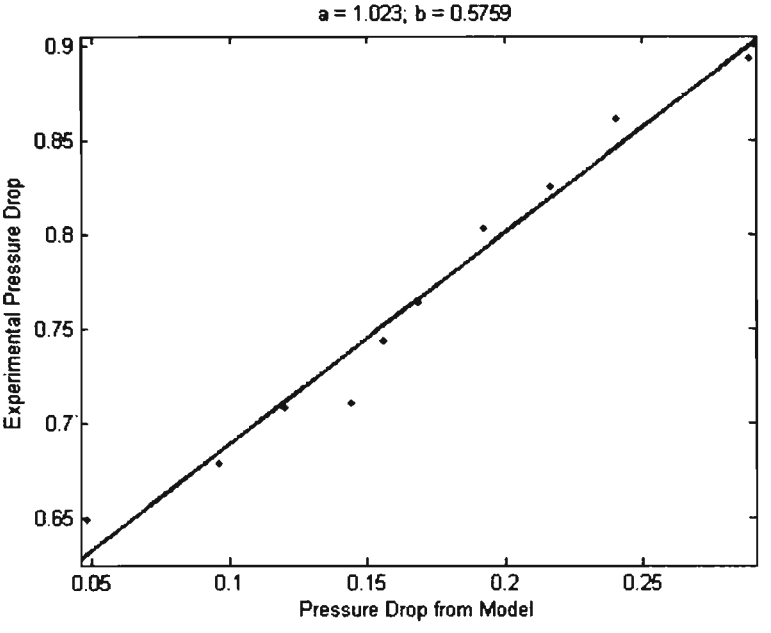

Figure A.1 Curve fitting plot of 78^0 contact angle channel using 5 mm bubble

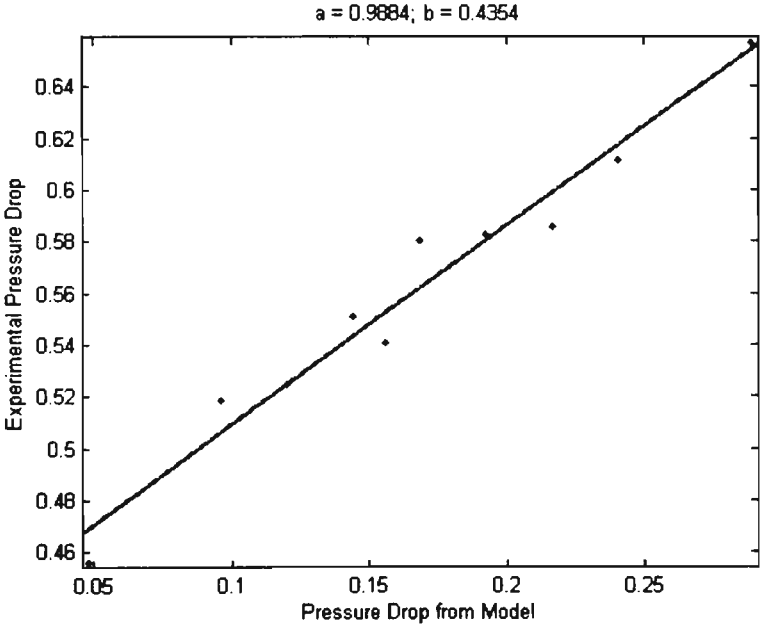

Figure A.2 Curve fitting plot of 63^0 contact angle channel using 5 mm bubble

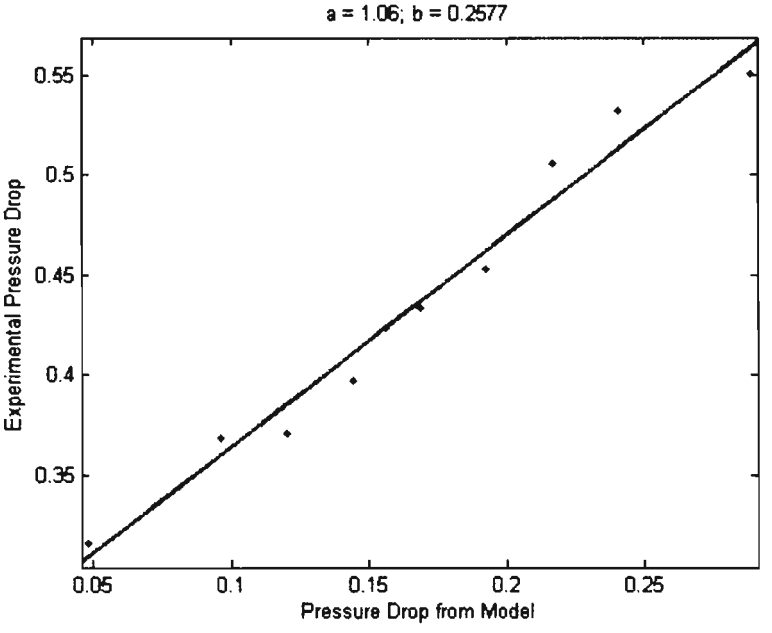

Figure A.3 Curve fitting plot of 51^0 contact angle channel using 5 mm bubble

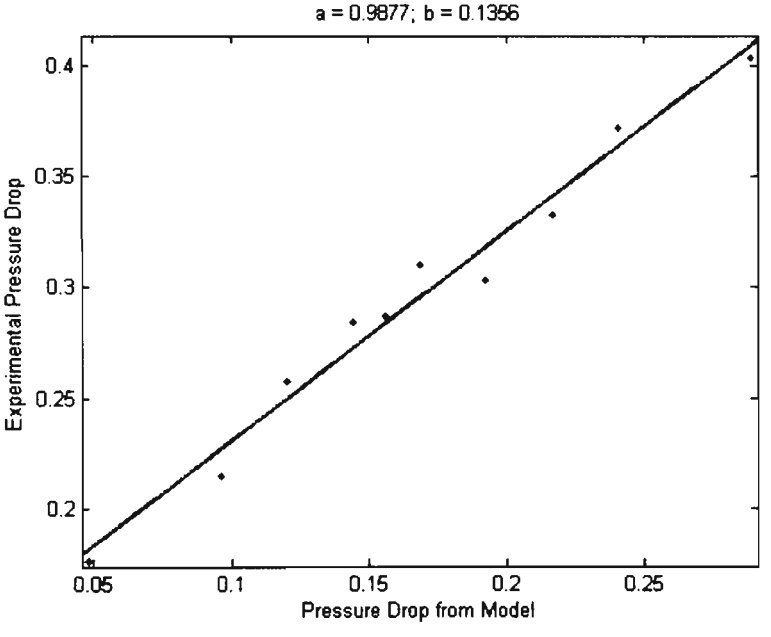

Figure A.4 Curve fitting plot of 35^0 contact angle channel using 5 mm bubble

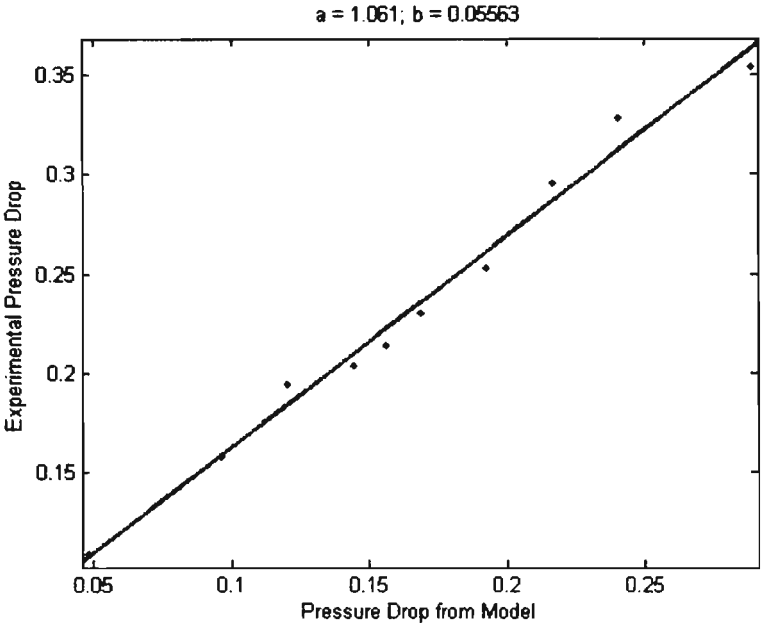

Figure A.5 Curve fitting plot of 24^0 contact angle channel using 5 mm bubble

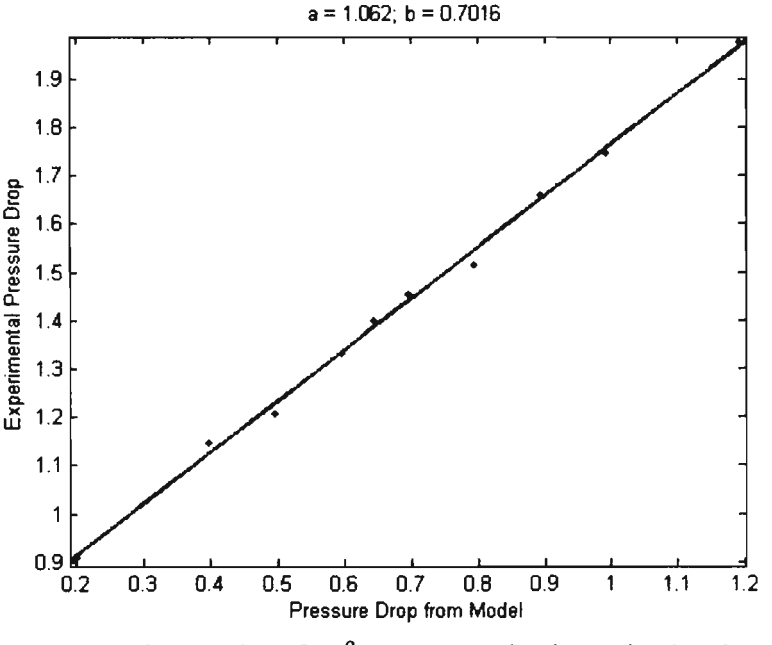

Figure A.6 Curve fitting plot of 78^0 contact angle channel using 8 mm bubble

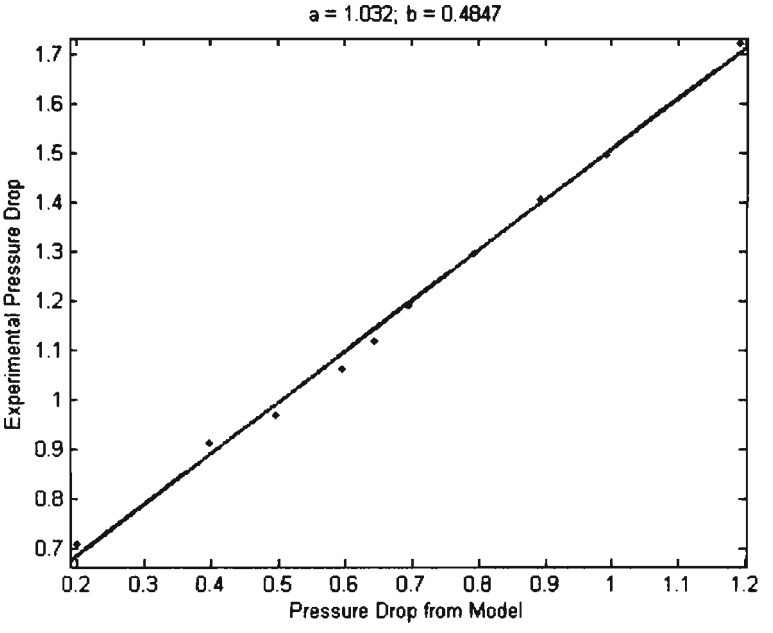

Figure A.7 Curve fitting plot of 63^0 contact angle channel using 8 mm bubble

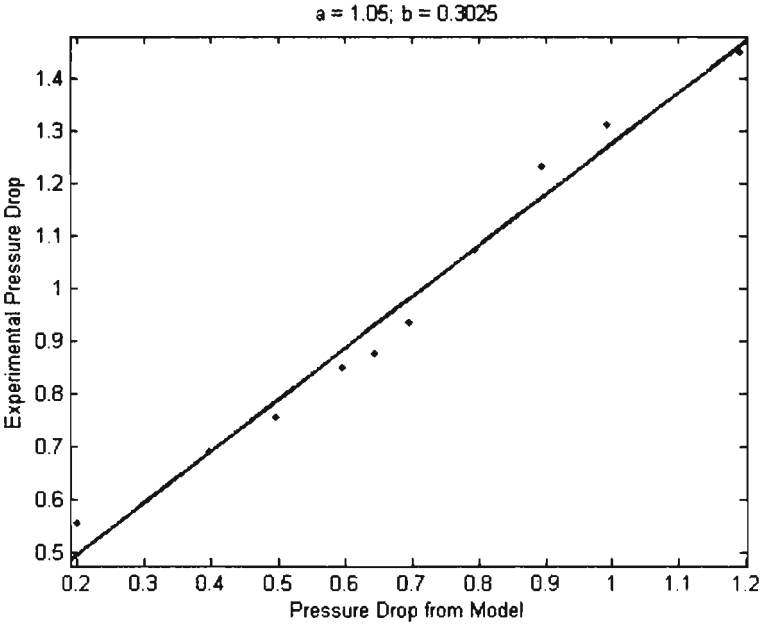

Figure A.8 Curve fitting plot of 51^0 contact angle channel using 8 mm bubble

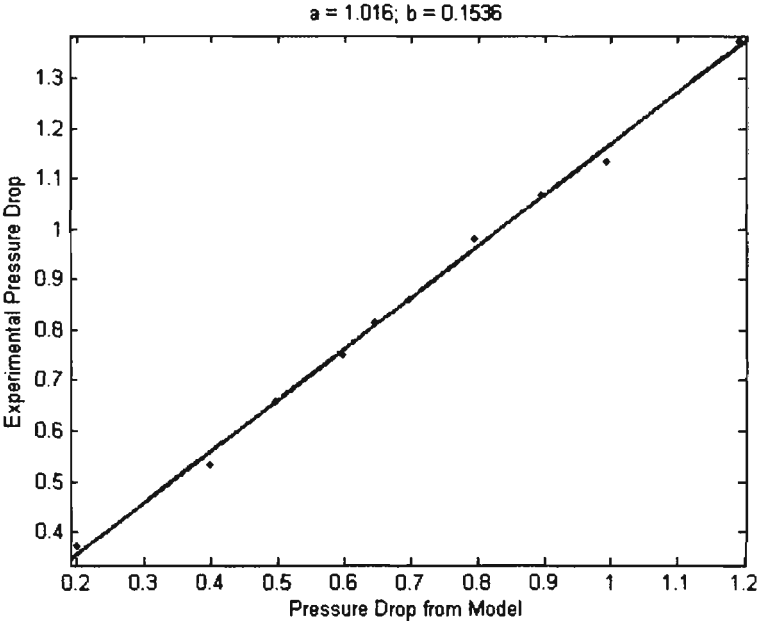

Figure A.9 Curve fitting plot of 35^0 contact angle channel using 8 mm bubble

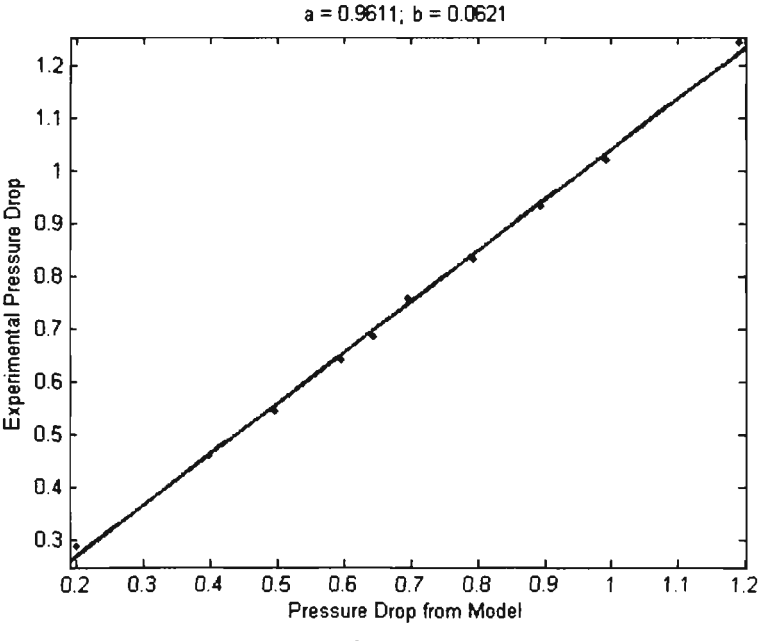

Figure A.10 Curve fitting plot of 24^0 contact angle channel using 8 mm bubble

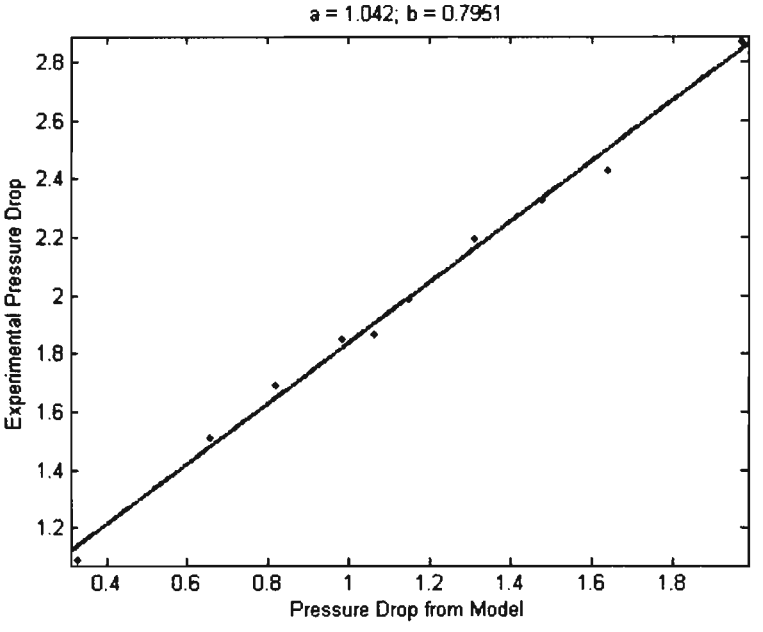

Figure A.11 Curve fitting plot of 78^0 contact angle channel using 10 mm bubble

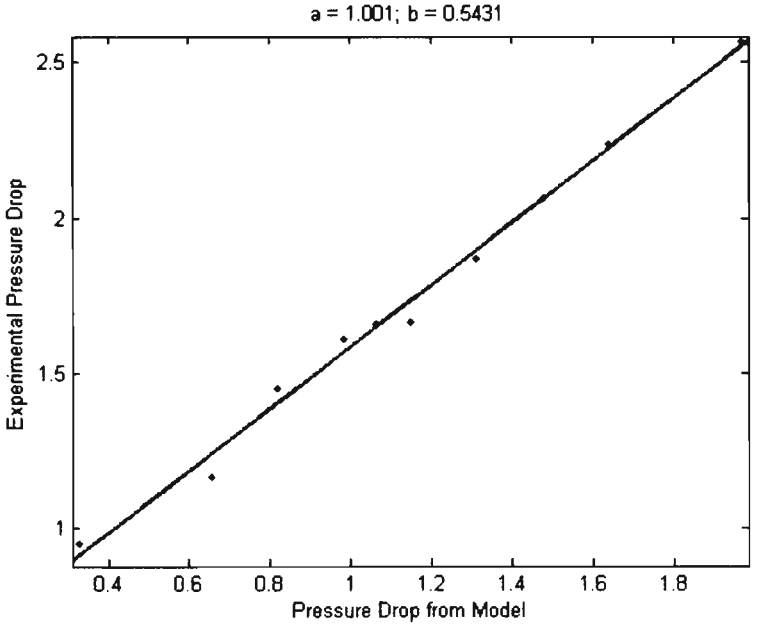

Figure A.12 Curve fitting plot of 63^0 contact angle channel using 10 mm bubble

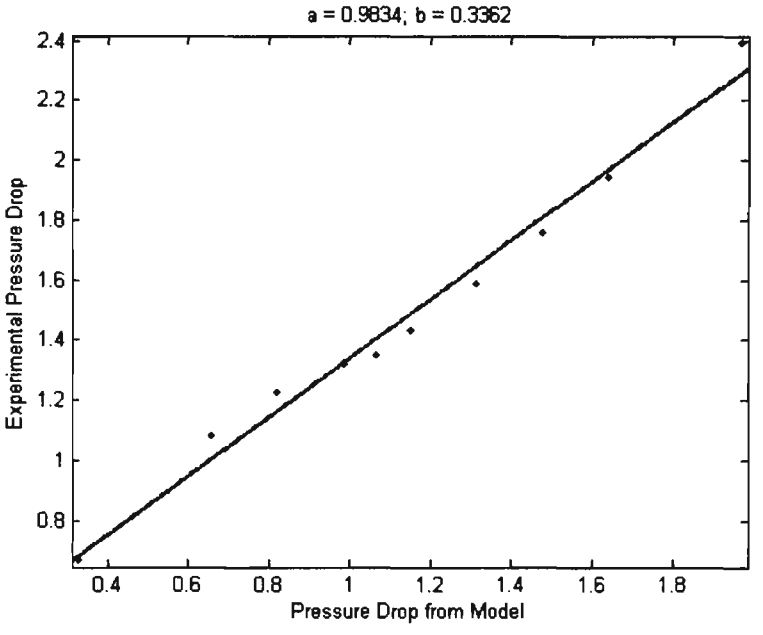

Figure A.13 Curve fitting plot of 51^0 contact angle channel using 10 mm bubble

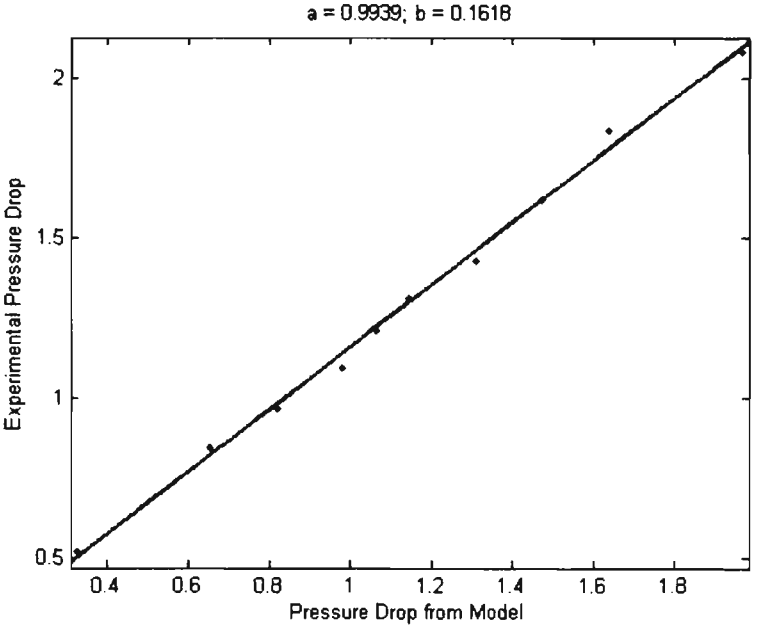

Figure A.14 Curve fitting plot of 35^0 contact angle channel using 10 mm bubble

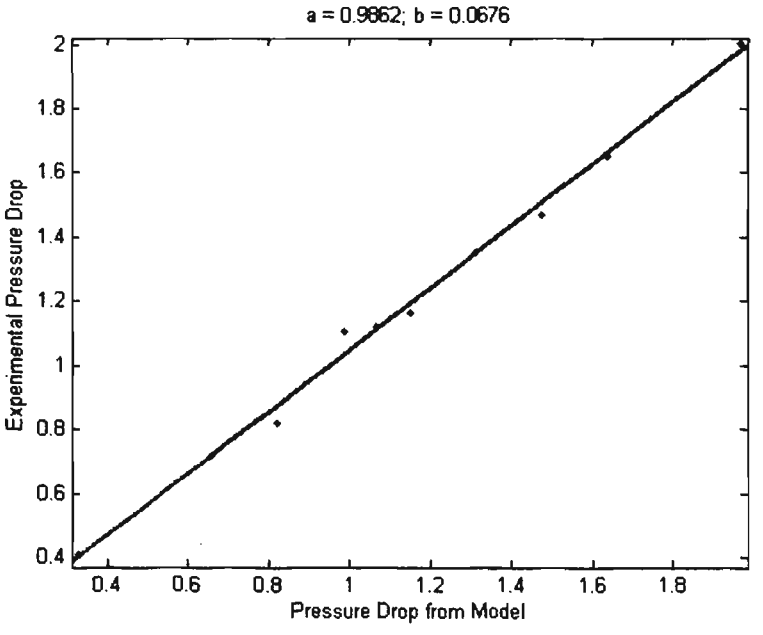

Figure A.15 Curve fitting plot of 24^0 contact angle channel using 10 mm bubble

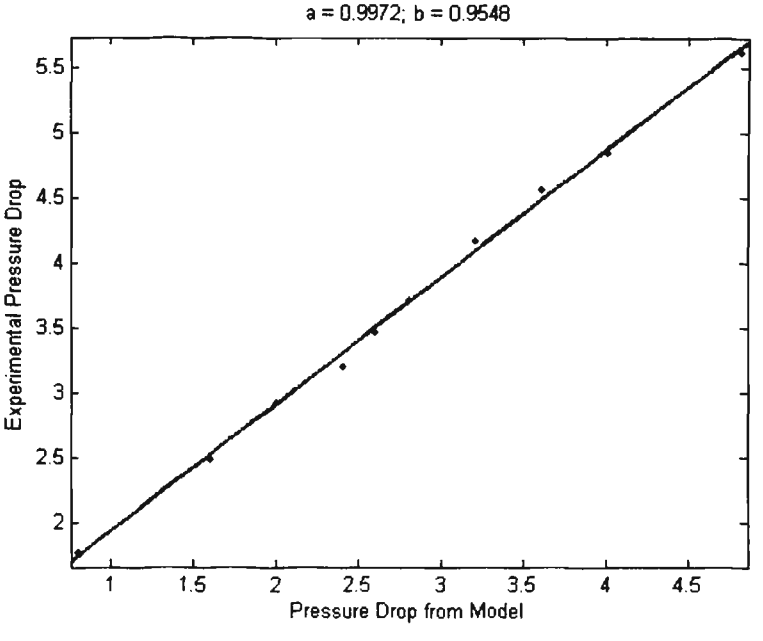

Figure A.16 Curve fitting plot of 78^0 contact angle channel using 12 mm bubble

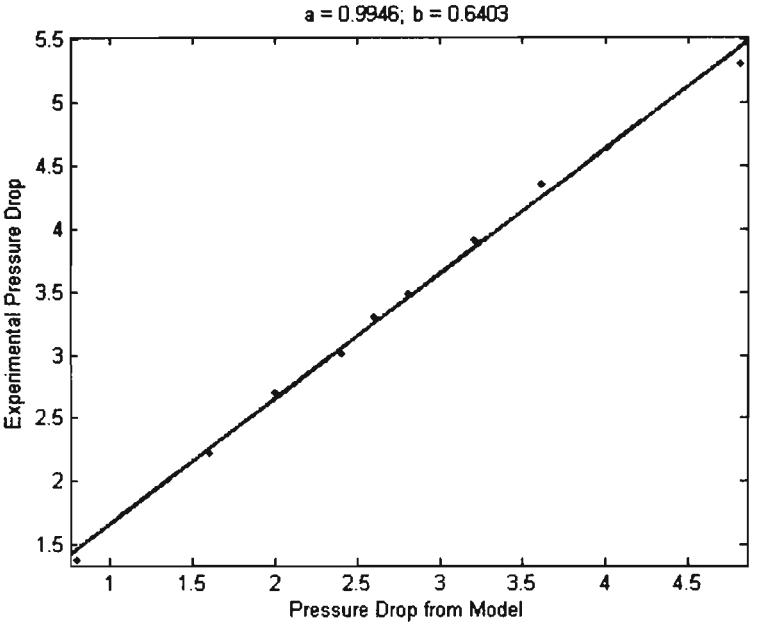

Figure A.17 Curve fitting plot of 63^0 contact angle channel using 12 mm bubble

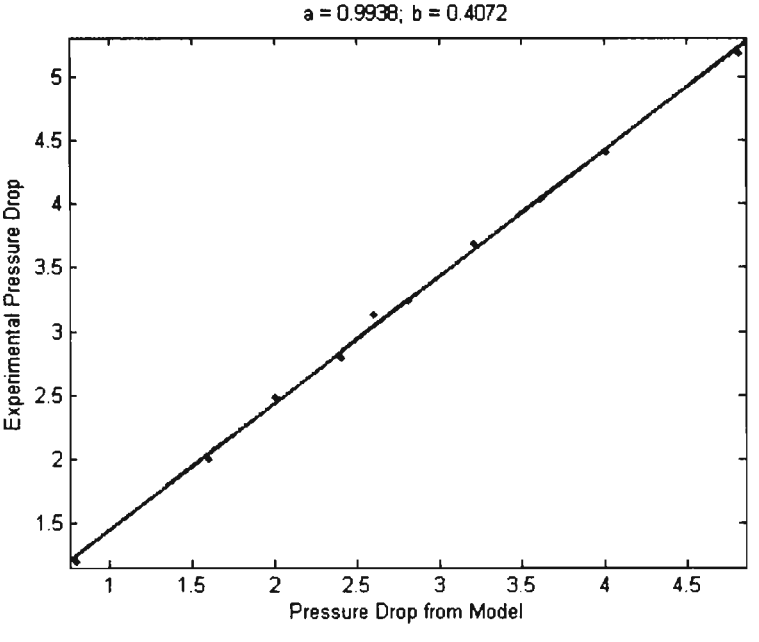

Figure A.18 Curve fitting plot of 51^0 contact angle channel using 12 mm bubble

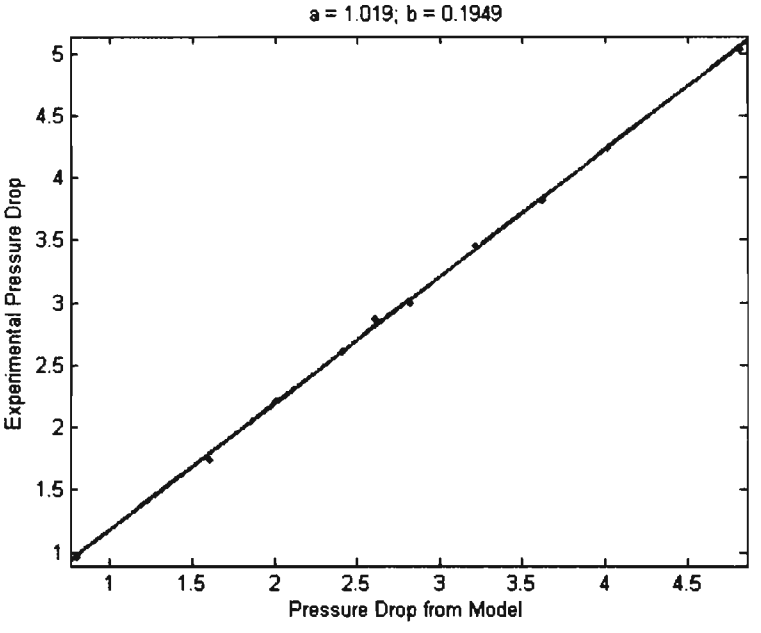

Figure A.19 Curve fitting plot of 35^0 contact angle channel using 12 mm bubble

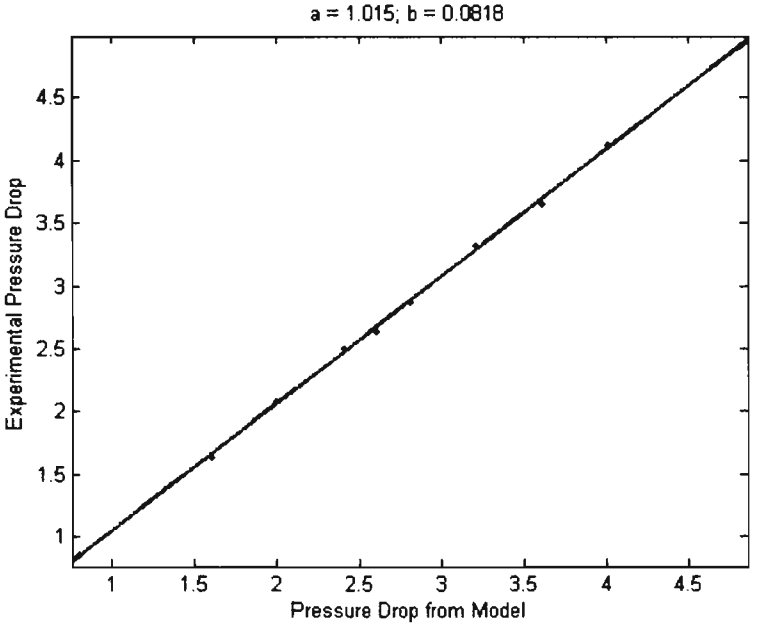

Figure A.20 Curve fitting plot of 24^0 contact angle channel using 12 mm bubble

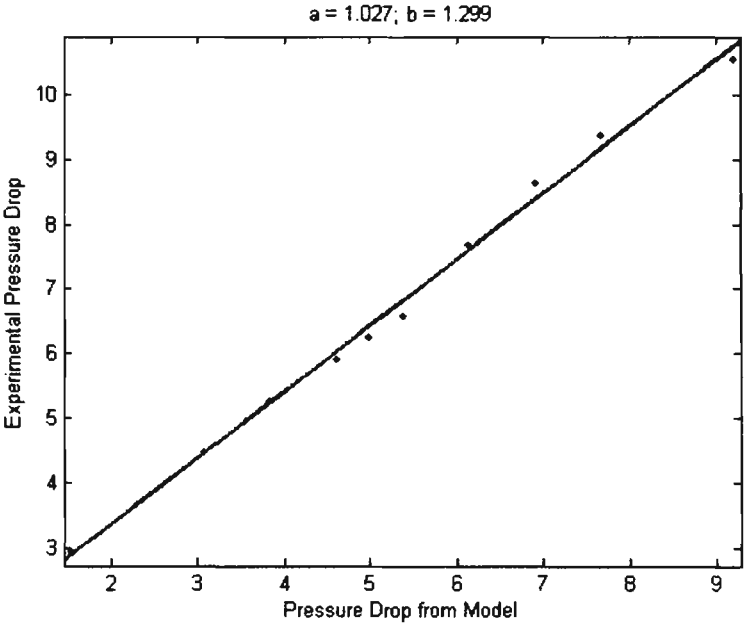

Figure A.21 Curve fitting plot of 78^0 contact angle channel using 15 mm bubble

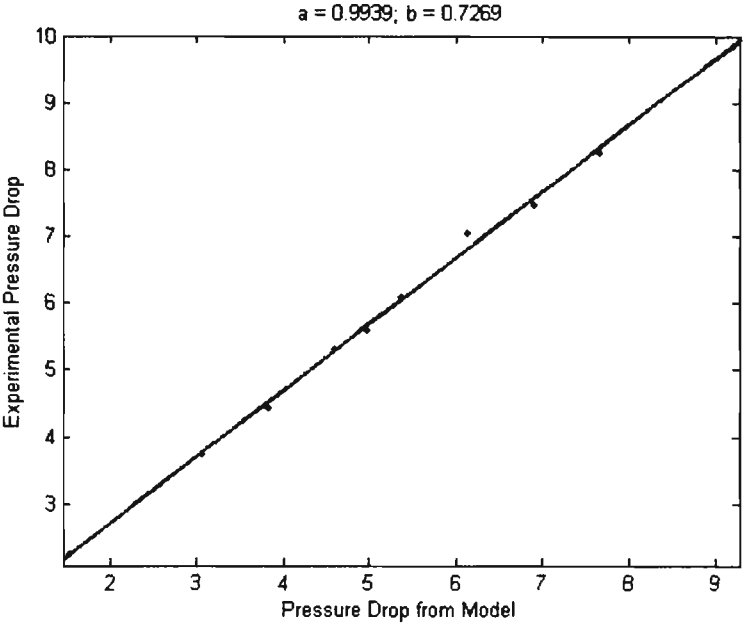

Figure A.22 Curve fitting plot of 63^0 contact angle channel using 15 mm bubble

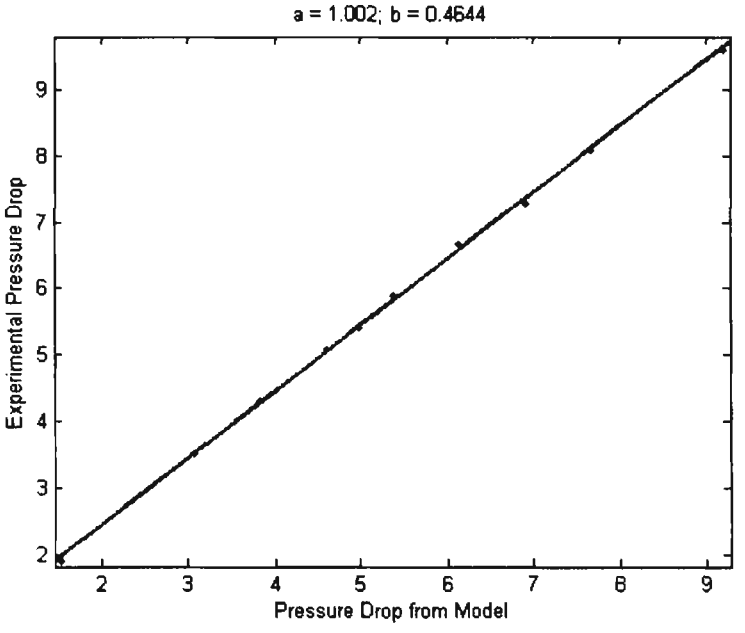

Figure A.23 Curve fitting plot of 51^0 contact angle channel using 15 mm bubble

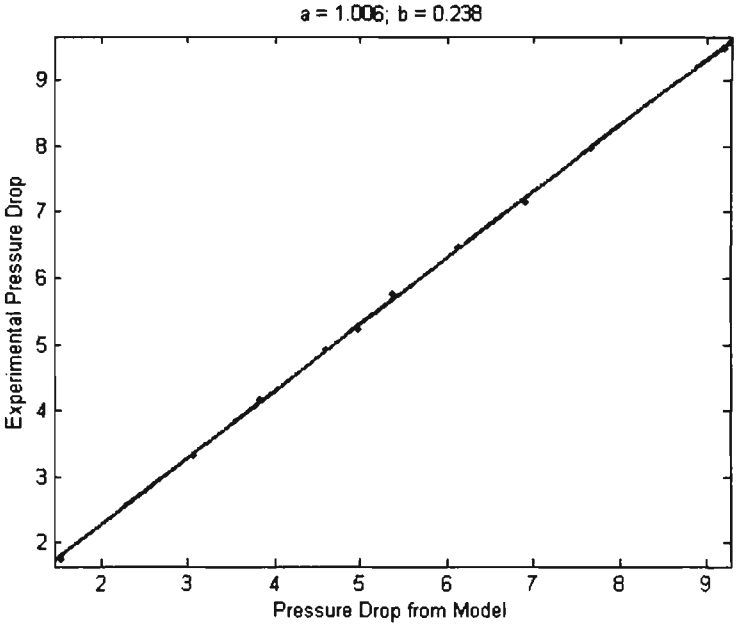

Figure A.24 Curve fitting plot of 35^0 contact angle channel using 15 mm bubble

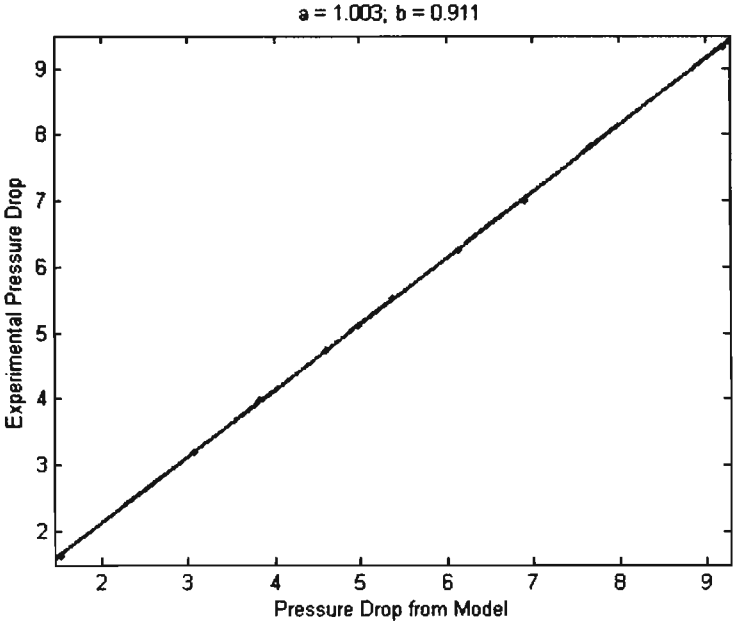

Figure A.25 Curve fitting plot of 24^0 contact angle channel using 15 mm bubble

The curve fitting plots obtains from Equation 16 are show in Figures A.26-A.35.

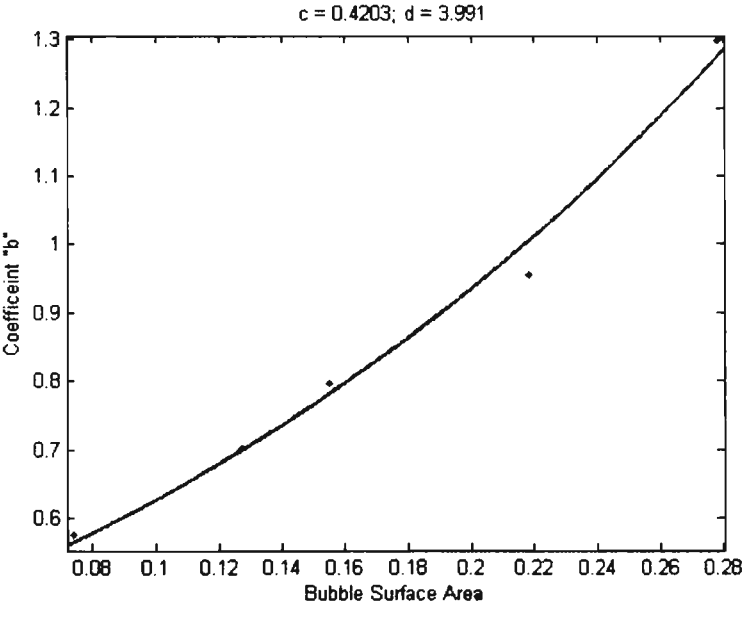

Figure A.26 Curve fitting plot of coefficient 'b' of 78^0 contact angle channel against the bubble contact area

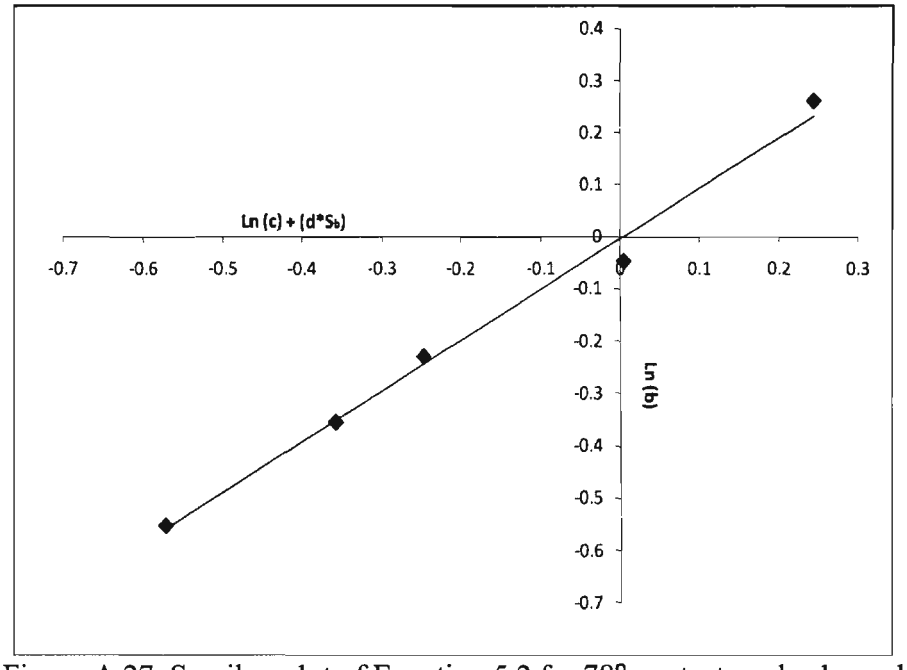

Figure A.27 Semilog plot of Equation 5.2 for 78° contact angle channel

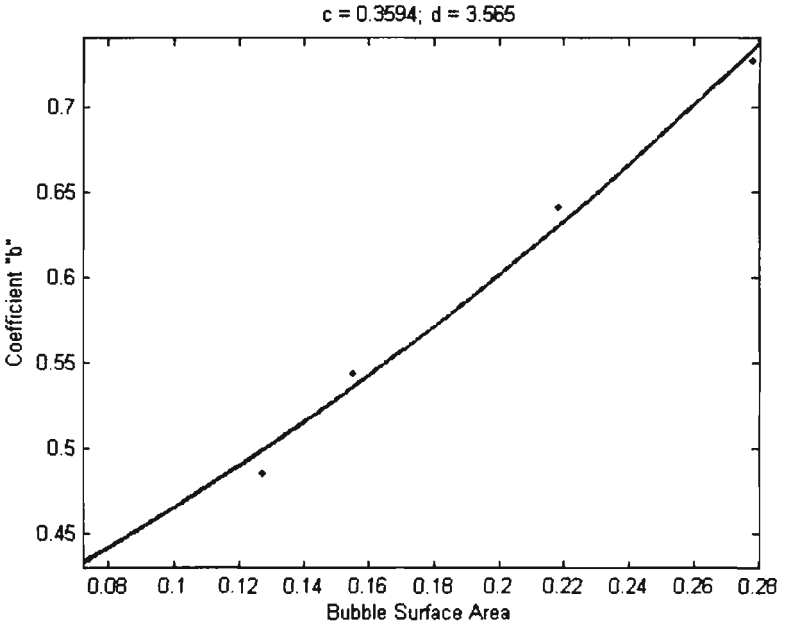

Figure A.28 Curve fitting plot of coefficient 'b' of 63° contact angle channel against the bubble contact area

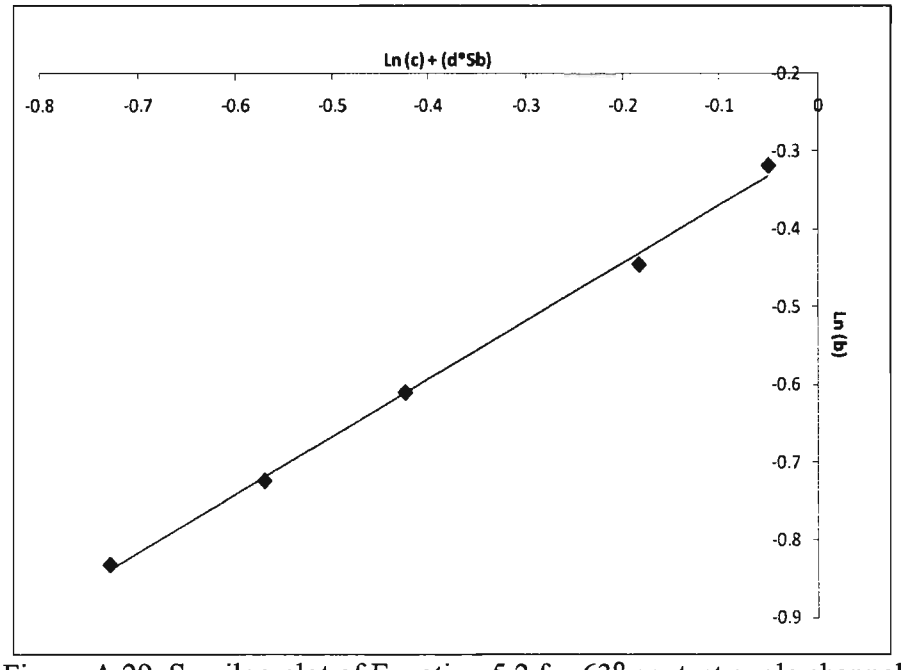

Figure A.29 Semilog plot of Equation 5.2 for 63° contact angle channel

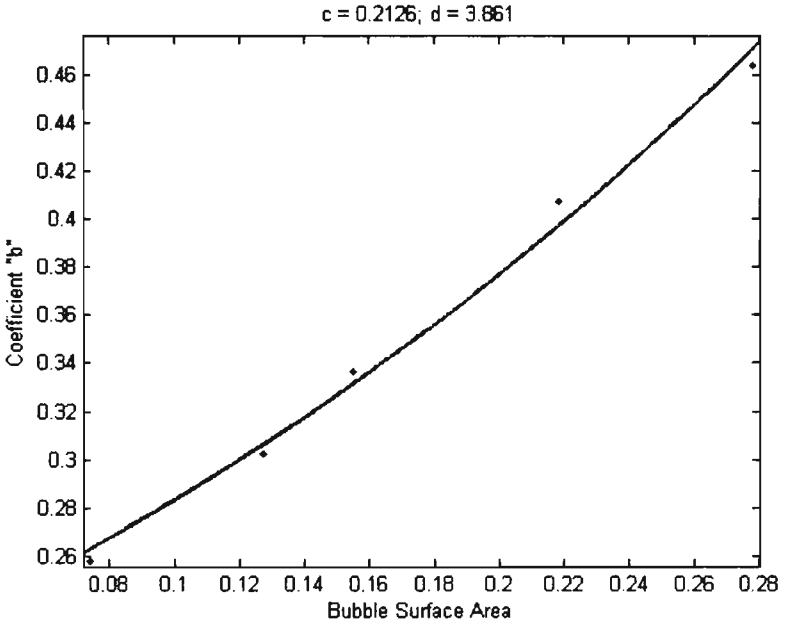

Figure A.30 Curve fitting plot of coefficient 'b' of 51^0 contact angle channel against the bubble contact area

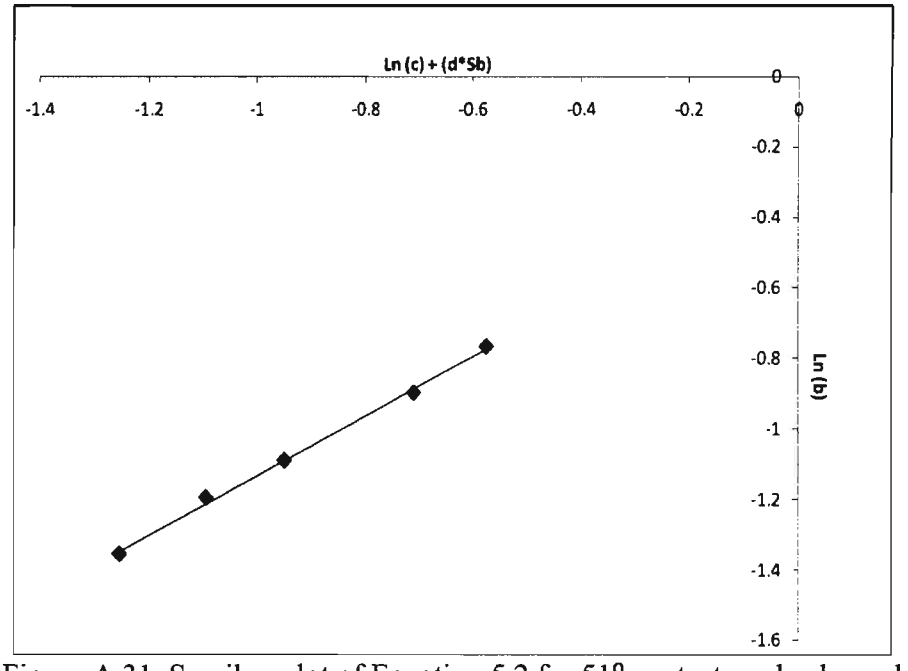

Figure A.31 Semilog plot of Equation 5.2 for 51° contact angle channel

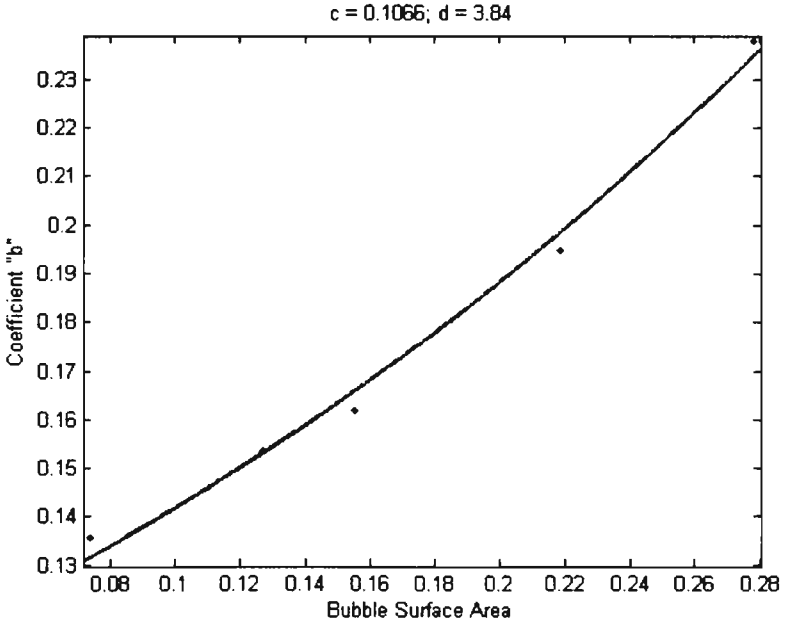

Figure A.32 Curve fitting plot of coefficient 'b' of 35° contact angle channel against the bubble contact area

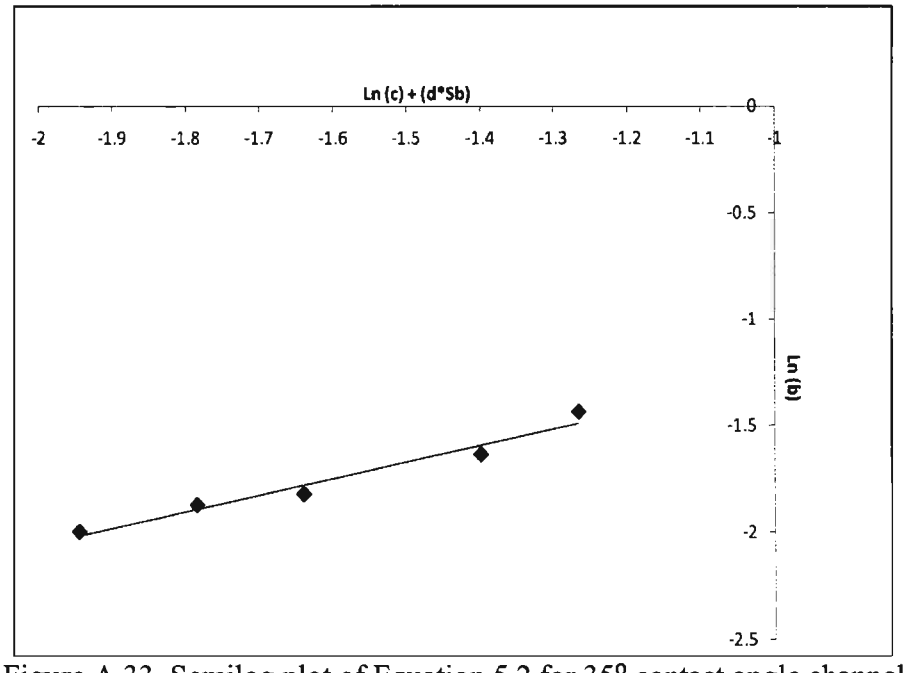

Figure A.33 Semilog plot of Equation 5.2 for 35^{o} contact angle channel

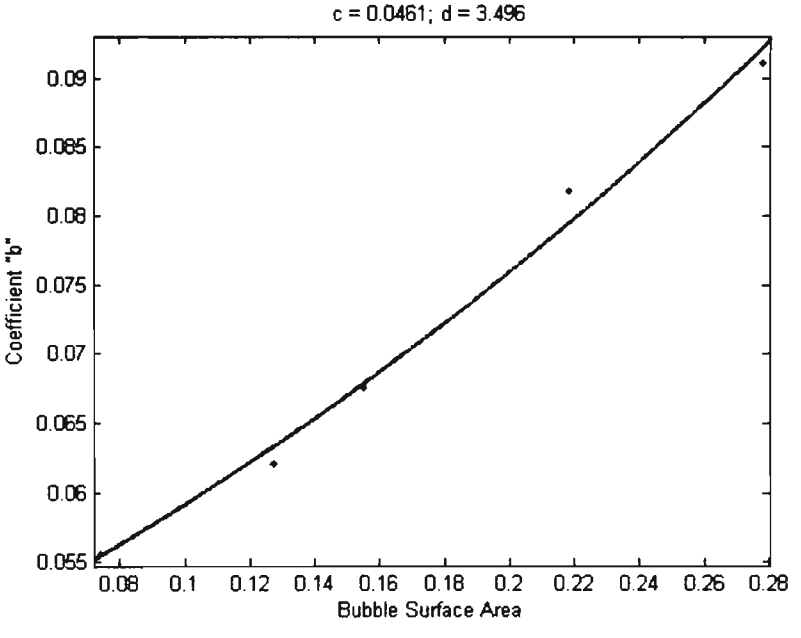

Figure A.34 Curve fitting plot of coefficient 'b' of 24^{0} contact angle channel against the bubble contact area

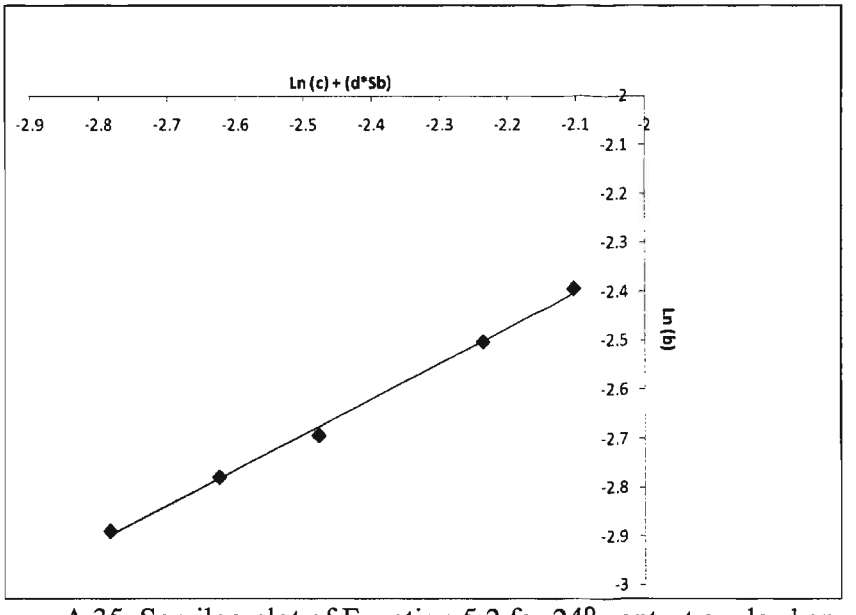

Figure A.35 Semilog plot of Equation 5.2 for 24° contact angle channel

Figure A.36 shows coefficient 'c' curve fitted against contact angle in radians using Equation 17

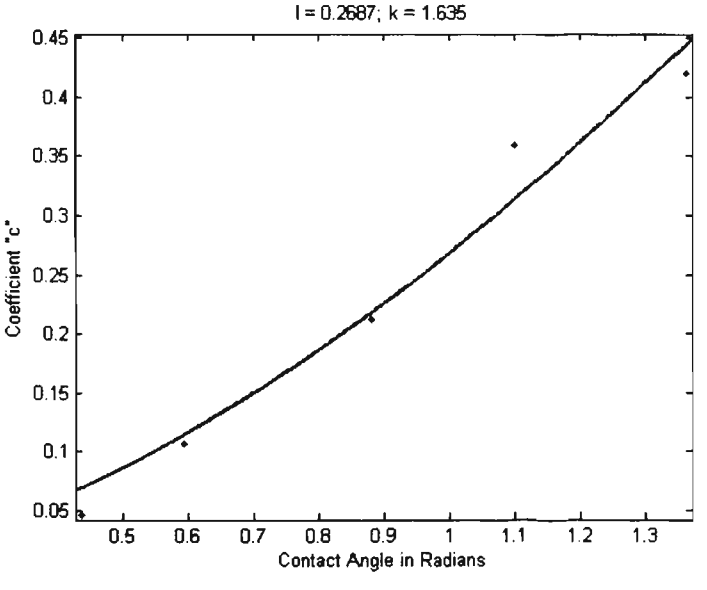

Figure A.36 Curve fitting plot of coefficient 'c' against contact angle in radians

APPENDIX B

PLOTS COMPARING THEORETICAL MODEL, PROPOSED MODEL, AND EXPERIMENTAL DATA

The plots B.1-B.5 show the comparison between the theoretical model, proposed model, and experimental data in smooth SU-8 channels of aspect ratios 2.

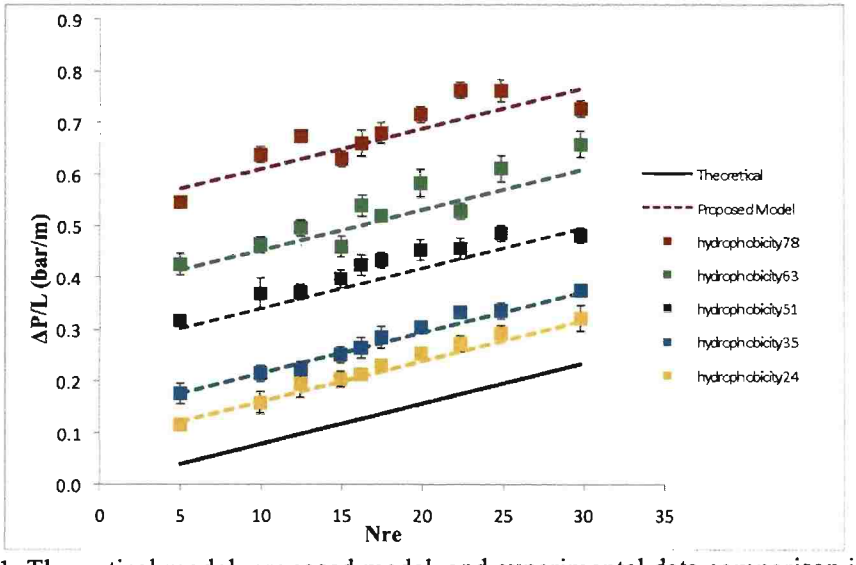

Figure B.1 Theoretical model, proposed model, and experimental data comparison in smooth SU-8 channels using 5 mm bubble

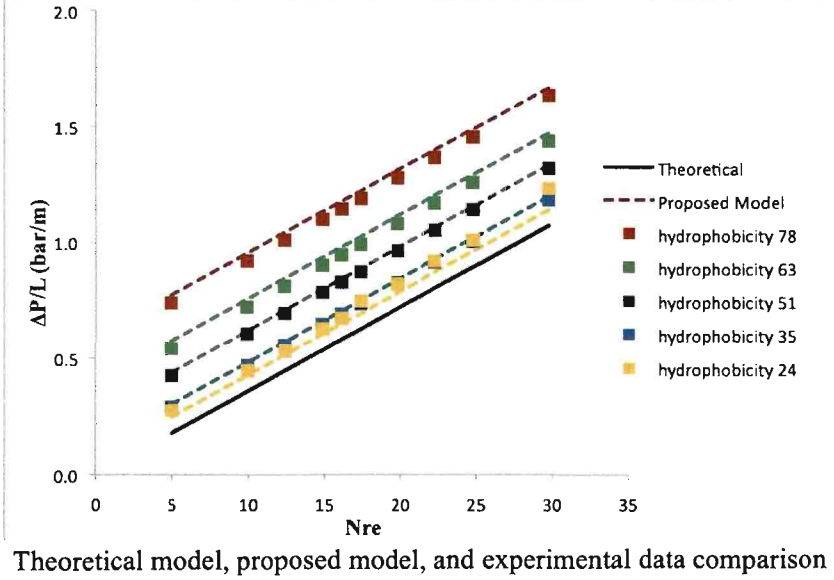

Figure B.2 Theoretical model, proposed model, and experimental data comparison in smooth SU-8 channels using 8 mm bubble

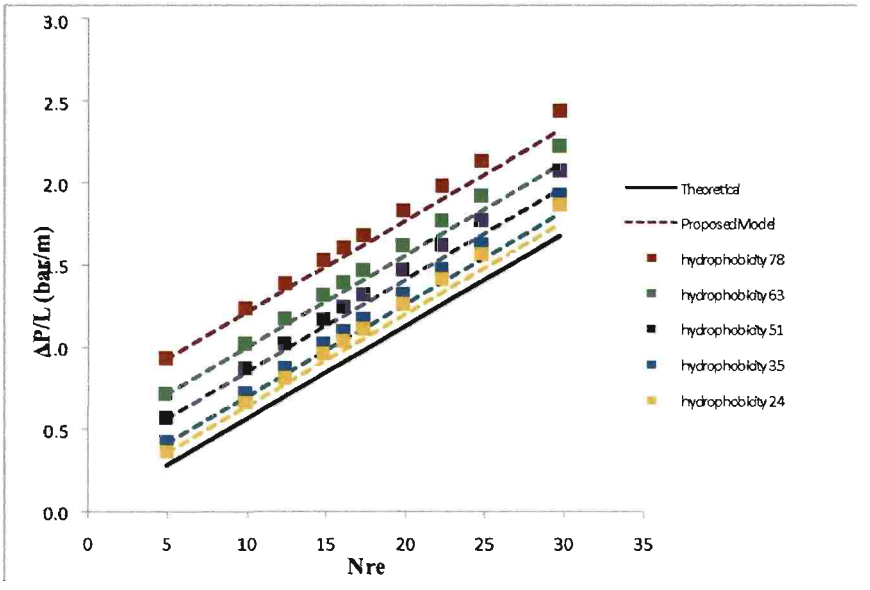

Figure B.3 Theoretical model, proposed model, and experimental data comparison in smooth SU-8 channels using 10 mm bubble

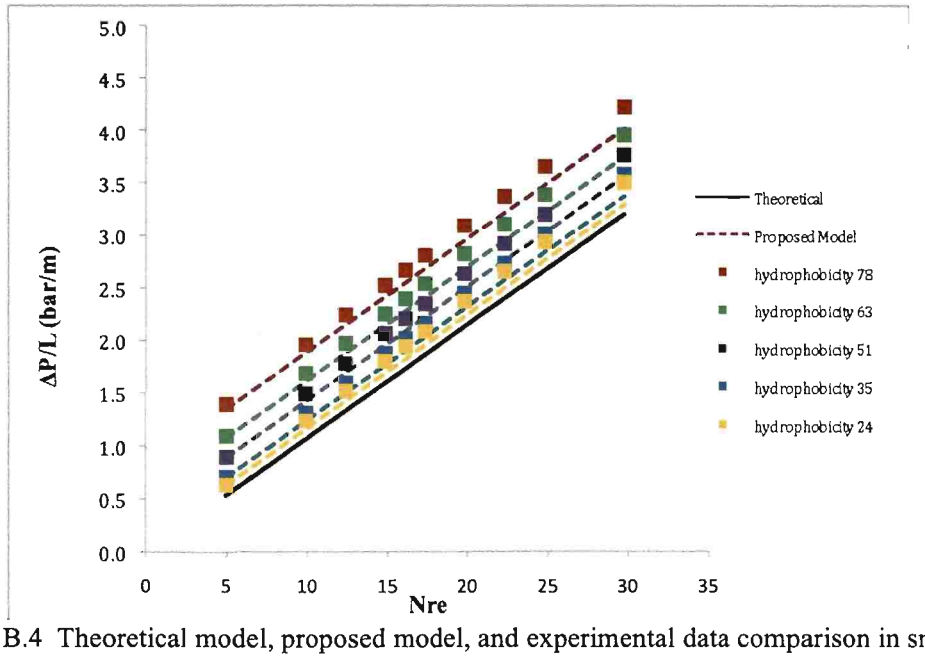

Figure B.4 Theoretical model, proposed model, and experimental data comparison in smooth SU-8 channels using 12 mm bubble

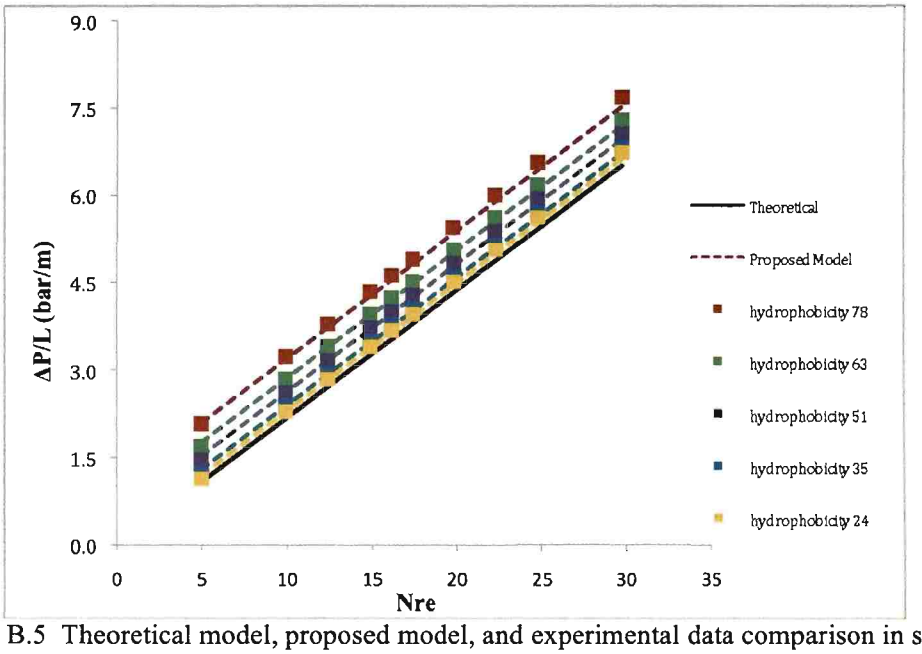

Figure B.5 Theoretical model, proposed model, and experimental data comparison in smooth SU-8 channels using 15 mm bubble

The plots B.6-B.10 show the comparison between the theoretical model, proposed model, and experimental data in smooth SU-8 channels of aspect ratios 4.

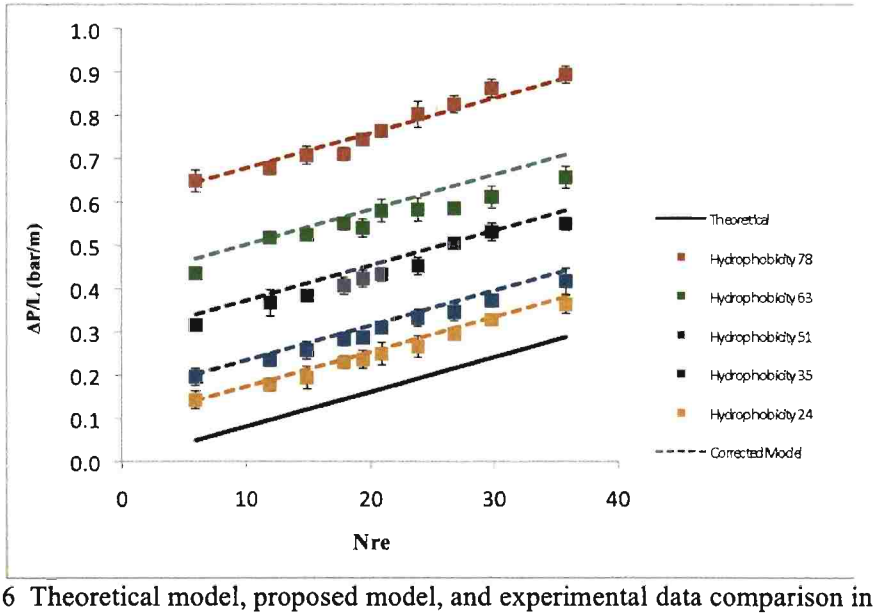

Figure B.6 Theoretical model, proposed model, and experimental data comparison in smooth SU-8 channels using 5 mm bubble

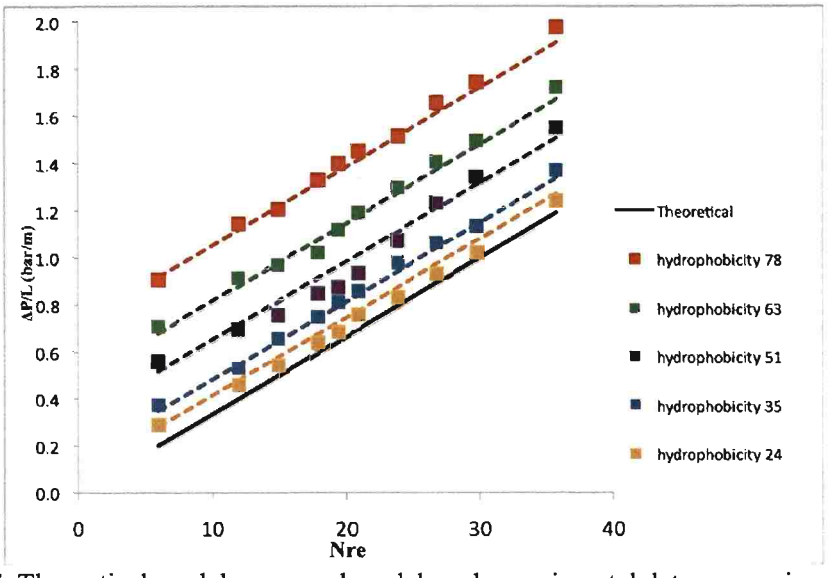

Figure B.7 Theoretical model, proposed model, and experimental data comparison in smooth SU-8 channels using 8 mm bubble

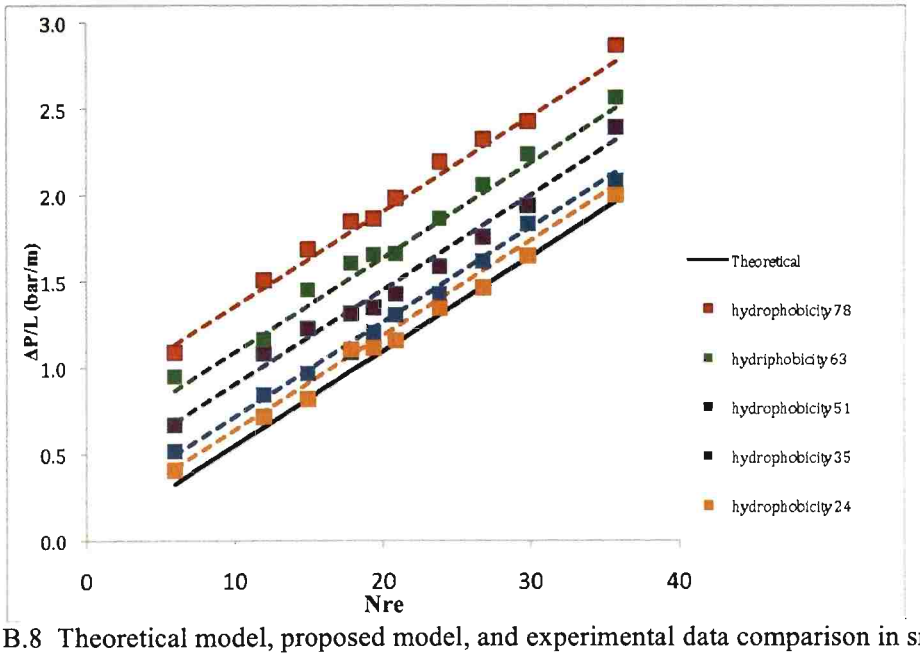

Figure B.8 Theoretical model, proposed model, and experimental data comparison in smooth SU-8 channels using 10 mm bubble

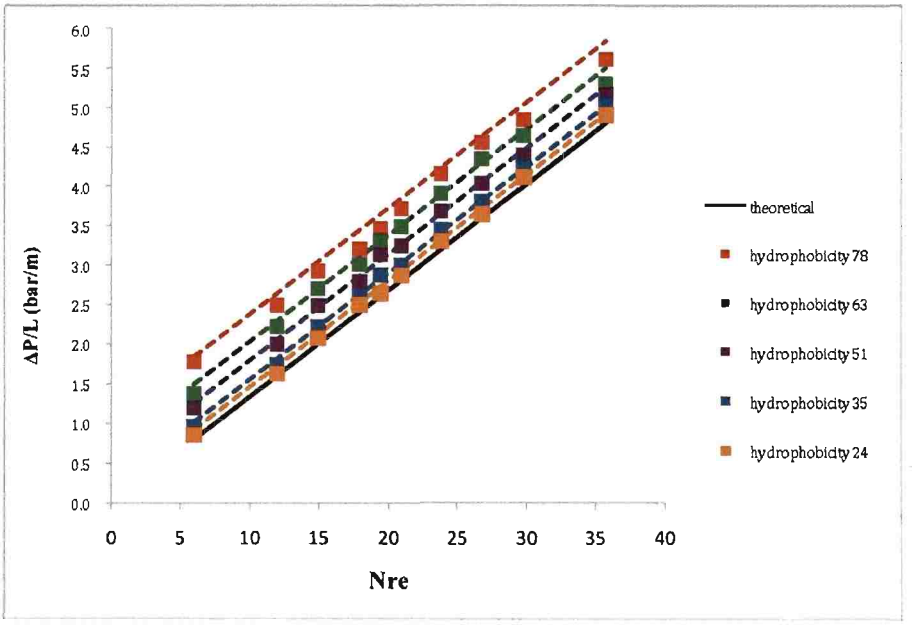

Figure B.9 Theoretical model, proposed model, and experimental data comparison in smooth SU-8 channels using 12 mm bubble

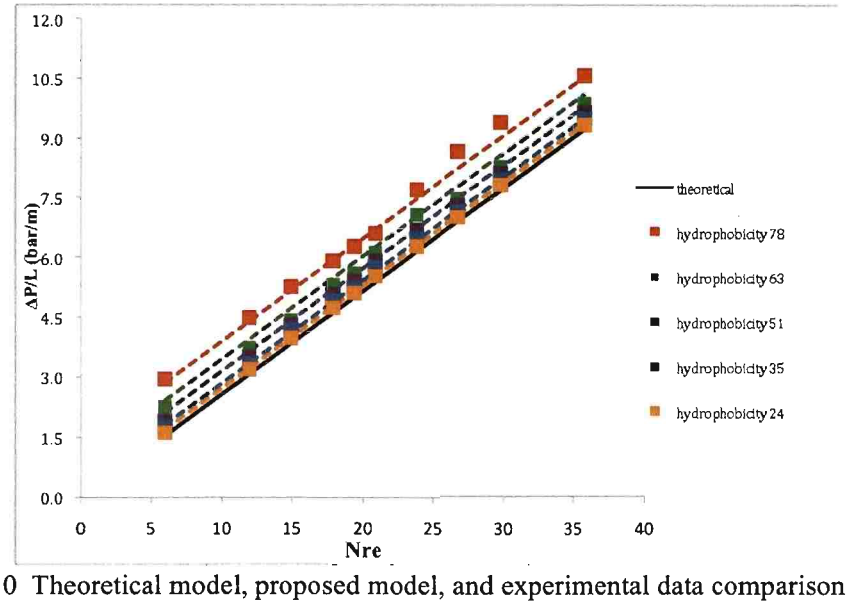

Figure B.10 Theoretical model, proposed model, and experimental data comparison in smooth SU-8 channels using 15 mm bubble

The plots B.11-B.15 show the comparison between the theoretical model, proposed model, and experimental data in smooth SU-8 channels of aspect ratios 6.

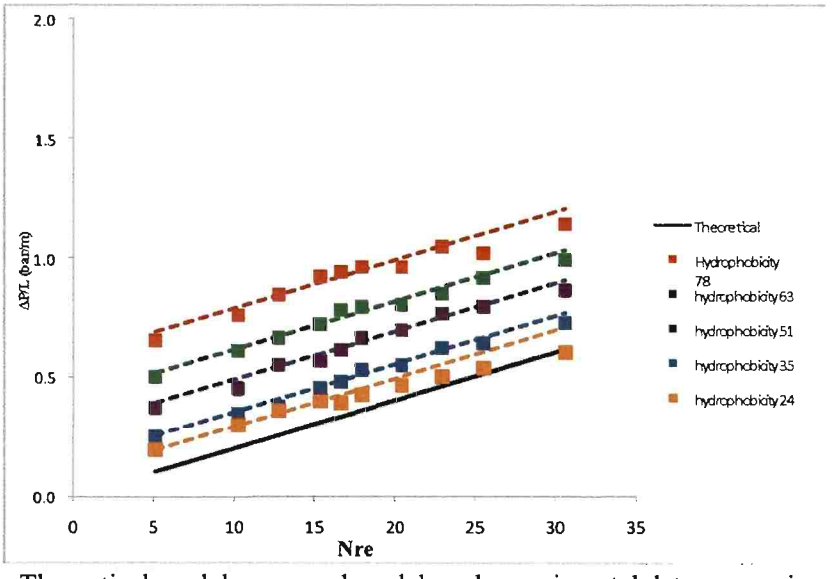

Figure B.11 Theoretical model, proposed model, and experimental data comparison in smooth SU-8 channels using 5 mm bubble

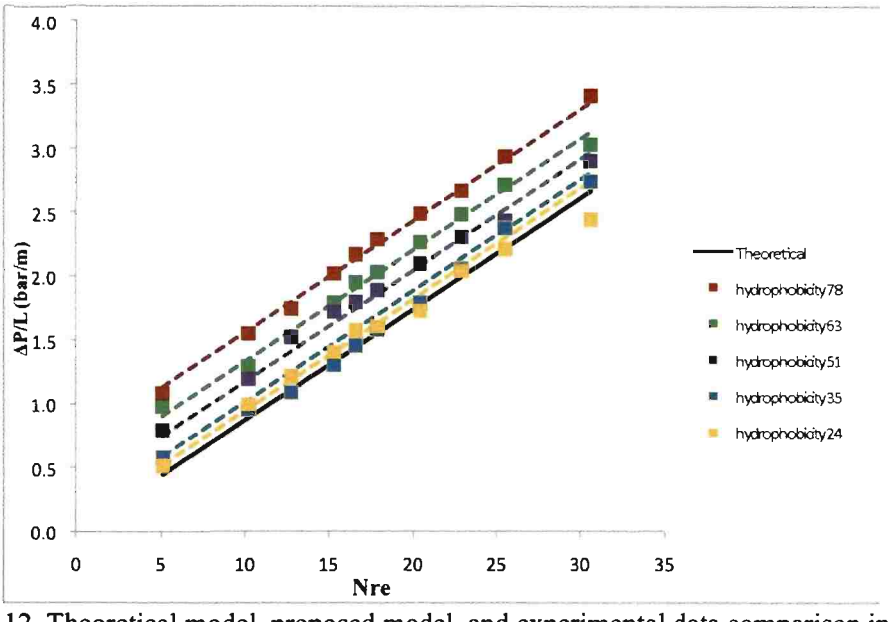

Figure B.12 Theoretical model, proposed model, and experimental data comparison in smooth SU-8 channels using 8 mm bubble

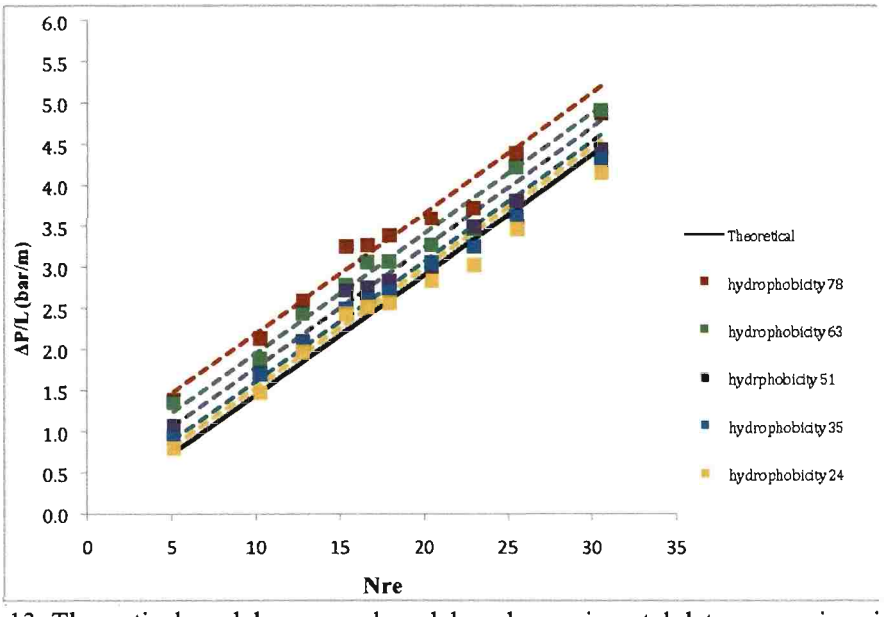

Figure B.13 Theoretical model, proposed model, and experimental data comparison in smooth SU-8 channels using 10 mm bubble

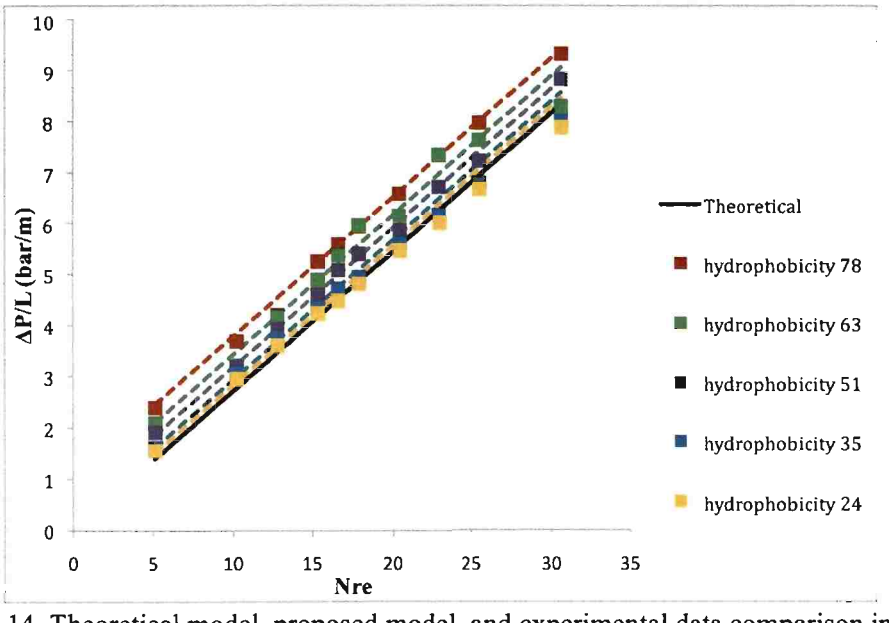

Figure B.14 Theoretical model, proposed model, and experimental data comparison in smooth SU-8 channels using 12 mm bubble

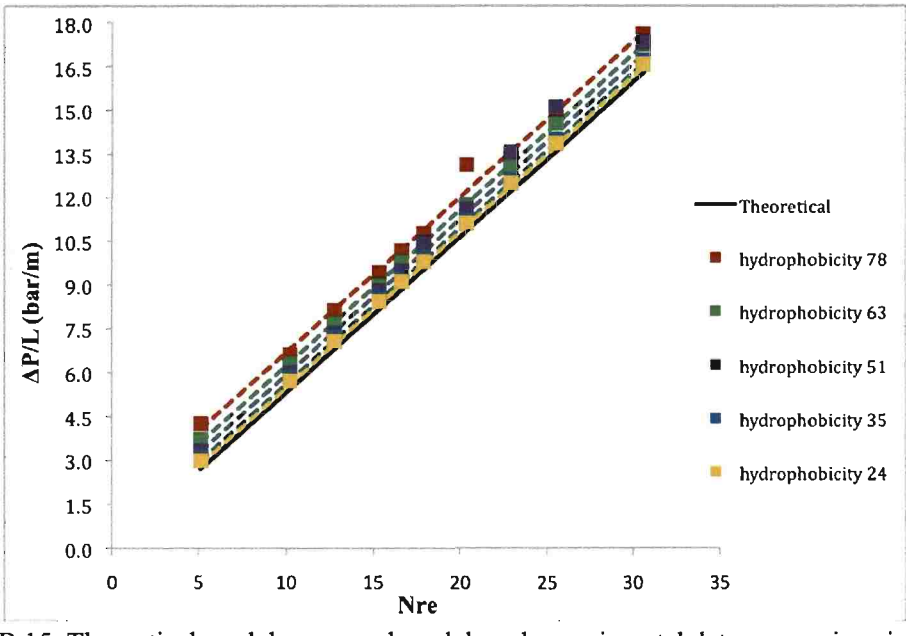

Figure B.15 Theoretical model, proposed model, and experimental data comparison in smooth SU-8 channels using 15 mm bubble

The plots B.16-B.20 show the comparison between the theoretical model, proposed model, and experimental data in smooth SU-8 channels of aspect ratio 10.

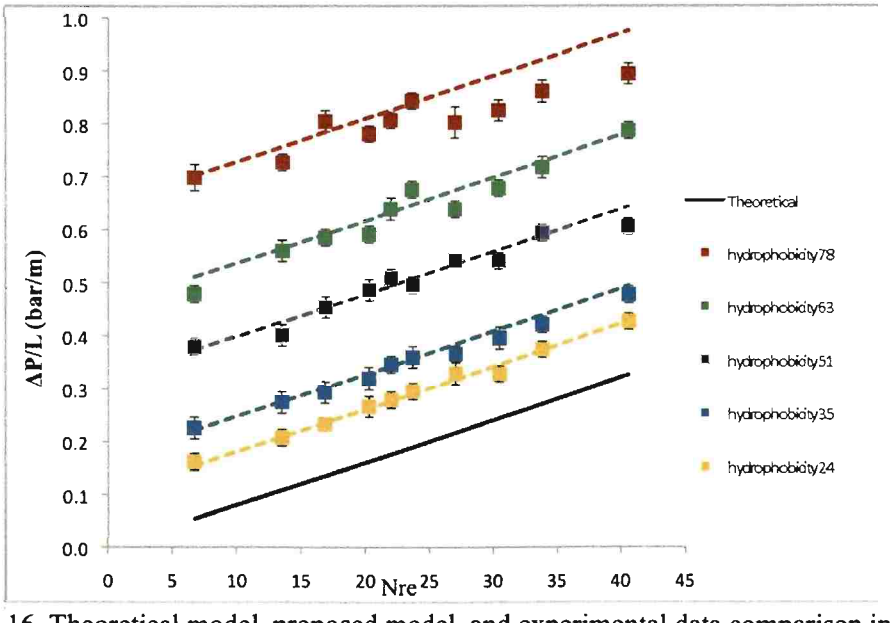

Figure B.16 Theoretical model, proposed model, and experimental data comparison in smooth SU-8 channels using 5 mm bubble

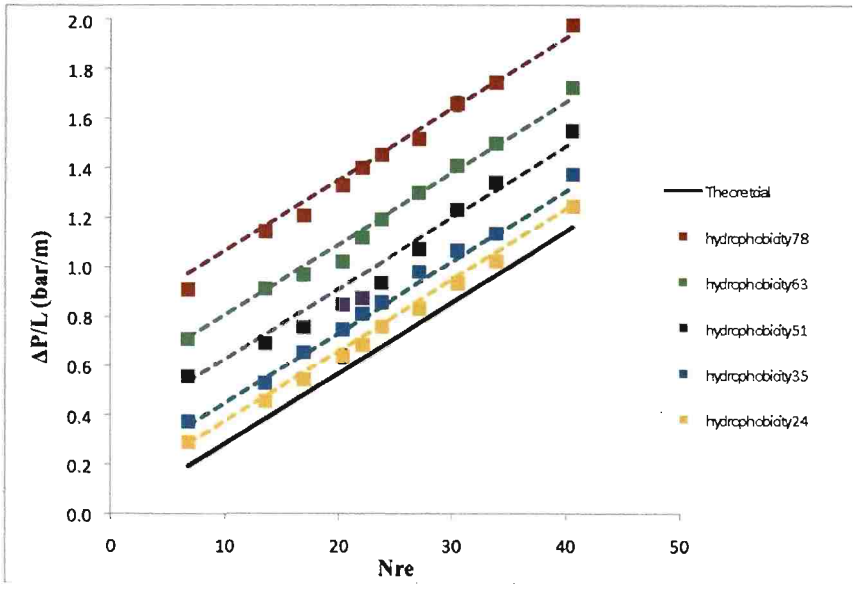

Figure B.17 Theoretical model, proposed model, and experimental data comparison in smooth SU-8 channels using 8 mm bubble

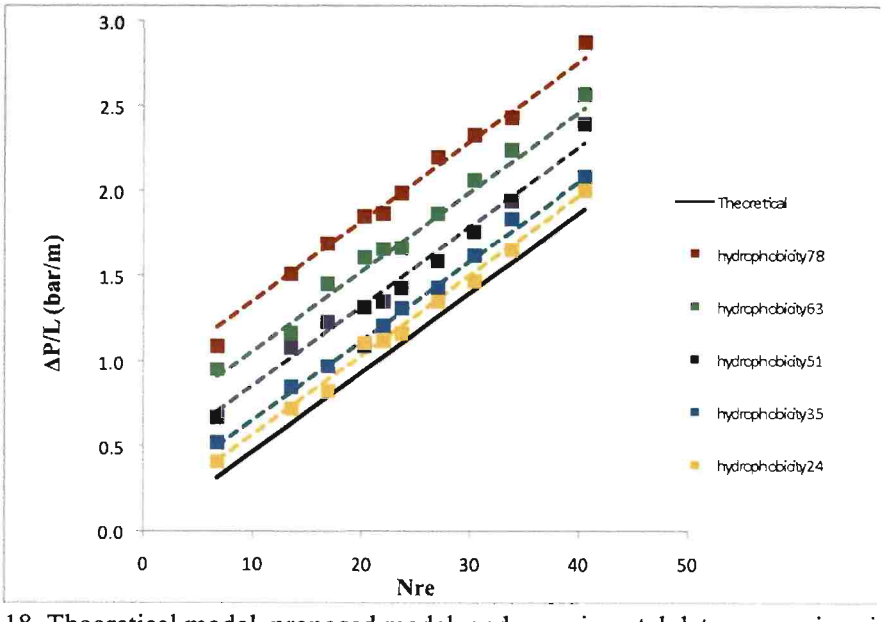

Figure B.18 Theoretical model, proposed model, and experimental data comparison in smooth SU-8 channels using 10 mm bubble

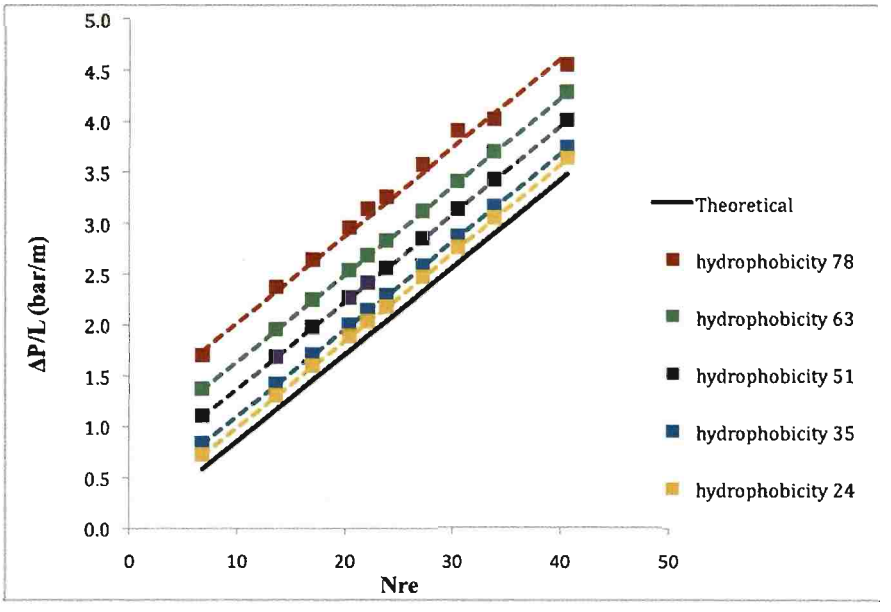

Figure B.19 Theoretical model, proposed model, and experimental data comparison in smooth SU-8 channels using 12 mm bubble

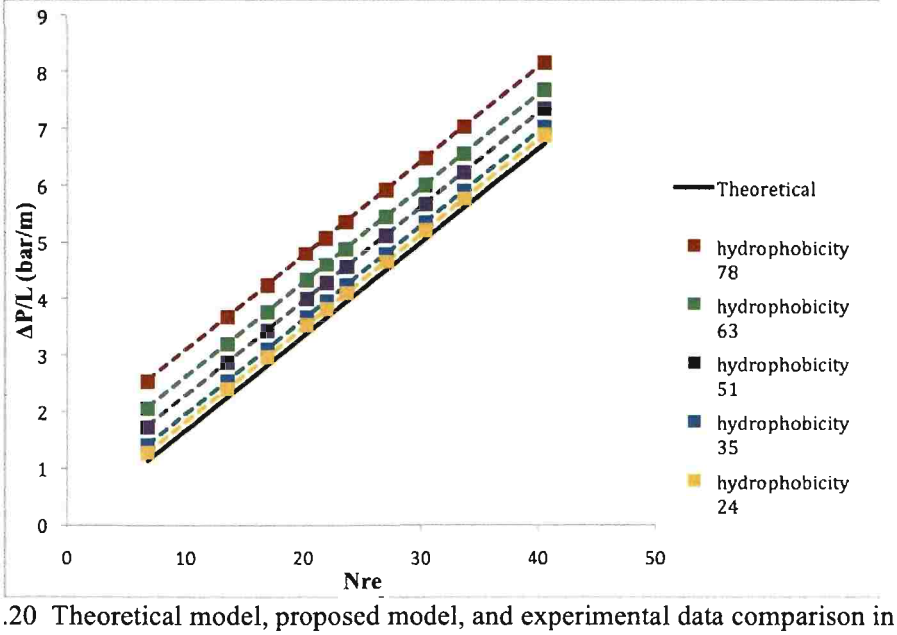

Figure B.20 Theoretical model, proposed model, and experimental data comparison in smooth SU-8 channels using 15 mm bubble

The plots B.21-B.25 show the comparison between the theoretical model, proposed model, and experimental data in smooth SU-8 channels of aspect ratio 16

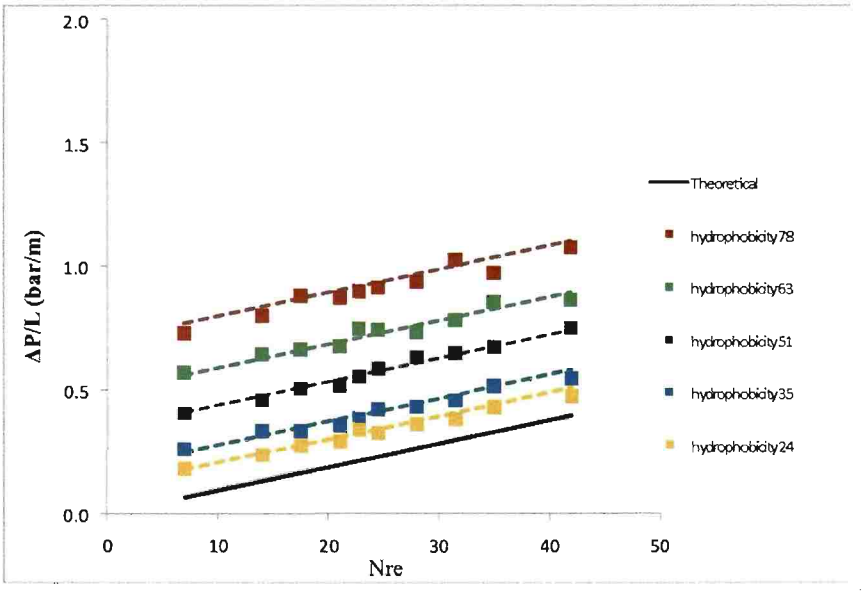

Figure B.21 Theoretical model, proposed model, and experimental data comparison in smooth SU-8 channels using 5 mm bubble

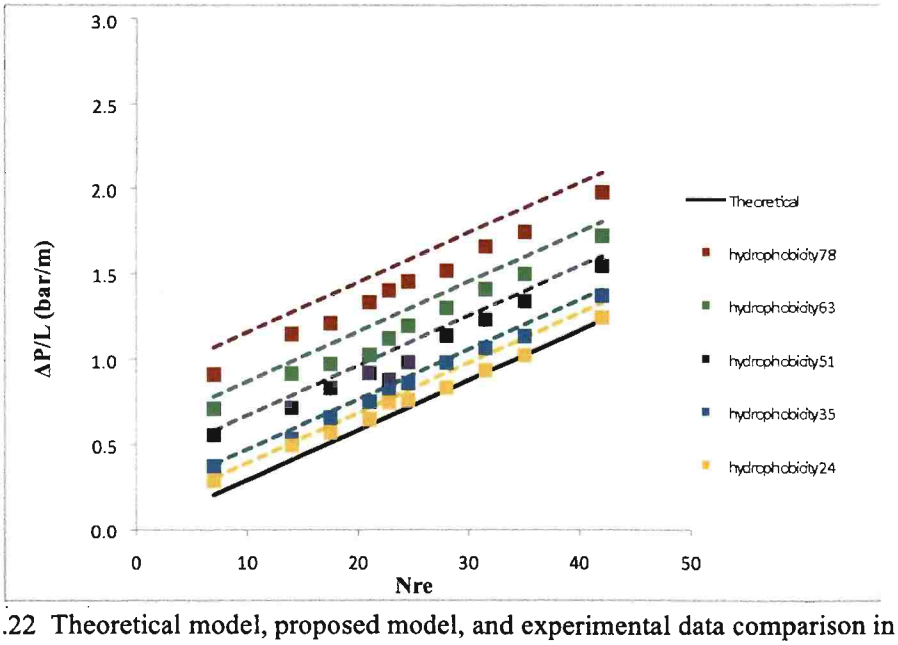

Figure B.22 Theoretical model, proposed model, and experimental data comparison in smooth SU-8 channels using 8 mm bubble

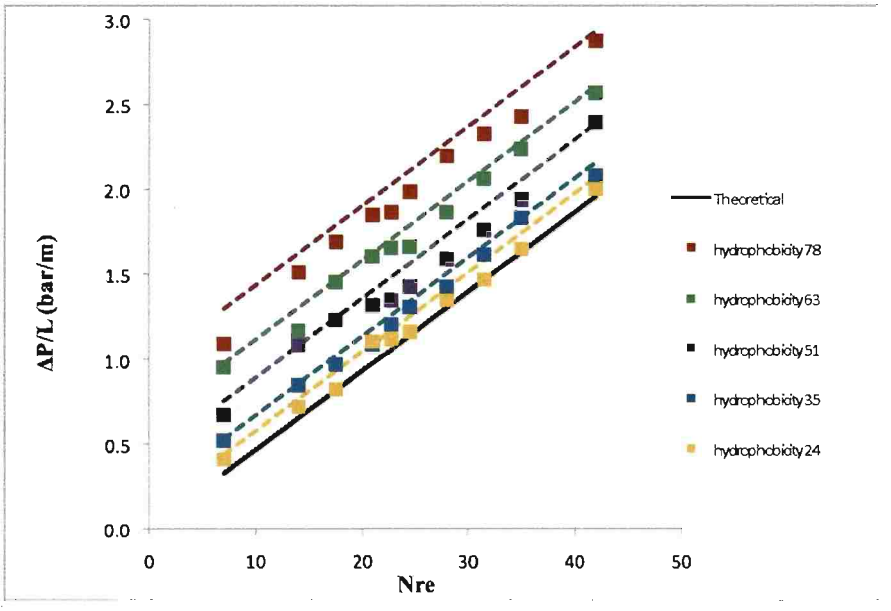

Figure B.23 Theoretical model, proposed model, and experimental data comparison in smooth SU-8 channels using 10 mm bubble

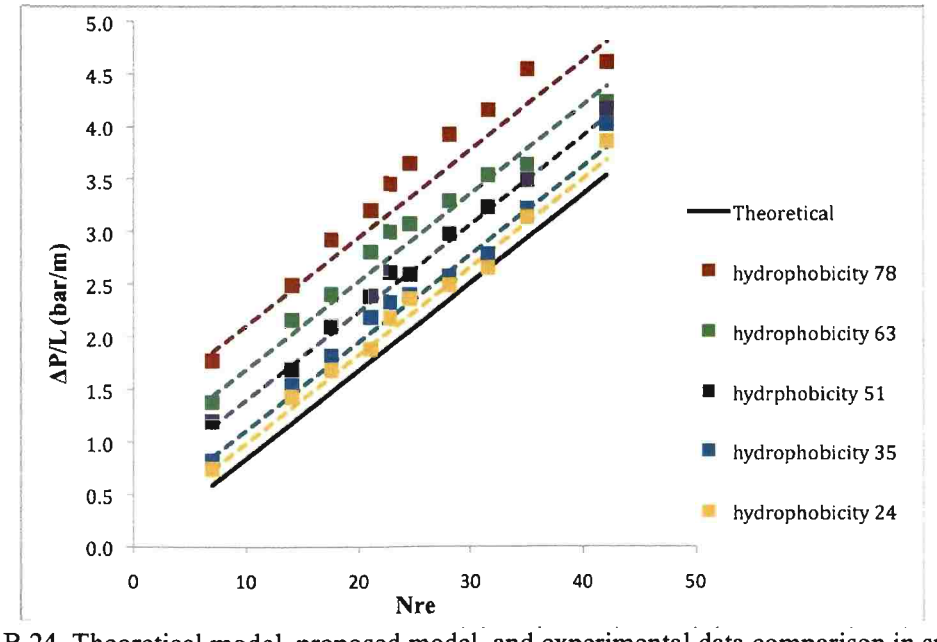

Figure B.24 Theoretical model, proposed model, and experimental data comparison in smooth SU-8 channels using 12 mm bubble

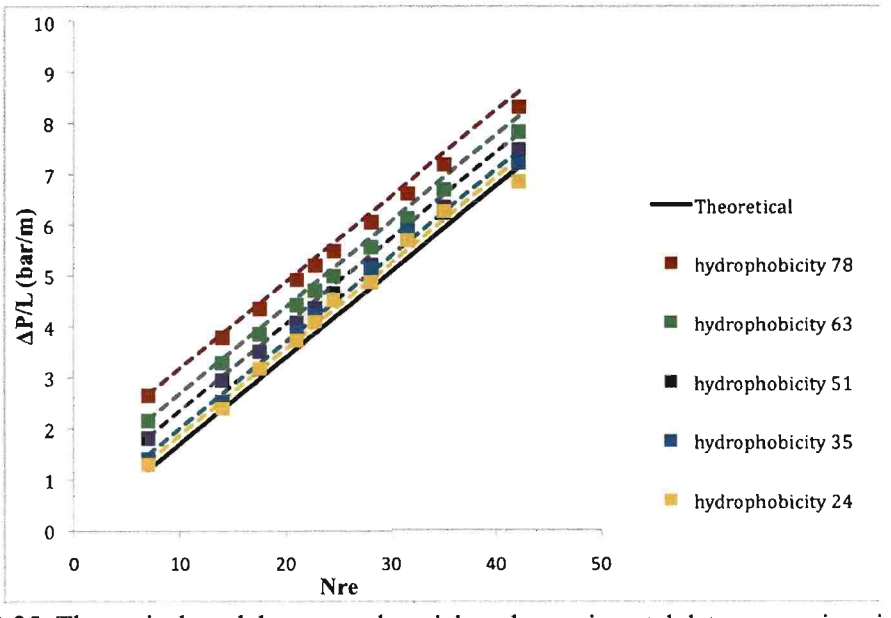

Figure B.25 Theoretical model, proposed model, and experimental data comparison in smooth SU-8 channels using 15 mm bubble

The plots B.26-B.30 show the comparison between the theoretical model, proposed model, and experimental data in smooth SU-8 channels of aspect ratio 20

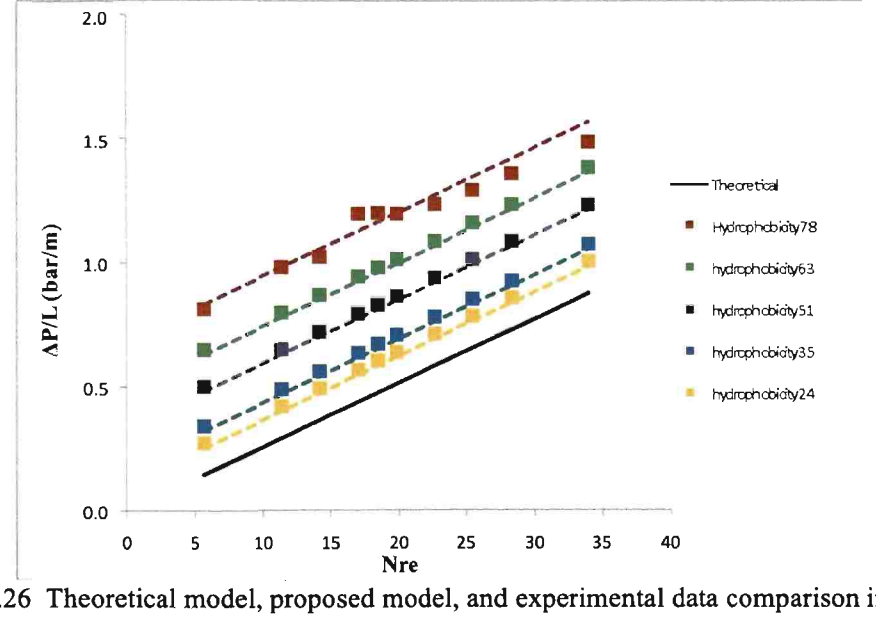

Figure B.26 Theoretical model, proposed model, and experimental data comparison in smooth SU-8 channels using 5 mm bubble

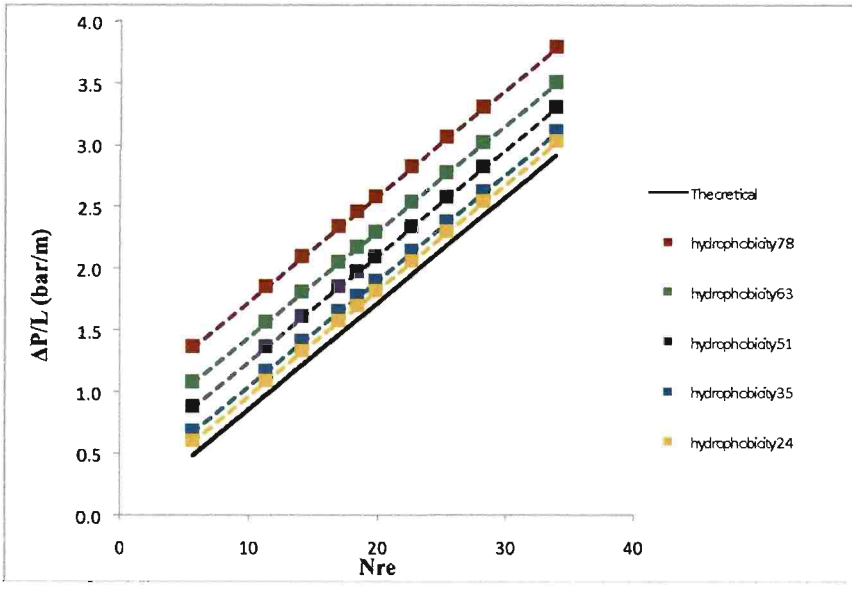

Figure B.27 Theoretical model, proposed model, and experimental data comparison in smooth SU-8 channels using 8 mm bubble

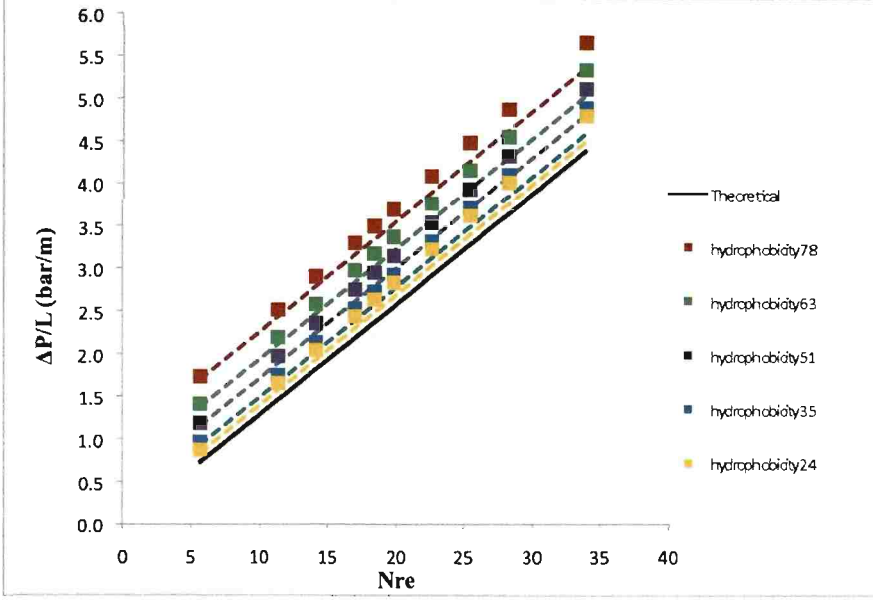

Figure B.28 Theoretical model, proposed model, and experimental data comparison in smooth SU-8 channels using 10 mm bubble

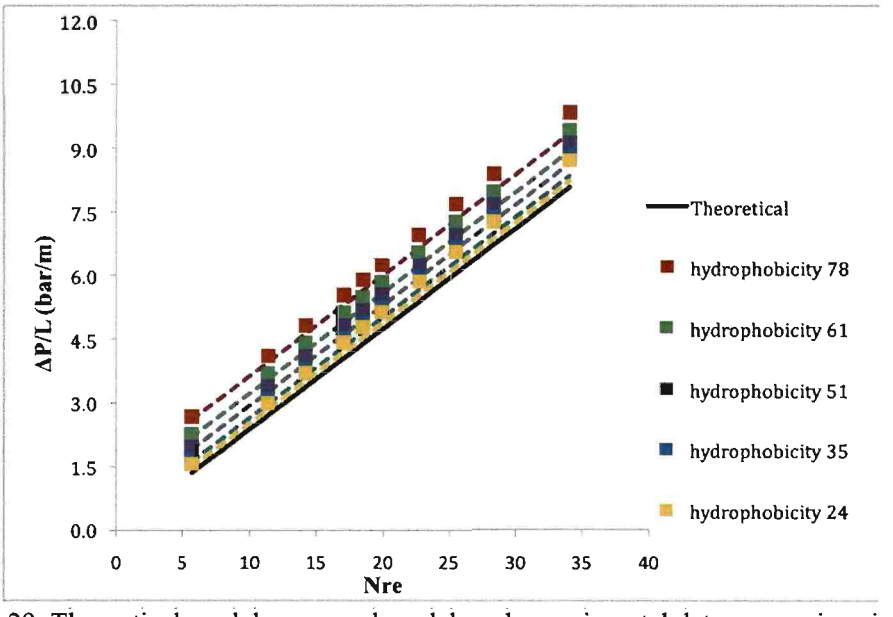

Figure B.29 Theoretical model, proposed model, and experimental data comparison in smooth SU-8 channels using 12 mm bubble

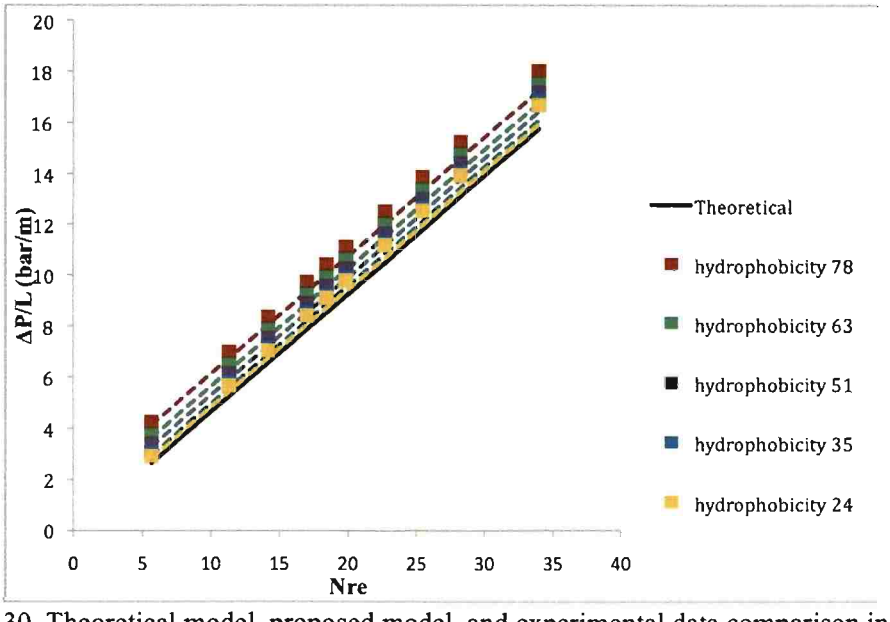

Figure B.30 Theoretical model, proposed model, and experimental data comparison in smooth SU-8 channels using 15 mm bubble

REFERENCES

1. S.Y. The, R. Lin, L.H. Hung and A.P. Lee (2008) "Droplet Microfluidics," Lab on a Chip, 8:198-220.

2. H. Song, D.L. Chen and R.F. Ismagilov (2006) "Reactions in Droplets in Microfluidic Channels," Angewandte Chemie International Edition, 45:7336-7356.

3. A. Kawahara, P.M.Y. Chang and M. Kawaji (2002) "Investigation of Two-Phase Flow Pattern, Void Fraction and Pressure Drop in a Microchannel," International Journal of Multiphase Flow, 28:1411-1435.

4. A. Gunther and K.F. Jensen (2006) "Multiphase Microfluidics: From Flow Characteristics to Chemical and Materials Synthesis," Lab on a Chip, 6:1487-1503.

5. F.P. Bretherton (1961) "The Motion of Long Bubbles in Tubes," Journal of Fluid Mechanics, 10:166-188.

6. B.P. Ho and L.G. Leal (1975) "The Creeping Motion of Liquid Drops Through a Circular Tube of Comparable Diameter," Journal of Fluid Mechanics, 71:361-383.

7. J. Ratulowski and H.C. Chang (1989) "Transport of Gas Bubbles in Capillaries," Physics of Fluids A, 1:1642-1655.

8. S.R. Hodges, O.E. Jensen and J.M. Rallison (2004) "The Motion of a Viscous Drop Through a Cylindrical Tube," Journal of Fluid Mechanics, 501:279-301.

9. A. Mazouchi and G.M. Homsy (2001) "Thermocapillary Migration of Long Bubbles in Polygonal Tube. I. Theory," Physics of Fluids, 13:1594-1600.

10. M.J. Fuerstman, A. Lai, M.E. Thurlow, S.S Shevkoplyas, H.A. Stone and G.M. Whitesides (2007) "The Pressure Drop Along Rectangular Microchannels Containing Bubbles," Lab on a Chip, 7:1479-1489.

11. T. Cubaud and C.M. Ho (2004) "Transport of Bubbles in Square Channels," Physics of Fluids, 16:4575-4584.

12. J. Koo and C. Kleinstreuer (2007) "Liquid Flow in Microchannel: Experimental Observation and Computational Analysis of Microfluidic Effects," Journal of Micromechanics and Microengineering, 13:568-579.

13. J. July, D. Mayes and B.D. Webb (2002) "Characterization of Frictional Pressure Drop for Liquid Flows Through Microchannels," International Journal of Heat and Mass Transfer, 45:3477-3489.

14. C.Y. Yang and R.L. Webb (1996) "Condensation of R-12 in Small Hydraulic Diameter Extruded Aluminum Tubes With and Without Micro-Fins," International Journal of Heat and Mass Transfer, 39:791-800.

15. C.Y. Yang and R.L. Webb (1996) "Friction Pressure Drop of R-12 in Small Hydraulic Daimeter Extruded Aluminum Tubes With and Without Micro-Fins," International Journal of Heat and Mass Transfer, 39:801-809.

16. T.M. Squires and S.R. Quake (2005) "Microfluidics: Fluid Physics at the Nanoliter Scale," Reviews of Modern Physics, 77:977–1026.

17. A.M. Barajas and R.L. Panton (1993) "The Effects of Contact Angle on Two-Phase Flow in Capillary Tubes," International Journal of Multiphase Flow, 19:337–346.

18. T. Cubaud, U. Ulmanella and C.M. Ho (2006) "Two-Phase Flow in Microchannels With Surface Modifications," Fluid Dynamics Research, 38:772–786.

19. C.Y. Lee and S.Y. Lee (2007) "Influence of Interfacial Tensions on Transition of Two-Phase Flow Pattern in Mini-Channels," 6th International Conference Multiphase Flow (Lipzig, Germany).

20. J.C. Allen and S.Y. Son (2007) "High Speed Microscopic Visualization of Adiabatic Gas–Liquid Flow in Microchannels," 18th International Symposium on Transport Phenomena, 2037–2042.

21. Z. Gao, D.B. Henthorn and C-S. Kim (2008) "Enhanced Wettability of an SU-8 Photoresist Through a Photografting Procedure for Analytical Device Applications," Journal of Micromechanics and Microengineering, 18:045013.

22. S. M. Ghiaasiaan and S. I. Abdel-Khalik (2001) "Two-Phase Flow in Microchannels. Advances in Heat Transfer," Academic Press, 34:145-244.

23. M. Suo and P. Griffith (1964) "Two-Phase Flow in Capillary Tubes," Journal of Basic Engineering, 86:576-582.

24. D. Barnea, Y. Luninski and Y. Taitel (1983) "Flow Pattern in Horizontal and Vertical Two Phase Flow in Small Diameter Tubes," Canadian Journal of Chemical Engineering, 61:617-620.

25. C. A. Damianides and J. W. Westwater (1988) "Two-Phase Flow Patterns in a Compact Heat Exchanger and in Small Tubes," Second UK National Conference on Heat Transfer, Glasgow, Scotland, 2:1257-1268.

26. T. Fukano, A. Kariyasaki and M. Kagawa (1989) "Flow Patterns and Pressure Drop in Isothermal Gas-Liquid Concurrent Flow in a Horizontal Capillary Tube," Proceedings of the 1989 ANS National Heat Transfer Conference, Philadelphia, Pennsylvania, 153-161.

27. K. Mishima and T. Hibiki (1996) "Some Characteristics of Air-Water Two-Phase Flow in Small Diameter Vertical Tubes," International Journal of Multiphase Flow, 22:703 - 712.

28. K. Mishima, T. Hibiki and H. Nishihara (1997) "Visualization and Measurement of Two-Phase Flow by Using Neutron Radiography," Nuclear Engineering and Design, 175:25-35.

29. K. Mishima and T. Hibiki (1998) "Development of High-Frame-Rate Neutron Radiography and Quantitative Measurement Method for Multiphase Flow Research," Nuclear Engineering and Design, 184:183-201.

30. K. Mishima and M. Ishii (1984) "Flow Regime Transition Criteria for Upward Two-Phase Flow in Vertical Tubes," International Journal of Heat and Mass Transfer, 27:723-737.

31. J. W. Coleman and S. Garimella (1999) "Characterization of Two-Phase Flow Patterns in Small Diameter Round and Rectangular Tubes," International Journal of Heat and Mass Transfer, 42(15):2869-2881.

32. K. A. Triplett, S. M. Ghiaasiaan, S. I. Abdel-Khalik and D. L. Sadowski (1999) "Gas-Liquid Two Phase Flow in Microchannels. Part 1: Two-Phase Flow Patterns," International Journal of Multiphase Flow, 25(3):377-394.

33. L. Galbiati and P. Andreini (1992) "Flow Pattern Transition for Vertical Downward Two-Phase Flow in Capillary Tubes. Inlet Mixing Effects," International Communications in Heat and Mass Transfer, 19(6):791-799.

34. H. Ide, H. Matsumura, Y. Tanaka and T. Fukano (1997) "Flow Patterns and Frictional Pressure Drop in Gas-Liquid Two-Phase Flow in Vertical Capillary Channels with Rectangular Cross Section," Nippon Kikai Gakkai Ronbunshu, B Hen/Transactions of the Japan Society of Mechanical Engineers, Part B, 63:452-460.

35. T. S. Zhao and Q. C. Bi (2001) "Co-Current Air-Water Two-Phase Flow Patterns in Vertical Triangular Microchannels," International Journal of Multiphase Flow, 27:765-782.

36. C.-Y. Yang and C.-C. Shieh (2001) "Flow Pattern of Air-Water and Two-Phase R-134a in Small Circular Tubes," International Journal of Multiphase Flow, 27(7):1163-1177.

37. A. Tabatabai and A. Faghri (2001) "A New Two-Phase Flow Map and Transition Boundary Accounting for Surface Tension Effects in Horizontal Miniature and Micro Tubes," Journal of Heat Transfer, 123(5):958-968.

38. M. W. Wambsganss, J. A. Jendrzejczyk and D. M. France (1991) "Two-Phase Flow Patterns and Transitions in a Small, Horizontal, Rectangular Channel," International Journal of Multiphase Flow, 17(3):327-342.

39. M. W. Wambsganss, J. A. Jendrzejczyk and D. M. France (1994) "Determination and Characteristics of the Transition to Two-Phase Slug Flow in Small Horizontal Channels," Journal of Fluids Engineering, Transactions of the ASME, 116(1):140-146.

40. Z. Feng and A. Serizawa (1999) "Visualization of Two-Phase Flow Patterns in an Ultra-Small Tube," Proceedings of the 18th Multiphase Flow Symposium of Japan, Suita, Osaka, Japan, 33-36.

41. P.M.Y Chung, and M. Kawaji (2004) "The Effect of Channel Diameter on Adiabatic Two-Phase Flow Characteristics in Microchannels," International Journal of Multiphase Flow, 30:735-761.

42. P.M.Y Chung, M. Kawaji, A. Kawahara and Y. Shibata (2004) "Two-Phase Flow through Square and Circular Microchannels-Effects of Channel Geometry," Journal of Fluids Engineering, 126(4):546-552.

43. A. Kawahara, M. Sadatomi, K. Okayama, M. Kawaji and P.M.Y. Chung (2005) "Effects of Channel Diameter and Liquid Properties on Void Fraction in Adiabatic Two-Phase Flow through Microchannels," Heat Transfer Engineering, 26:13-19.

44. A. Serizawa and Z. Feng (2004) "Two-Phase Fluid Flow: Heat Transfer and Fluid Flow in Microchannels", G. P. Celata. New York, NY, Begell House, 1:91-117.

45. A. Kawahara, P.M.Y. Chung and M. Kawaji (2002) "Investigation of Two-Phase Flow Pattern, Void Fraction and Pressure Drop in a Microchannel," International Journal of Multiphase Flow, 28:1411-1435.

46. R. W. Lockhart and R. C. Martinelli (1949) "Proposed Correlation of Data for Isothermal Two Phase, Two-Component Flow in Pipes," Chemical Engineering Progress, 45:39-45.

47. D. Chisholm (1973) "Pressure Gradients Due to Friction During the Flow of Evaporating Two-Phase Mixtures in Smooth Tubes and Channels," International Journal of Heat and Mass Transfer, 16:347-358.

48. L. Friedel (1979) "Improved Frictional Pressure Drop Correlations for Horizontal and Vertical Two Phase Pipe Flow," 3 R International, 18:485-491.

49. E. K. Ungar and J. D. Cornwell (1992) "Two-Phase Pressure Drop of Ammonia in Small Diameter Horizontal Tubes," AIAA paper, 92:3891.

50. M. Kuerta, T. Kobayashi, K. Mishima and H. Nishihara (1998) "Pressure Drop and Heat Transfer for Flow-Boiling of Water in Small-Diameter Tubes," JSME International Journal, Series B, 41:871-879.

51. K. A. Triplett, S. M. Ghiaasiaan, S. I. Abdel-Khalik, A. LeMouel and B. N. McCord (1999) "Gas Liquid Two-Phase Flow in Microchannels. Part 2: Void Fraction and Pressure Drop," International Journal of Multiphase Flow, 25(3):395-410.

52. C. Y. Yang and R. L. Webb (1996) "Friction Pressure Drop of R-12 in Small Hydraulic Diameter Extruded Aluminum Tubes with and without Micro-Fins," International Journal of Heat and Mass Transfer, 39:801-809.

53. Y.Y. Yan and T. F. Lin (1999) "Condensation Heat Transfer and Pressure Drop of Refrigerant R-134a in a Small Pipe," International Journal of Heat and Mass Transfer, 42:697-708.

54. D. Chisholm (1967) "A Theoretical Basis for the Lockhart-Martinelli Correlation for Two-Phase Flow," International Journal of Heat and Mass Transfer, 10:1767-1778.

55. C. C. Wang, C. S. Chiang and D. C. Lu (1997) "Visual Observation of Two-Phase Flow Pattern of R-22, R-134a, and R-407c in a 6.5-Mm Smooth Tube," Experimental Thermal and Fluid Science, 15:395-405.

56. I. Y. Chen, K. S. Yang, Y. J. Chang and C. C. Wang (2001) "Two-Phase Pressure Drop of Air-Water and R-410a in Small Horizontal Tubes," International Journal of Multiphase Flow, 27:1293-1299.

57. T. S. Zhao and Q. C. Bi (2001) "Pressure Drop Characteristics of Gas-Liquid Two-Phase Flow in Vertical Miniature Triangular Channels," International Journal of Heat and Mass Transfer, 44:2523-2534.

58. H. J. Lee and S. Y. Lee (2001) "Pressure Drop Correlations for Two-Phase Flow within Horizontal Rectangular Channels with Small Heights," International Journal of Multiphase flow, 27:783-796.

59. T. N. Tran, M. C. Chyu, M. W. Wambsganss and D. M. France (2000) "Two-Phase Pressure Drop of Refrigerants During Flow Boiling in Small Channels: An Experimental Investigation and Correlation Development," International Journal of Multiphase Flow, 26:1739-1754.

60. M. Zhang and R. L. Webb (2001) "Correlation of Two-Phase Friction for Refrigerants in Small-Diameter Tubes," Experimental Thermal and Fluid Science, 25:131-139.

61. A. E. Dukler and M. G. Hubbard (1975) "A Model for Gas-Liquid Slug Flow in Horizontal and Near Horizontal Tubes," Industrial Engineering and Chemical Fundamentals, 14:337-347.

62. T. Fukano, A. Kariyasaki and M. Kagawa (1989) "Flow Patterns and Pressure Drop in Isothermal Gas-Liquid Concurrent Flow in a Horizontal Capillary Tube," Proceedings of the 1989 ANS National Heat Transfer Conference, Philadelphia, Pennsylvania, 153-161.

63. M. J. Madou (2002) "Fundamentals of Microfabrication", 2nd Ed. Boca Raton, FL: CRC Press.

64. B. White, P. Fremstad, and F. Nogal (2008) "Ibm System z10 Enterprise Class Technical Introduction," IBM International Technical Support Organization.

65. "Intel Core i7 Processor Extreme Edition and Intel Core i7 Processor," Intel Corporation Datasheet, 1:2008.

66. M. J. Comstock, L. F. Thompson, C. G. Willson, and M. J. Bowden (1983) "Introduction to Microlithography," ser. 219. Washington, D.C: ACS Symposium Series.

67. SU-8 2000 Data Sheet Chart, MicroChem.

68. L. H. Lee (1991) "Fundamentals of Adhesion," Plenum Press, New York, NY.

69. W. G. Anderson (1986) "Wettability Literature Survey-Part 2: Wettability Measurement," JCPT, November.

70. A. W. Adamson (1982) "Physical Chemistry of Surfaces," 4th Edition, John Wiley and Sons Inc., New York City 332-68.

71. P. Y. Wu and W. A. Little (1983) "Measurement of Friction Factor for Flow of Gases in Very Fine Channels Used for Micro-miniature Joule – Thompson Refrigerators," Cryogenics, 24:273-277.

72. J. Harley and H. Bau (1989) "Fluid Flow in Micron and Submicron Size Channels," IEEE Trans. THO 249:25-28.

73. X. F. Peng and G. P. Peterson (1996) "Convective Heat Transfer and Flow Friction for Water Flow in Microchannel Structures," International Journal of Heat Mass Transfer, 39:2599-2608.

74. D. Yu, R. Warrington and T. Barren (1995) "An Experimental and Theoretical Investigation of Fluid Flow and Heat Transfer in Microtubes," Proceedings of the ASME/JSME Thermal Engineering Conference, ASME, 1:523-530.

75. S. K. Lim, T. N. Wong, K. T. Ooi, K. C. Toh and K. Suzuki (2000) "Analytical Study of Liquid Flow in a Microtube, Engineering Advances at the Dawn of 21st century," Proceedings of the Seminar on Integrated Engineering, 472-478.

76. G. M. Mala and D. Li (1999) "Flow Characteristics of Water in Microtubes," International Journal of Heat and Fluid Flow, 20:142-148.

77. W. Qu, G. M. Mala and D. Li (2000) "Pressure Driven Water Flows in Trapezoidal Silicon Microchannels," International Journal of Heat and Mass Transfer, 43:353-364.

78. C. Fang, E. S. Julie, F-M. Wang and K. E. Goodson (2010) "Impact of Wall Hydrophobicity on Condensation Flow and Heat Transfer in Silicon Microchannels," Journal of Micromechanics and Microengineering, 20:12-24.

79. Y. Taitel and A. E. Dukler (1976) "A Model for Predicting Flow Regime Transitions in Horizontal and near Horizontal Gas-Liquid Flow," AIChE Journal, 22:47-55.

80. A. E. Fox (2009) "A Study of Optical Propagation in Polymer Liquid Crystal Nanocomposites for Photolithography Applications," Thesis, Drexel University.

81. First Ten Angstroms (1997) Application Notes.

82. A. S. Kulkarni (2004) "Effect of Surface Roughness in Microchannel Flow," Thesis, University of Florida.

83. G. Zhou and S-C. Yao (2009) "Effect of Surface Roughness on Laminar Liquid Flow in Micro-channel," Applied Thermal Engineering, 31:228-234.

84. A. Serizawa, Z. Feng and Z. Kawara (2002) "Two-phase Flow in Microchannels," Experimental Thermal and Fluid Science, 26:703-714.

85. S. W. Clarke, J. G. Jones and D. R. Oliver (1970) "Resistance to Two-Phase Gas-Liquid Flow in Airways," Journal of Applied Physiology, 29:4.

86. M. Sharan and A. S. Popel (2001) "A Two-Phase Model for Flow of Blood in Narrow tubes with Increased Effective Viscosity Near the Wall," Biorheology, 38:415-428.

VITA

Gautham C. Unni, was born on August 13, 1984 in Bangalore, India. He completed his Bachelors in Chemical Engineering from M.S. Ramaiah Institute of Science and Technology, Bangalore, India in June 2007. He then travelled to Rolla, Missouri to pursue a doctorate degree in Chemical Engineering at Missouri University of Science and Technology and graduated in May 2011.

Gautham was guided by Dr. Kimberly Henthorn, Professor of Chemical and Biological. He worked as a Graduate Research Assistant and a Teaching Assistant. His research was focused on the effects of hydrophobicity and surface roughness on two-phase flow in rectangular microchannels.

Gautham's interest in extracurricular activities drove him to become the President of the International Students Club and the Event Coordinator for the India Association, both at Missouri University of Science and Technology.